SYNGAS ASH DEPOSITION FOR A THREE ROW FILM COOLED LEADING EDGE TURBINE VANE

by

Sai Shrinivas Sreedharan

A dissertation submitted to the faculty of Virginia Polytechnic Institute and State University in partial fulfillment of the requirements for the degree of

Doctor of Philosophy
In
Mechanical Engineering

Committee Chair:
Danesh K. Tafti

Committe Members:
Uri Vandsburger
Wing Ng
Srinath Ekkad
Christopher J Roy

27^{th} July 2010

Virginia Tech

Blacksburg, Virginia

Keywords: Leading edge of Turbine Vane, Large Eddy Simulations (LES), Film-cooling, Syngas ash deposition, probabilistic model for deposition, ash composition

SYNGAS ASH DEPOSITION FOR A THREE ROW FILM COOLED LEADING EDGE TURBINE VANE

Sai Shrinivas Sreedharan

ABSTRACT

Coal gasification and combustion can introduce contaminants in the solid or molten state depending on the gas clean up procedures used, coal composition and operating conditions. These byproducts when combined with high temperatures and high gas stream velocities can cause Deposition, Erosion, and Corrosion (DEC) of turbine components downstream of the combustor section. The objective of this dissertation is to use computational techniques to investigate the dynamics of ash deposition in a leading edge vane geometry with film cooling.

Large Eddy Simulations (LES) is used to model the flow field of the coolant jet-mainstream interaction and the deposition of syngas ash in the leading edge region of a turbine vane is modeled using a Lagrangian framework. The three row leading edge vane geometry is modeled as a symmetric semi-cylinder with a flat afterbody. One row of coolant holes is located along the stagnation line and the other two rows of coolant holes are located at $\pm 21.3^\circ$ from the stagnation line. The coolant is injected at 45° to the vane surface with 90° compound angle injection. The coolant to mainstream density ratio is set to unity and the freestream Reynolds number based on leading edge diameter is 32000. Coolant to mainstream blowing ratios (B.R.) of 0.5, 1.0, 1.5, and 2.0 are investigated.

It is found that the stagnation cooling jets penetrate much further into the mainstream, both in the normal and lateral directions, than the off-stagnation jets for all blowing ratios. Jet dilution is characterized by turbulent diffusion and entrainment. The strength of both mechanisms increases with blowing ratio. The adiabatic

effectiveness in the stagnation region initially increases with blowing ratio but then generally decreases as the blowing ratio increases further. Immediately downstream of off-stagnation injection, the adiabatic effectiveness is highest at B.R.=0.5. However, in spite of the larger jet penetration and dilution at higher blowing ratios, the larger mass of coolant injected increases the effectiveness with blowing ratio further downstream of injection location.

A novel deposition model which integrates different sources of published experimental data to form a holistic numerical model is developed to predict ash deposition. The deposition model computes the ash sticking probabilities as a function of particle temperature and ash composition. This deposition model is validated with available experimental results on a flat plate inclined at 45°. Subsequently, this model was then used to study ash deposition in a leading edge vane geometry with film cooling for coolant to mainstream blowing ratios of 0.5, 1.0, 1.5 and 2.0. Ash particle sizes of 5, 7, 10 μm are considered. Under the conditions of the current simulations, ash particles have Stokes numbers less than unity of O(1) and hence are strongly affected by the flow and thermal fields generated by the coolant interaction with the mainstream. Because of this, the stagnation coolant jets are successful in pushing and/or cooling the particles away from the surface and minimizing deposition and erosion in the stagnation region. Capture efficiency for eight different ash compositions are investigated. Among all the ash samples, ND ash sample shows the highest capture efficiency due to its low softening temperature. A trend that is common to all particle sizes is that the percentage capture efficiency is least for blowing ratio of 1.5 as the coolant is successful in pushing the particles away from the surface. However, further increasing the blowing ratio to 2.0, the percentage capture efficiency increases as more number of particles are transported to the surface by strong mainstream entrainment by the coolant jets.

Dedicated to my family

Mr. & Mrs. Pangajam Sreedharan

Mr. & Mrs. RamaLaxmi Srinivasan

Mr. & Mrs. KamalPriya Raguraman

DISCLAIMER

ACKNOWLEDGMENTS

I would like to take this opportunity to thank my advisor, Professor Danesh Tafti. I am one of the fortunate few to have found the perfect advisor for the most crucial phase in my career. He has brilliantly advised me through every hurdle that I encountered during my PhD. It was a pleasure working in his Lab, his constant motivation has helped me explore my hidden potentials. I owe my deepest gratitude to Dr. Tafti for having faith and confidence in me. I would like to thank my committee members: Dr. Ekkad, Dr. Ng, Dr. Roy and Dr. Vandsburger for their scholarly opinions and feedback. I would like to thank the experimental group: Eric and Steve, for their weekly inputs. I also want to thank Dr. Duggirala for serving as a proxy to Dr. Roy during my final defense presentation. I would like to extend my gratitude to DOE-NETL-UTSR, for providing me with the required financial support throughout the course of my PhD.

I would like to thank my labmates: Aroon, Ali, Mohammad, Pradeep, Shi-Ming, Keagen, Kohei, Jose, Jonathan, Naresh, Sunil, Amit , Nagendra (Nagi), Surya, Kamal, Vivek and Sukhjinder (Sukhi), for making this thesis possible. I am indebted to all of them for supporting me in a number of ways. I cherished all our discussions, the lab meetings and even though I lost lunch/coffee bets, I enjoyed the arguments we had. Special thanks to Nagi, Amit and Naresh for helping me review my dissertation.

I would like to thank my roomates and friends at Blacksburg who made my stay at Blacksburg memorable. I would like to thank my parents and my family for standing by my side and supporting me through tough times. It would not have been possible without their support.

TABLE OF CONTENTS

LIST OF TABLES

LIST OF FIGURES

Figure Page

ABBREVIATIONS

B.R.	Blowing ratio
DE	Deposition & Erosion
DEC	Deposition, Erosion & Corrosion
DPM	Discrete Phase Model
DRW	Discrete Random Walk
EFEP	Energy Fraction of Erosive Particles
GT	Gas Turbine
IGCC	Integrated Gasification Combined Cycle
LES	Large Eddy Simulations
NBO/T	Non-Bridging Oxygens to Tetrahedral Oxygens
PVC	Polyvinyl Chloride
RANS	Reynolds Averaged Navier-Stokes
RMS	Root Mean Square
ST	Softening Temperature
TADF	Turbine Acceleration Deposition Facitlity
TBC	Thermal Barrier Coating
TKE	Turbulent Kinetic Energy

NOMENCLATURE

η	Adiabatic Effectiveness
C_s	Smagorinsky constant
C_d	Drag coefficient
d	Coolant Hole Diameter
d_p	Particle Diameter
D	Leading Edge Diamater
D	Coupon Diameter
L	Coolant Hole Length
L_c	Characteristic Length
m	Mass of the particle
n	Normal distance from vane surface
Nu	Nusselt number
P	Lateral Spacing
Pr	Prandtl number
Re_L	Reynolds number, $Re_L = \frac{(U_{jet})L}{\nu}$
Re_p	Particle Reynolds number, $Re_p = \frac{(U_{jet}-U_p)L}{\nu}$
s	Streamwise direction along the vane surface
S	Strain rate tensor
St_p	Momentum Stokes number
St_{conv}	Convective Stokes number
St_{rad}	Radiative Stokes number
θ	Non-dimensional temperature, $(T - T_c)/(T_\infty - T_c)$
θ	Non-dimensional temperature, $(T - T_a)/(T_{jet} - T_a)$
t	Time

y^+	Non-dimensional wall distance
U	Velocity
V_{normal}	Particle velocity normal component
x^p	Particle location
ρ	Density (kg/m^3)
μ	Dynamic Viscosity ($Pa.s$)
ν	Kinematic Viscosity, (m^2/s)
Subscripts / Superscripts	
a	Ambient air
c	coolant
f	Fluid
jet	Inlet jet temperature
∞	Freestream
$melt$	PVC melting temperature
p	Particle
s (or) $soft$	Softening Temperature
t	Turbulent
$*$	Dimensional quantity
$'$	Fluctuating quantity

1. INTRODUCTION

The goal of DOE's fossil energy turbine program is to provide power generation technology essential to the success of advanced fossil energy power systems in the 2008 to 2015 time frame. One of the key capabilities needed to achieve this goal is the use of Syngas from coal gasification as a fuel in land based gas turbines. Syngas has huge environmental benefits in reducing emissions and is also cost effective when compared to the use of natural gas. One of the issues in realization of DOE's vision relates to the durability of turbine components subjected to a harsh high temperature, high pressure, and high velocity environment in the gas path immediately downstream of the combustor. The byproducts of gasification and combustion of coal introduces corrosive vapors, and molten ash, which combined with high temperatures and high gas stream velocities can cause Deposition, Erosion, and Corrosion (DEC) of turbine components. Regardless of the advances in gas clean up systems, Syngas entering the combustion chamber contains traces of flyash particles in the size ranging up to 10 microns which when deposited can result in surface roughness values which can be orders of magnitude higher than the particle size.

These flyash particles are physically in a molten state as they exit the gas turbine combustor and enter the hot gas flow path. The components most likely to experience DEC are the first stage nozzle guide vane and rotor, and hub and tip regions where secondary flows dominate. The region most susceptible to DEC is the leading edge region of the vane. The presence of film cooling showerhead at the leading edge can potentially have a large impact on DEC by modifying the flow and temperature field in the vicinity of the leading edge. Deposition increases the surface roughness on the vane surface and thus increases skin friction drag. In the case of film-cooling, molten ash deposition build up cause blockages in film cooling holes, leading to deterioration

in effectiveness and overheating of the vane. Additionally, solid ash particles can degrade Thermal Barrier Coating (TBC) by erosion and contribute to spallation. Thus, from the above, knowledge of the mechanisms responsible for deposition and erosion and methods of mitigation can help improve the operational life of the turbine components and reduce the risk of catastrophic failures.

Past studies have focused on particle impaction in the first stage stator and rotor and the relevant literature review are summarized in the chapters to follow. There are no detailed studies on the effect of film cooling in spite of its large potential influence on DEC. The leading edge region of a vane is particularly susceptible to DEC, and this dissertation provides detailed and comprehensive understanding of film cooling physics near the stagnation region and quantifying the effect of showerhead cooling on deposition and erosion. Not only does the presence of film cooling jets dramatically alter the flow field and particle trajectory but also has a large effect on the temperature field which influences the phase of the particles arriving at the blade surface and whether they lead to deposition or erosion.

To the best of our knowledge, there is no previous study (computation or experimental) in the gas turbine literature which has studied the hydrodynamic and thermal conditions under which DEC occurs at the leading edge in the presence of showerhead film cooling. This research uses a combination of the method of time-accurate Large-Eddy Simulations (LES) and Discrete Phase Modeling (DPM) as a tool for simulating particle dynamics at realistic engine conditions. LES accurately represents the unsteady nature of the flow and temperature field and the relevant turbulent length scales. This time-accurate LES data when used by DPM leaves little uncertainty in modeling the trajectory of particles which will be very sensitive to the large scale turbulence generated by the interaction of the coolant jets and the mainstream.

This thesis also investigates the use of a steady-state Reynolds-Averaged Navier Stokes (RANS) for predicting the flow in conjunction with a Discrete Random Walk (DRW) method for the particle phase to predict deposition. In addition to using the

RANS generated mean turbulent field in the DRW to calculate particle trajectories, the mean LES turbulent flow field is also used with DRW to evaluate the differences between the two methods. While the use of LES for the mean turbulent field is still computationally expensive, deposition for different ash characteristics are much easier to obtain than a instantaneous LES calculations combined with DPM method. To the best of our knowledge, this present study is the first to implement the DRW in an LES framework to predict deposition giving a fairly accurate representation of deposition when compared to that obtained from time-accurate LES calculations.

Objective

The objective of this study is to investigate the dynamics of flyash deposition and erosion on a three-row film cooled leading edge vane geometry at realistic engine conditions. Time accurate Large-Eddy Simulation (LES) is used to accurately characterize the complex turbulent flow field for a three-row film cooled leading edge geometry. The ash particles are treated discretely in the Lagrangian frame of reference. The computations incorporate a novel deposition model which computes sticking probability as a function of ash particle viscosity as criteria for deposition and an idealized restitution coefficient of unity for particles that potentially contribute towards erosion.

This dissertation addresses the following issues:

1. Effect of ash particle sizes on deposition in the presence of showerhead film cooling.

2. Effect of coolant injection (blowing ratio) on ash particle trajectories and deposition.

3. Effect of deposition as a function of ash composition and particle softening temperature.

4. Comparison of steady flow RANS computations to time-accurate LES simulations.

This dissertation is compilation of work that is under-review or has been published in peer-reviewed journal and conference proceedings and is structured as follows. Chapter 1 discusses the motivation and states the research objectives. Chapter 2 studies the effect of blowing ratio on the film cooling performance (adiabatic effectiveness). Chapter 3 explores the effect of deposition on a three-row showerhead leading edge vane geometry. The deposition results discussed in Chapter 3, uses a discontinuous step function deposition model which is based on a single ash softening temperature. Chapter 4 discusses the development and validation of a new deposition model with available experiments on a flat plate inclined at 45°. Chapter 5 analyzes ash deposition based on the novel deposition model on showerhead leading edge vane geometry.

2. EFFECT OF BLOWING RATIO IN THE NEAR STAGNATION REGION OF A THREE-ROW LEADING EDGE FILM COOLING GEOMETRY USING LARGE EDDY SIMULATIONS

Abstract

Computational studies are carried out using Large Eddy Simulations (LES) to investigate the effect of coolant to mainstream blowing ratio in a leading edge region of a film cooled vane. The three row leading edge vane geometry is modeled as a symmetric semi-cylinder with a flat afterbody. One row of coolant holes is located along the stagnation line and the other two rows of coolant holes are located at $\pm 21.3^{\circ}$ from the stagnation line. The coolant is injected at 45° to the vane surface with 90° compound angle injection. The coolant to mainstream density ratio is set to unity and the freestream Reynolds number based on leading edge diameter is 32000. Blowing ratios (B.R.) of 0.5, 1.0, 1.5, and 2.0 are investigated. It is found that the stagnation cooling jets penetrate much further into the mainstream, both in the normal and lateral directions, than the off-stagnation jets for all blowing ratios. Jet dilution is characterized by turbulent diffusion and entrainment. The strength of both mechanisms increases with blowing ratio. The adiabatic effectiveness in the stagnation region initially increases with blowing ratio but then generally decreases as the blowing ratio increases further. Immediately downstream of off-stagnation injection, the adiabatic effectiveness is highest at B.R.=0.5. However, further downstream the larger mass of coolant injected at higher blowing ratios, in spite of the larger jet penetration and dilution, increases the effectiveness with blowing ratio.

A part of this work is published in IGTI: ASME paper # GT09-59325 & IMECE2008-67019

2.1 Introduction

Recent advances in gas turbine technology are exploring avenues to increase thermal efficiencies. One of the ways to improve efficiency is by raising combustor exit temperatures. However, the gas exit temperatures are limited by the material properties of the turbine vanes. In order to reduce component temperatures, turbine blades are cooled by routing coolant through serpentine passages within the turbine blade which cools the blade internally. The same air is ejected through discrete film cooling holes on the turbine blade surface which provide external surface cooling. This study focuses on film cooling of the first stage turbine vane which is subjected to the maximum gas temperatures. The air provided for film cooling of turbine components is extracted from the compressor and reduces the overall efficiency of the cycle. As a result, it is vital to maximize film cooling effectiveness for a limited amount of available coolant. Hence understanding the complex physics of interaction between film cooling jets and the hot mainstream is critical.

There are various factors that significantly affect the cooling afforded by the coolant injected through discrete holes on a turbine vane. Factors such as free-stream turbulence, location of cooling holes on the vane surface, geometry and coverage of holes, and mass and momentum injection ratios can play a significant role. Goldstein et al. [1] were the first to perform experiments on a flat plate to study the influence of coolant hole geometry on film cooling effectiveness. Widening of the coolant holes produced better film cooling effectiveness. Several experimental studies on shaped hole film-cooling technology were conducted ever since to investigate the coolant hole configurations and is summarized in a review paper by Bunker [2].

The leading edge region of the blade is of critical interest because it carries a high heat load due to the high heat transfer coefficients. Mick and Mayle [3] carried out experiments to study the effects of blowing ratio on adiabatic film cooling effectiveness. They discussed changes in film cooling effectiveness on the surface as the blowing ratio was varied from 0.38-0.97. In this range of blowing ratios they found

that, at the leading edge, the film cooling effectiveness decreased as the blowing ratio increased. This is attributed to the increased mainstream penetration. Mehendale and Han [4], Ekkad et al. [5] and Johnston et. al. [6] studied the effect of freestream turbulence on leading edge film cooling. Their experiments in general concluded that mainstream turbulence reduced film cooling performance. Cruse et al. [7], Yuki et al. [8] and Ou and Rivir [9] have performed experiments to measure film cooling performance on the leading edge modeled as a symmetric quarter cylinder with a flat after body. Almost all of the studies have focused on adiabatic effectiveness which is an essential measure of film cooling performance.

Many numerical studies have been carried out to-date to simulate and quantify major aspects related to film cooling performance. Computational studies up to 1993 have been summarized in a review paper by Simoneau and Simon [10]. Chernobrovkin and Lakshminarayana [11] computationally investigated the film cooling performance on a leading edge modeled as a symmetric quarter cylinder model using the low Reynolds number $k-\epsilon$ turbulence model. They showed vorticity plots and discussed how the mainstream entrainment created local hot spots on the vane surface which eventually resulted in a decreased adiabatic effectiveness. However, they recommended the use of better turbulence models to improve accuracy. Lakehal et al. [12] employed various versions of $k-\epsilon$ turbulence models to quantify film cooling effectiveness as the blowing ratio is varied from 0.3 - 0.9. They proposed further refinements to the turbulence model to account for laminar-turbulent transition which was entirely neglected. York and Leylek [13] used the realizable $k-\epsilon$ turbulence model to study the adiabatic effectiveness on a leading edge modeled as a symmetric quarter cylindrical model. The discrepancies in predicting heat transfer ratio increased as the blowing ratio increased (B.R. $>$ 1.1). The predicted value of heat transfer ratio was significantly lower (30% at B.R. 1.5) than the experimental data point. Lin and Shih [14] performed computations using the $k-\omega$ shear-stress transport (SST) turbulence model on the cylindrical leading edge with a flat afterbody model with three row showerhead. Their results showed the surface distributions of adiabatic film

cooling effectiveness on the vane surface. This SST model under predicted the normal spreading of the coolant by about 20 to 50%. Acharya et al. [15] have reviewed and identified limitations of various computational models used in film cooling technology. They performed their calculation on a flat plate. They compared the results obtained from LES, DNS and several available turbulence models namely $k - \epsilon$ and Reynolds stress transport model to experiments and found substantial improvements in DNS and LES. Overall, they concluded that LES is superior in predicting the time averaged velocities and turbulent statistics in the near field of the jet mainstream interaction.

The most important feature of using LES is that it eliminates the semi-empiricism of RANS based turbulence models. LES studies have been used to predict film cooling performance on a flat plate by Tyagi and Acharya [16], Lui and Pletcher [17], Iourikina and Lele [18, 19] and Guo et al. [20]. Recent LES studies on leading edge modeled as a symmetric quarter cylinder with a flat afterbody has been performed by Rozati and Tafti [21, 22]. Their geometry had two rows of injection on either side of the stagnation line and the coolant was injected at 30° to the surface and 90° compound angle injection. They reported results for adiabatic effectiveness and heat transfer coefficient where the freestream Reynolds number was 100,000 and blowing ratio ranged as 0.4, 0.8 and 1.2. Overall, they discussed the detailed mainstream jet mixing mechanism and their film cooling performance results showed excellent agreement with experiments.

2.2 Objective

The study is an extension of the work of Rozati and Tafti [21, 22] to a more practical geometry and a larger range of blowing ratios. The present study investigates a symmetric three row showerhead leading edge film cooling geometry at the leading edge of a semi-cylindrical model with a flat after body using LES. It follows a previous study which investigated the adiabatic effectiveness at a blowing ratio of 0.5 for the same geometry [23]. In this chapter, blowing ratios of 0.5, 1.0, 1.5 and 2 are

investigated. This study compares the dynamics of jet mainstream interaction and subsequent effect on the temperature field and adiabatic effectiveness between the four blowing ratios. In spite of some idealizations - density ratio of unity and no free-stream turbulence, this is the first LES investigation in a three-row leading edge geometry at high blowing ratios and provides previously unavailable insight into the aerothermal aspects of the flow.

2.3 Methodology

2.3.1 Governing equations

The governing transport equations which include the incompressible mass, momentum and energy conservation are solved in a generalized body-fitted coordinate system. The equations are non-dimensionalized using a characteristic length scale D, characteristic velocity scale U_∞, and a characteristic temperature scale $(T_\infty - T_c)$. The non-dimensional time dependent equations are as follows:

Continuity

$$\frac{\partial}{\partial \xi_j}\left(\sqrt{g}\bar{U}^j\right) = 0 \tag{2.1}$$

Momentum

$$\begin{aligned}\frac{\partial}{\partial t}\left(\sqrt{g}\bar{u}_i\right) \;+\; & \frac{\partial}{\partial \xi_j}\left(\sqrt{g}\bar{U}^j\bar{u}_i\right) = -\frac{\partial}{\partial \xi_j}\left(\sqrt{g}(\vec{a}^j)_i\bar{p}\right) \\ & +\frac{\partial}{\partial \xi_j}\left(\left(\frac{1}{Re}+\frac{1}{Re_t}\right)\sqrt{g}g^{jk}\frac{\partial \bar{u}_i}{\partial \xi_k}\right)\end{aligned} \tag{2.2}$$

Energy

$$\begin{aligned}\frac{\partial}{\partial t}\left(\sqrt{g}\bar{\theta}\right) \;+\; & \frac{\partial}{\partial \xi_j}\left(\sqrt{g}\bar{U}^j\bar{\theta}\right) = \\ & \frac{\partial}{\partial \xi_j}\left(\left(\frac{1}{PrRe}+\frac{1}{Pr_tRe_t}\right)\sqrt{g}g^{jk}\frac{\partial \bar{\theta}}{\partial \xi_k}\right)\end{aligned} \tag{2.3}$$

where $\vec{a}^i$ are the contravariant basis vectors [*] , $\sqrt{g}$ is the Jacobian of the transformation, $g^{(ij)}$ is the contravariant metric tensor, $\sqrt{g}U^j = \sqrt{g}(\vec{a}^j)_i u_i$ is the contravariant

[*]The notation $(\vec{a}^j)_i$ is used to denote the i-th component of vector $\vec{a}^j$, $(\vec{a}^j)_i = \partial\xi_j/\partial x_i$

flux vector, u_i is the Cartesian velocity vector, and θ is the non-dimensional temperature. The overbar in the continuity, momentum and energy equations denote grid filtered quantities. Re_t is the inverse of the non-dimensional turbulent eddy-viscosity and is obtained by the Smagorinsky model.

$$\frac{1}{Re_t} = C_s^2(\sqrt{g})^{(2/3)}|\bar{S}|$$

where $|\bar{S}|$ is the magnitude of the strain rate tensor given by $|\bar{S}| = \sqrt{(2\bar{S}_{ik}\bar{S}_{ik})}$. The Smagorinsky constant C_s^2 is obtained via the dynamic procedure [24]. The turbulent Prandtl number is assumed to have a constant value of 0.5 [25].

2.3.2 Computational model

Geometry Description

The computational domain models the leading edge of a vane as a semi-cylindrical form with a flat after body. Three rows of film cooling holes are employed. One row is located at stagnation and two rows are located at ±4d, on either side of the stagnation line. The lateral pitch spacing (P) between two holes for any given row is 4.5d, and the relative position of the holes on the upper half and lower half are staggered with respect to the stagnation hole. The origin is fixed at the center of the domain at stagnation with the stagnation hole located at z = -1.125d and staggered off-stagnation holes located at z = 1.125d. The coolant hole diameter ratio (D/d) is 21.5 and the length ratio of the coolant pipe (L/d) is 10.75 . The coolant is injected laterally at 45° to the surface with a compound angle of 90° to the mainstream. Figure 2.1 shows the head-on view of the leading edge model. The solid line shows the computational domain. Figure 2.2 shows the computational domain of interest as the shaded region. It extends 10D in the x-direction, 5D in y-direction and 4.5d in the spanwise z-direction.

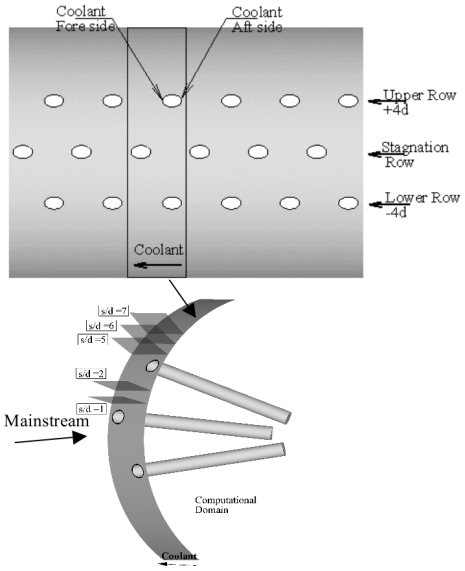

Figure 2.1.: Leading edge vane model and near field streamwise planes used in presenting results.

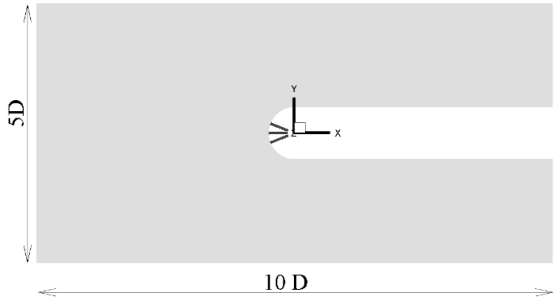

Figure 2.2.: Computational domain in side view (X-Y plane)

Boundary conditions

The adiabatic wall approach is used to predict the adiabatic wall temperature and effectiveness. Therefore, the surface is maintained at zero wall flux, the non-dimensional coolant temperature is set to 0 and the non-dimensional mainstream temperature is set to 1. Periodic boundary conditions are applied in the span (z-direction) to simulate an infinite row of holes. To simulate a linear cascade arrangement, periodic boundary conditions are also applied in the y-direction (figure 2.2). No penetration and no slip conditions are applied on the vane surface and on the

coolant pipe wall. The mainstream inlet condition is a constant velocity profile with no turbulence intensity and a convective outflow boundary condition is applied at the exit. The inlet boundary condition for the coolant pipe is also a constant velocity profile applied normal to the cross-section of the pipe. In the present study, the free stream Reynolds number based on leading edge diameter and the free stream velocity is 32,000. The coolant to mainstream blowing ratio of 0.5, 1.0, 1.5 and 2.0, and a density ratio of 1 is studied.

Computational grid and sensitivity study

A key feature for any numerical simulation is having a mesh with minimally skewed cells and superior near wall resolution. Here a multi-block framework is adopted for meshing the computational domain of interest. Gridgen, a commercial numerical grid generation software is used to create this multi-block grid. The grid is made of a structured mesh with unstructured block topology. The baseline grid selected for this geometry relied heavily on our experience in previous simulation performed in the stagnation region at Re_D=100,000 (Rozati and Tafti [21, 22]). To construct the baseline grid, the Reynolds number based on coolant hole diameter and coolant inlet velocity is a decisive factor for the near wall resolution in the coolant pipe. The near wall resolution estimated in the coolant pipe is carried forward to the cylinder surface and flat after body. One of the commonly used variables to measure the adequacy of grid resolution is y_1^+ (non-dimensional wall distance of the first grid point). Figure 2.3 shows the y^+ distribution on the vane surface for blowing ratio of 0.5. The max value of y_1^+ is 0.7 located just downstream of the hole and there are about 7 grid points within a y^+ of 10. Based on these requirements, the baseline grid has a size of 11.38 million cells.

A grid sensitivity study is carried out for a blowing ratio of 1.5 and 2.0. All the calculations in the grid sensitivity study are averaged for 7 non-dimensional time units. Two different grid spacing are considered for the same grid size (11.38 million cells). Figure 2.4 shows the spacing of the grid points in the wall normal direction. In

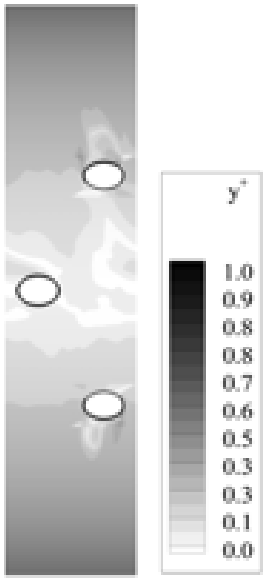

Figure 2.3.: y_1^+ distribution on cylinder surface.

the first grid (figure 2.4a), the grid spacing increases as a hyperbolic tangent function away from the wall. In the second grid (figure 2.4b), grid points were also spaced as a hyperbolic tangent function, except an equal grid spacing was used in between 0.1D to 0.45D from the vane surface (wall). This grid was studied to ensure eddies formed through the jet penetration are well resolved. For B.R. = 2.0, the stagnation jet penetrates to about 0.33D. Figure 2.5 shows the streamwise distribution of laterally averaged spanwise adiabatic effectiveness on the vane surface for the two grids at B.R. = 1.5 and B.R. =2.0. For B.R. = 1.5, the coarse grid spacing underpredicts the effectiveness in the stagnation region by 20% at s/d = 3.37 and downstream of the off-stagnation injection by 19% at s/d = 14. Again at B.R. = 2.0, the coarse grid under-predicts the effectiveness in the stagnation region by 20% at s/d = 2.8 and downstream of the off-stagnation injection by 23% at s/d = 5.4. Results shown in this study use the fine grid as a baseline grid for B.R. =1.5 and B.R. = 2.0.

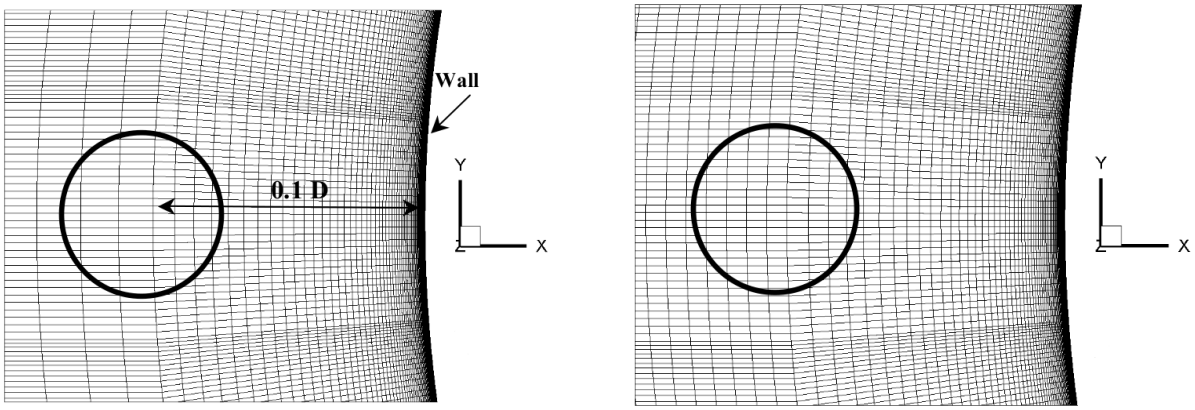

(a) Coarse Spacing (b) Fine spacing of cells

Figure 2.4.: Mesh near the leading edge model

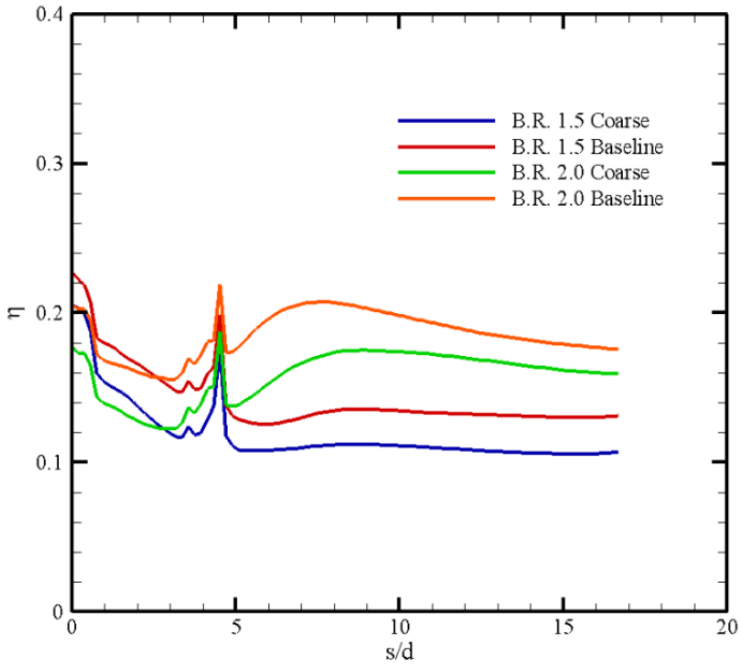

Figure 2.5.: Spanwise laterally averaged effectiveness for 2 different grid sizes for B.R. 1.5 and 2.0

2.4 Discussion of results

The simulation uses an in-house developed conservative finite volume code, GenIDLEST which stands for generalized incompressible direct and large eddy simulations of turbulence (Tafti [26]). The discretization of the governing equations uses a second order central difference scheme on a non-staggered grid topology. The convergence criterion for the momentum, pressure and the energy are 1×10^{-6}, 1×10^{-6} and 1×10^{-6} respectively at each time step. The time step is set at 7×10^{-5} for B.R. =0.5 and B.R. =1.0 and 6×10^{-5} for B.R. =1.5 and B.R. =2.0. The flow is allowed to develop for 5 characteristic non-dimensional time units, before time averaging, and is time averaged for 9 characteristic time units. All the results shown here are computed using 160 processors on Virginia Techs high performance terascale supercomputing facility: SYSTEM X.

The results focus on a comparison of the four blowing ratios as they affect the jet-mainstream turbulent interaction, penetration into the mainstream, entrainment and mixing and finally the temperature field and adiabatic effectiveness.

2.4.1 Instantaneous flow features

Figure 2.6 shows the iso-surface of instantaneous coherent vorticity extracted by using the eduction methodology of Chong et al. [27] for B.R.= 0.5 and 2.0. In this vortex identification technique, a vortex core is defined in a space where the rotation tensor dominates the rate of deformation tensor. The distinct patterns within the flow field are identified as vortices and the magnitude is indicative of the strength. At the lower blowing ratio, the vorticity in the flow field is largely coherent with well defined vortex structures. As the blowing ratio increases to 2.0 there is very little coherency in the flow field which degenerates into smaller scale vorticity characteristic of a fully turbulent flow. Clearly visible at B.R.=0.5 are ring vortices in the stagnation jet which destabilize and breakdown as the jet penetrates laterally across the pitch and then

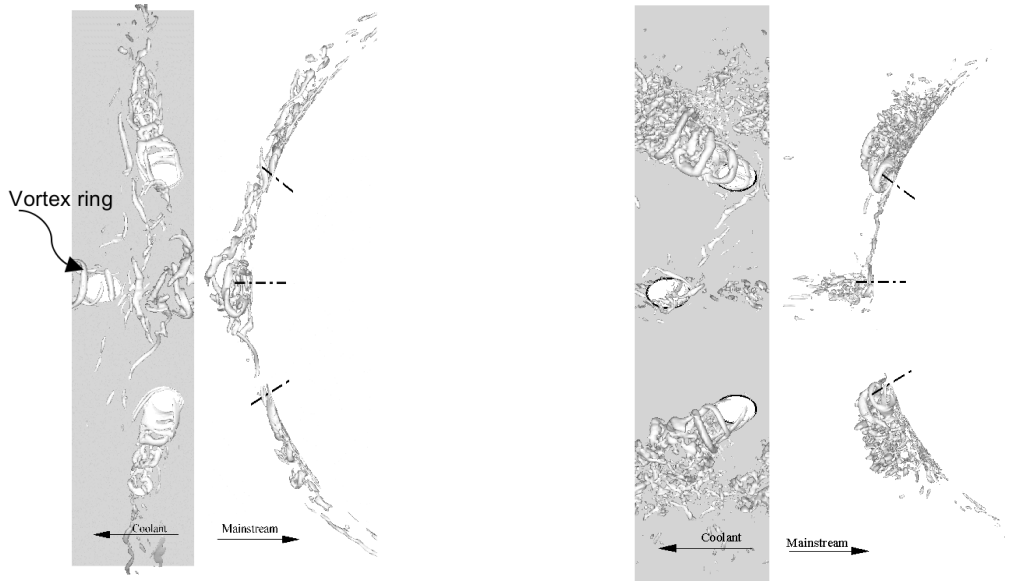

(a) Front View Side View (b) Front View Side View

Figure 2.6.: Structure of coherent vorticity (a) B.R. 0.5 (Iso-surface value = 30) (b) B.R. 2.0. (Iso-surface value = 75)

convect along the blade surface under the influence of the accelerating mainstream flow.

Figure 2.7 and figure 2.8 show the instantaneous velocity vectors and corresponding temperature contours in the cross stream and lateral direction in planes normal to the vane surface for B.R.=0.5 and 2.0. Also plotted with the velocity vectors are contours of coherent vorticity of magnitude 15 for B.R.=0.5 and 25 for B.R.=2.0. The plane at s/d=1.0 is just downstream of the stagnation hole, whereas s/d=5.0 is immediately downstream of the off-stagnation hole which is centered at s/d=4.0. The dashed lines and the dotted lines in the s/d planes are representative of stagnation (z/d = -1.125) and off-stagnation hole (z/d = 1.125) centerline, respectively, in the lateral direction (Figure 2.1). Figure 2.9 plots the instantaneous temperature contours in lateral planes along the pitch.

The following observations are made:

1. The stagnation jets have a much larger lateral movement across the pitch than the off-stagnation jets. At B.R.=0.5, the stagnation jet penetrates laterally across the pitch and also into the freestream but is pushed back to the surface of the vane to protect it from the hot mainstream gases. At B.R=2.0, the jet because of its higher momentum penetrates further into the mainstream and is dispersed by turbulent diffusion affording little or no protection to the stagnation region. At all blowing ratios, the stagnation coolant jet penetrates much further into the mainstream than the off-stagnation jets.

2. The same scenario holds for off-stagnation injection with some differences. While the B.R.=0.5 jet remains attached to the vane surface and gives localized protection to the surface across a small fraction of the lateral pitch, at B.R.=2.0, the jet penetrates further into the mainstream and spreads laterally across the pitch. In spite of the coolant being diluted by the mainstream through turbulent diffusion, it provides a much broader coverage of the surface across the pitch.

3. At both blowing ratios, mainstream entrainment through the action of the counter rotating vortex pair [21, 22] also plays an important role in diluting the effectiveness of the coolant. Because of the compound angle injection the vortex pair is asymmetric with a much stronger clockwise component which entrains mainstream fluid from the aft side of the jet in the direction of coolant injection. This aspect can be clearly discerned for B.R.=2.0 at s/d=5, 6, and 7 in figure 2.8. As the coolant core moves laterally across the pitch so do the entrainment vectors beneath the coolant core. Superimposed on the large scale entrainment is small scale vortcity, some of which is transported from the stagnation region, which also aid in mixing.

2.4.2 Turbulent kinetic energy

Figure 2.10 and figure 2.11 show the mean T.K.E. contours (normalized by U_∞^2) in planes normal to the vane surface along the stream wise direction for all the blowing ratios. T.K.E is produced by the shear interaction between the coolant jet and the mainstream as the jet penetrates into the flow and also by the strong shear induced underneath the coolant jet in the near wall region due to entrainment [22]. This is a good indicator of the turbulent mixing between coolant and mainstream. As the blowing ratio increases, the T.K.E. also increases. At B.R. = 2.0, (figure 2.11) T.K.E. values as high as 0.4 (z/d = -1.125, stagnation hole centerline) are generated in the coolant core exiting from the stagnation hole. As the coolant from the stagnation hole is convected downstream to s/d = 1 and s/d = 2, the maximum T.K.E. values drop to 0.22 and 0.13, respectively. These values are augmented with the off-stagnation coolant injection with values as high as 0.57 at s/d=4. As noted earlier (figure 2.7, 2.8, 2.9), and also seen in the T.K.E. contours is the increase in the lateral spread of the coolant as the blowing ratio increases.

2.4.3 Mean temperature field

Figure 2.12, 2.13 in streamwise and 2.14 in spanwise show the mean temperature contours. Two main observations can be made from the plots, which are in agreement with the instantaneous fields.

1. The coolant from the stagnation row penetrates much further into the mainstream than off-stagnation injection and as a consequence undergoes considerable dilution by turbulent interaction with the oncoming mainstream. Hence, although the coolant forms a protective umbrella over the stagnation region (Figure 2.14), its effectiveness in protecting the stagnation region is limited. Controlling the stagnation jet normal momentum by lowering the injection angle or using diffuser shaped holes or other means would result in large gains in effectiveness, even more so than off-stagnation holes.

2. The off-stagnation coolant jets do not have much movement along the lateral pitch before they are redirected in the flow direction at low blowing ratios. This coupled with a lower intensity interaction with the mainstream provides good localized protection to the vane surface, but leaving most of the lateral pitch scantly protected. As the blowing ratio increases, jet penetration in the lateral and normal directions increase. At B.R.=2, the presence of the coolant jet is felt throughout the lateral pitch, albeit after considerable mixing with the mainstream flow.

2.4.4 Adiabatic effectiveness

Figure 2.15 shows the contours of adiabatic effectiveness that is achieved by the film cooling on the vane surface to protect the vane surface from high temperatures at different coolant to mainstream blowing ratio. Figure 2.16 shows the line plots of laterally averaged adiabatic effectiveness along the span of the vane surface as a function of downstream location (s/d). The spanwise average is found by averaging across the upper and lower halves of the geometry. The surface adiabatic effectiveness in the stagnation region is a function of the jet penetration and mixing and the amount of coolant injected. At B.R.=0.5, jet penetration into the mainstream is the smallest amongst the different blowing ratios resulting in the least amount of mixing. Hence it has the largest effectiveness at the stagnation line. However, because of the larger injected mass at B.R.=1.0 and the redirection of the coolant to the vane surface, the adiabatic effectiveness downstream of the stagnation line is higher than B.R.=0.5. As the blowing ratio increases further to 1.5 and 2.0, the effectiveness decreases in the immediate vicinity of the stagnation line as the jet penetrates further into the mainstream with enhanced mixing. In spite of more coolant mass at these blowing ratios the mixing and subsequent dilution of the jet dominate and the resulting effectiveness is less than at B.R.=1.0 in the stagnation region.

The behavior of the adiabatic effectiveness follows the same principles downstream of the second row of injection. There is a fine balance between injected

coolant mass and jet penetration and mixing. At the lowest blowing ratio of 0.5, the injected coolant remains close to the surface and provides the highest effectiveness immediately downstream of injection. However the effectiveness decays rapidly, as a result of the smaller mass of coolant and lower lateral spreading of the coolant. As the blowing ratio increases to 1.0, the larger initial penetration of the jet into the mainstream reduces the effectiveness immediately downstream of injection, but which increases as the coolant is pushed back to the surface. At B.R.=1.5, the penetration into the mainstream is larger and in spite of the larger coolant mass, dilution of the coolant dominates the adiabatic effectiveness at the surface. At B.R.=2.0, however, in spite of the high T.K.E. generated and the intense mixing between the jet and the mainstream, the larger coolant mass injected and the larger lateral spread of the jet dominates the adiabatic effectiveness at the surface. In spite of different geometrical arrangements, which preclude quantitative comparisons, similar adiabatic effectiveness trends are observed by Arts and Bourguignon [28], Ou and Rivir [9], and Zhang and Moon [29].

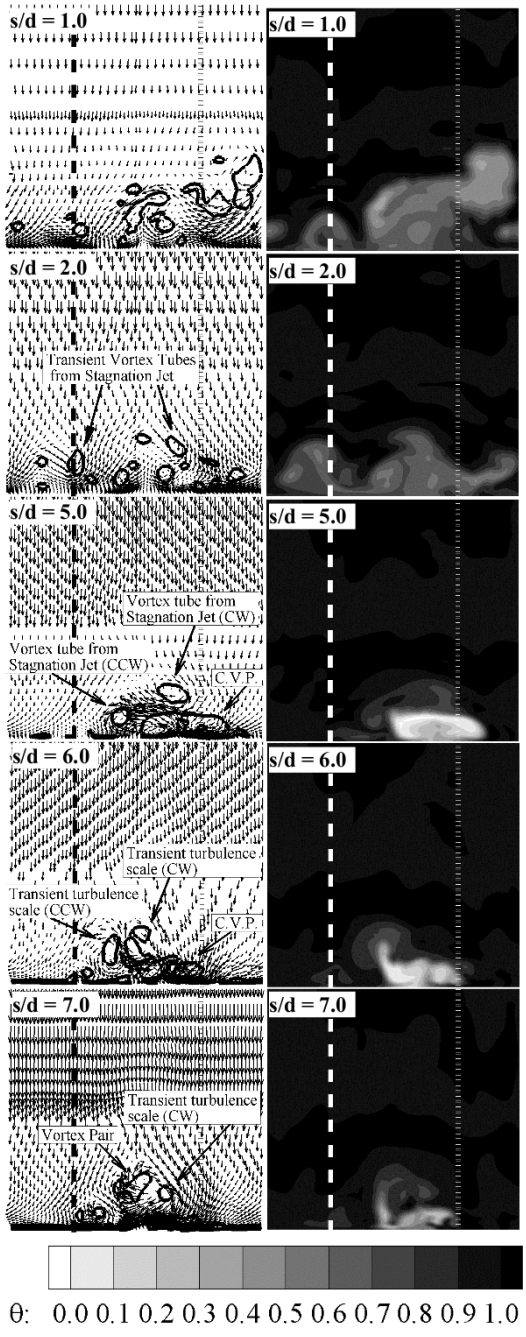

Figure 2.7.: Instantaneous velocity vectors and temperature contours in streamwise direction (B.R. = 0.5)

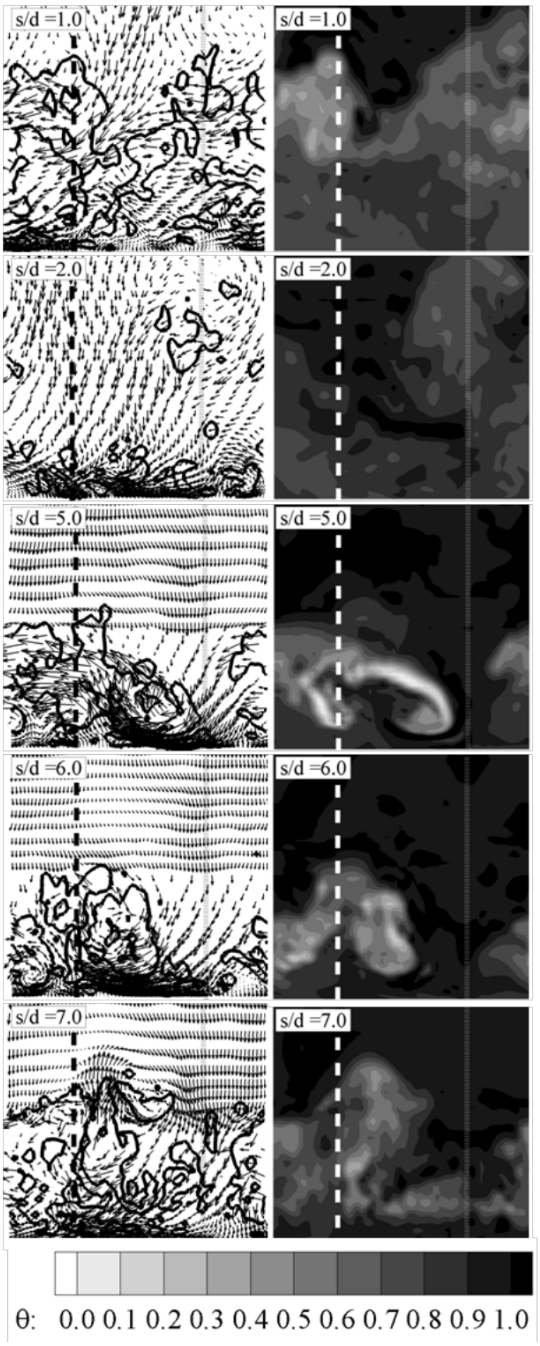

Figure 2.8.: Instantaneous velocity vectors and temperature contours in streamwise direction (B.R. = 2.0)

Coolant injection is from right to left. Height of domain is 4.28d. Dash line is centerline of stagnation hole (z/d=-1.125); dotted line is centerline of off-stagnation hole (z/d=1.125), CCW-counter-clockwise; CW-clockwise

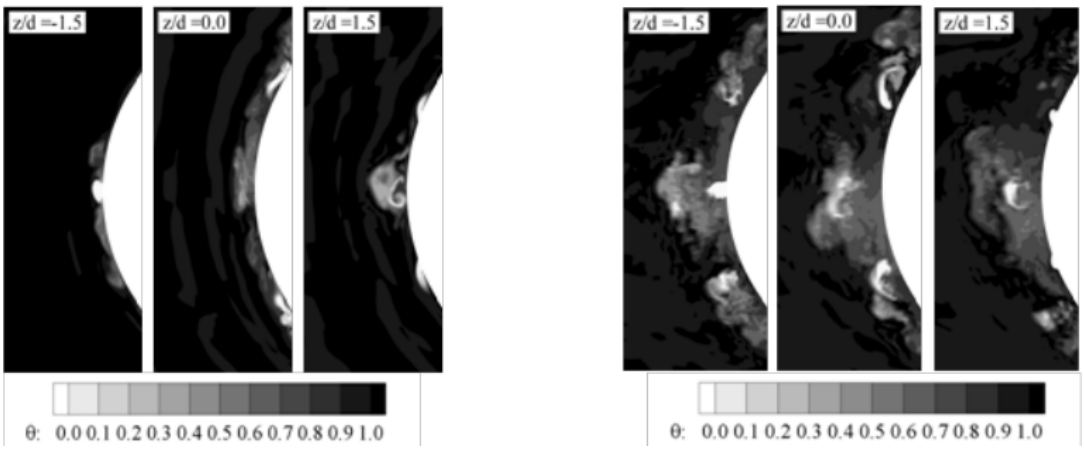

(a) (b)

Figure 2.9.: Instantaneous temperature contours at different lateral planes. (a) B.R. 0.5 (b) B.R. 2.0. Stagnation hole centerline is at z/d=-1.125 and off-stagnation hole centerline is at z/d=1.125.

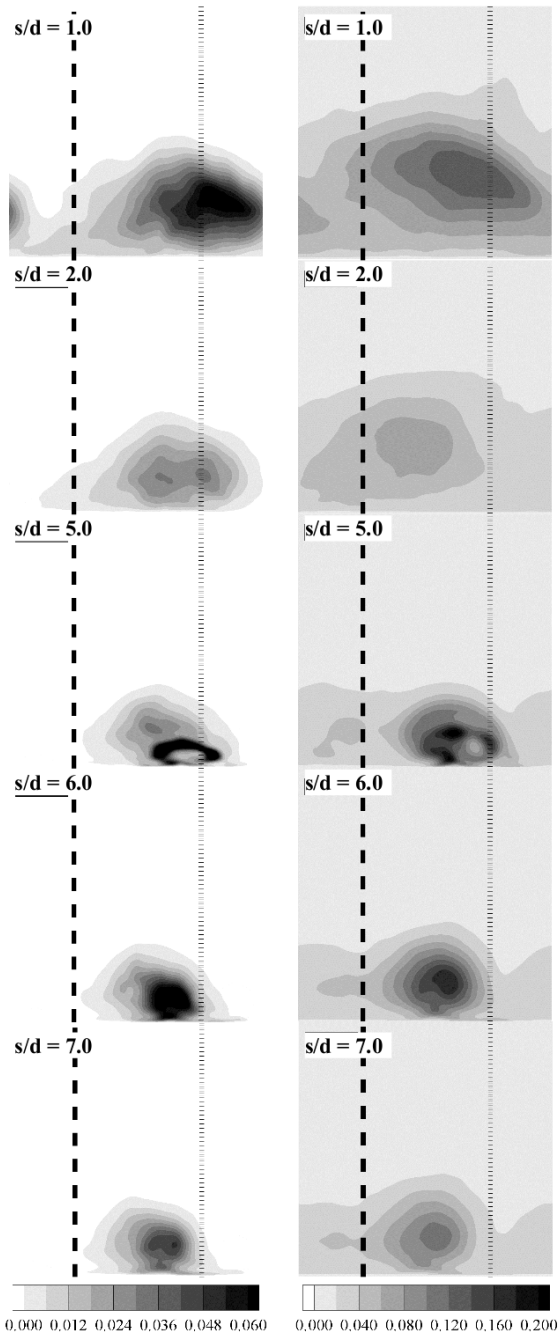

Figure 2.10.: T.K.E. contours along the stream wise direction for B.R. 0.5 (left), B.R. 1.0 (right).)

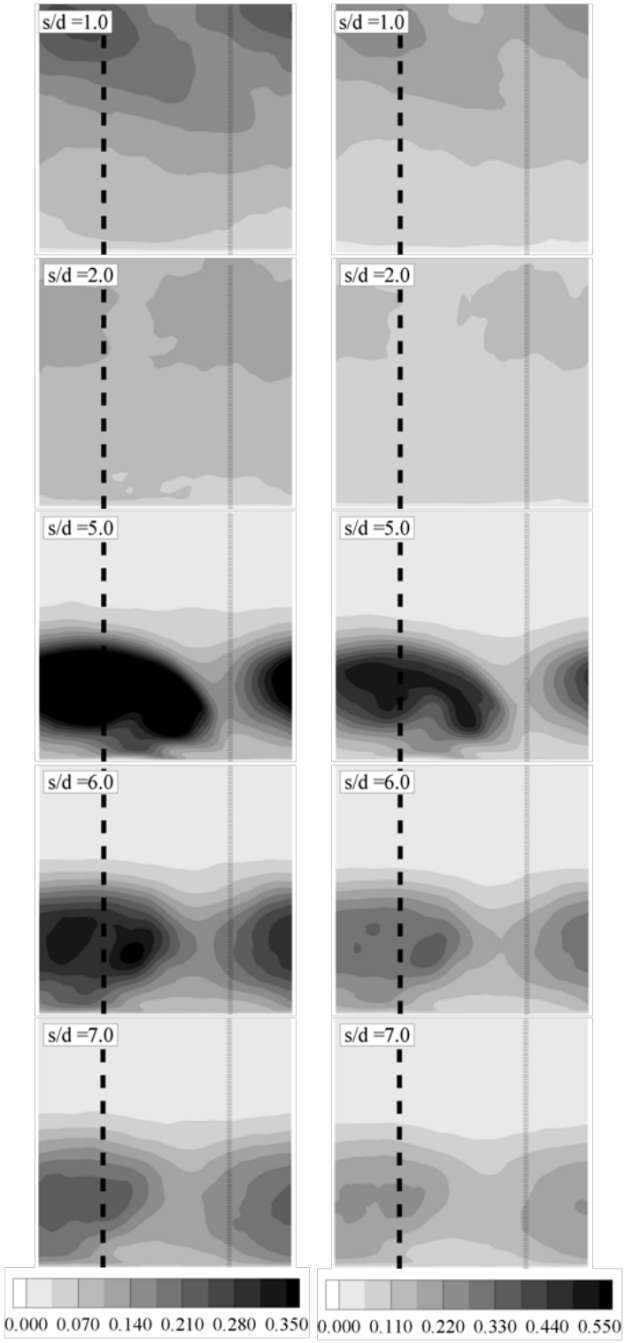

Figure 2.11.: T.K.E. contours along the stream wise direction for B.R. 1.5 (left), B.R. 2.0 (right).

Coolant injection is from right to left. Height of domain is 4.28d. Dash line is centerline of stagnation hole (z/d=-1.125); dotted line is centerline of off-stagnation hole (z/d=1.125)

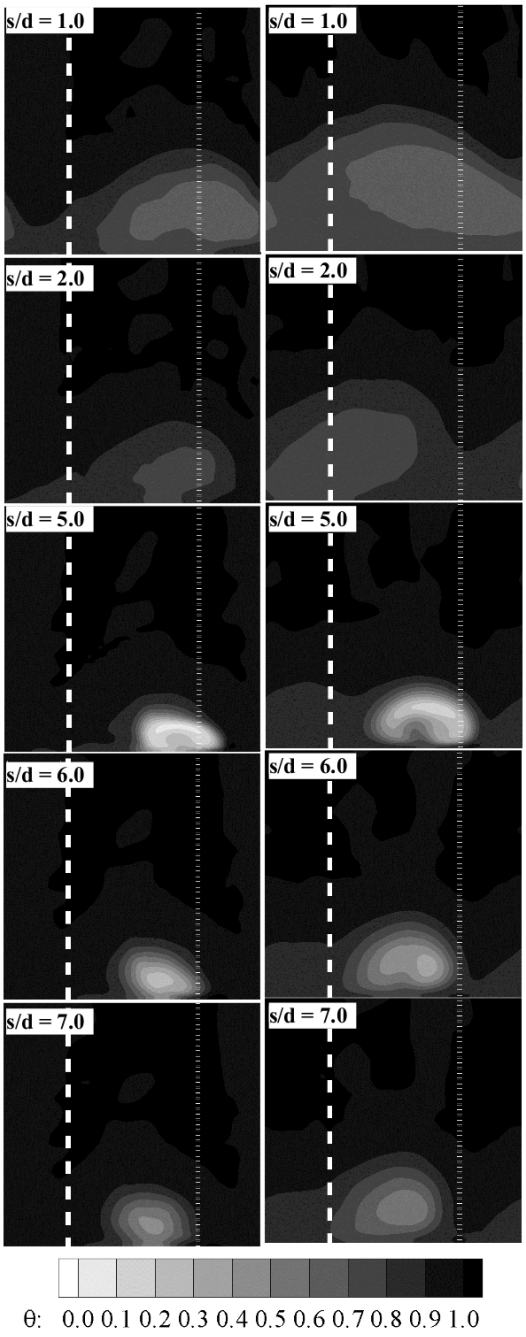

Figure 2.12.: Time-averaged temperature contours along the stream wise direction for B.R. 0.5 (left), B.R. 1.0 (right).)

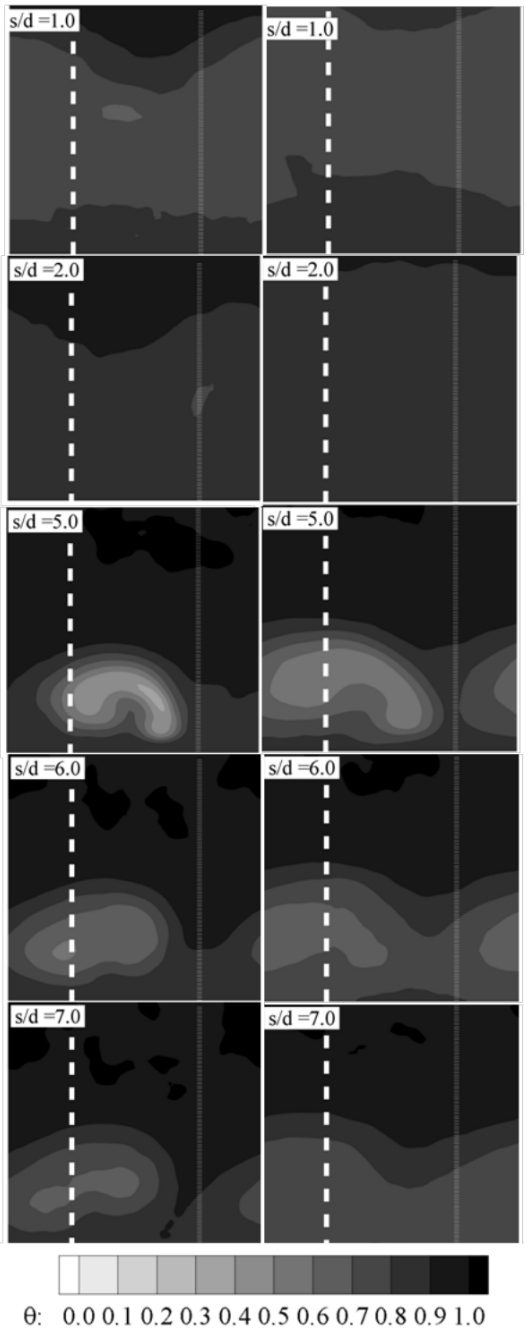

Figure 2.13.: Time-averaged temperature contours along the stream wise direction for B.R. 1.5 (left), B.R. 2.0 (right).

Coolant injection is from right to left. Height of domain is 4.28d. Dash line is centerline of stagnation hole (z/d=-1.125); dotted line is centerline of off-stagnation hole (z/d=1.125)

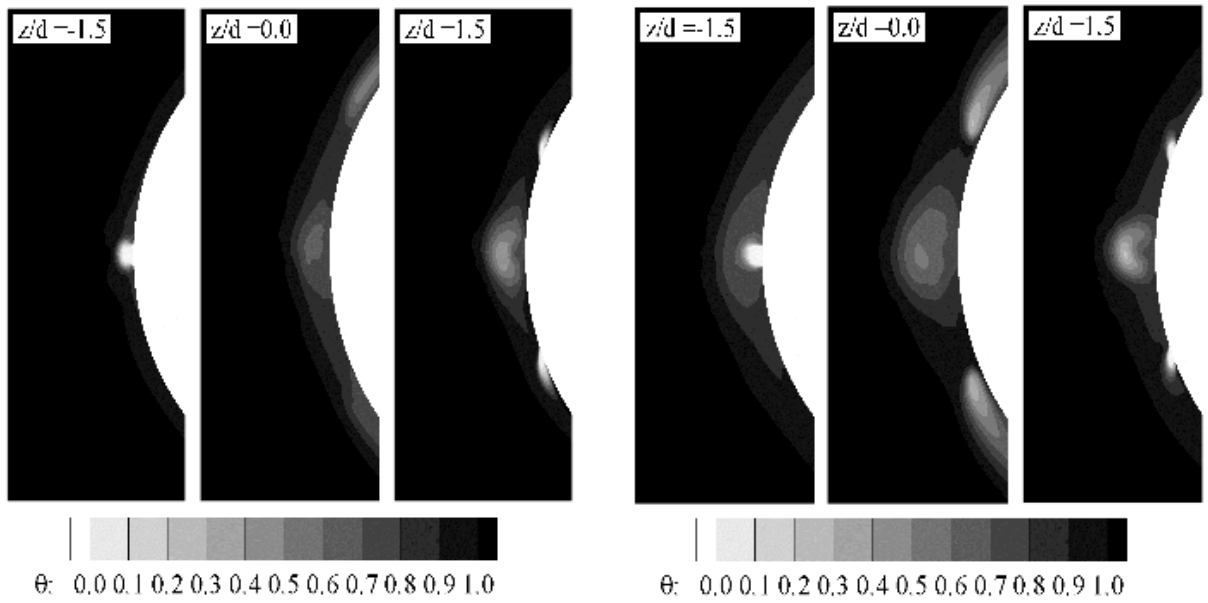

(a) (b)

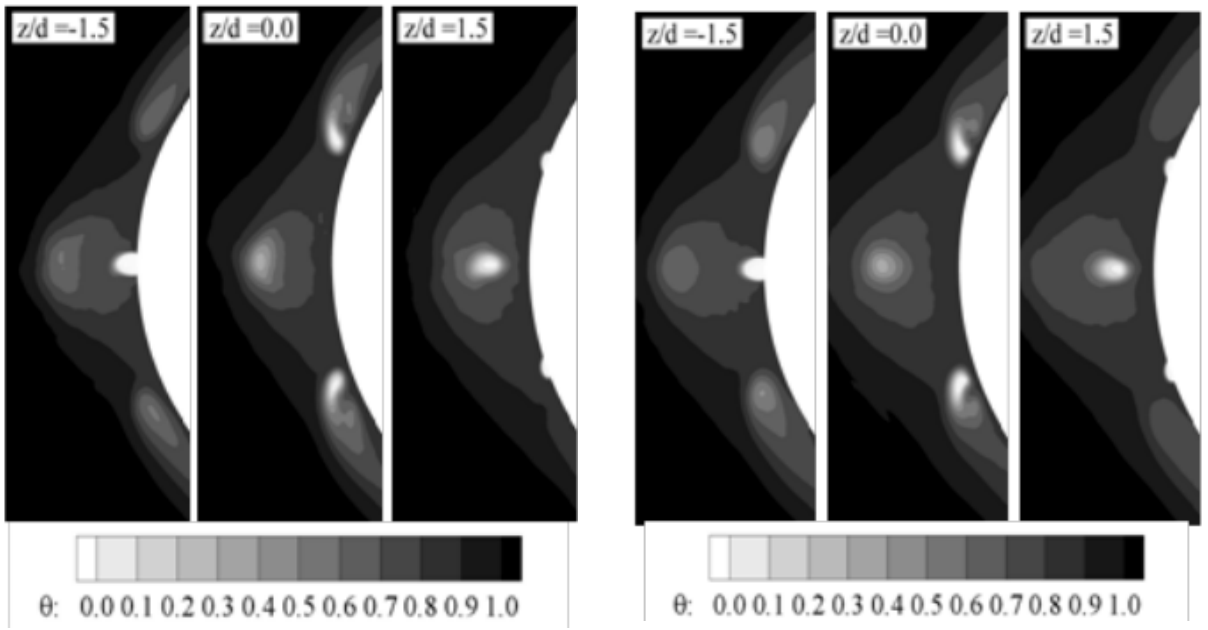

(c) (d)

Figure 2.14.: Time-averaged temperature contours at different lateral planes. (a) B.R. 0.5 (b) B.R. 1.0 (c) B.R. 1.5 (d) B.R. 2.0. Stagnation hole centerline is at z/d=-1.125 and off-stagnation hole centerline is at z/d=1.125

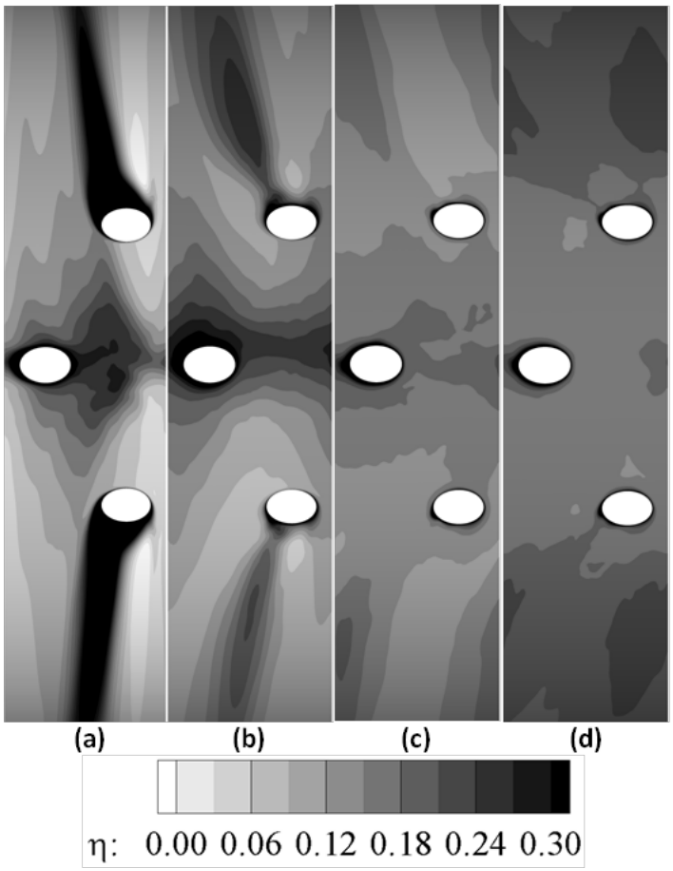

Figure 2.15.: Effectiveness on the vane surface (a) B.R. 0.5 (b) B.R. 1.0 (c) B.R. 1.5 (d) B.R. 2.0

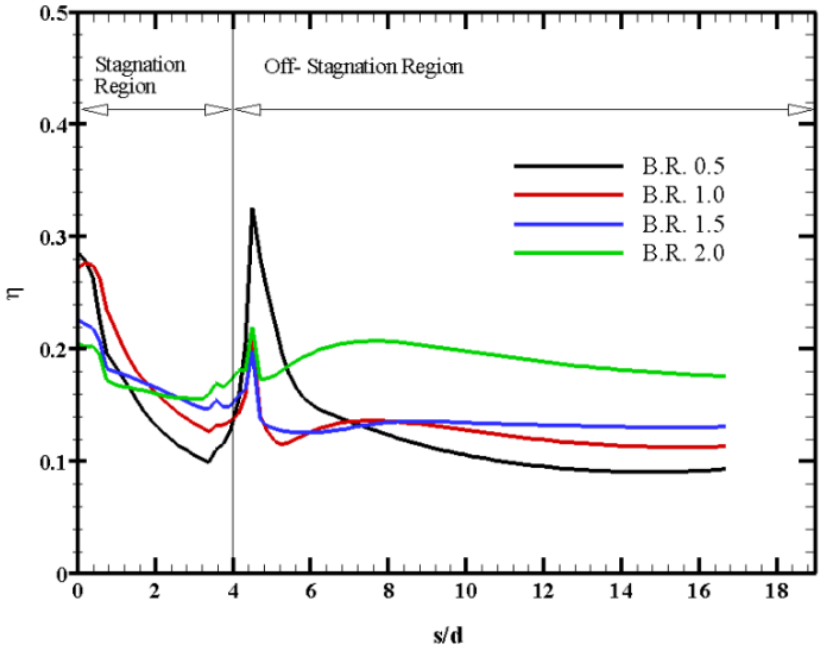

Figure 2.16.: Lateral span averaged effectiveness on the vane surface.

2.5 Conclusions

A LES investigation has been carried out on a three row leading edge vane geometry to investigate the effect of blowing ratio on the film cooling performance namely adiabatic cooling effectiveness. The following conclusions can be drawn from the present study:

- The lateral and normal penetration of the stagnation coolant jet is much stronger than the off-stagnation jets. Increasing the blowing ratio from 0.5 to 2.0, the stagnation jet penetrates farther into the mainstream At B.R. = 2.0, due to increased jet penetration into the mainstream and enhanced turbulent diffusion, there is little or no protection in the stagnation region.

- At B.R. = 0.5, the off-stagnation jet has a high effectiveness immediately downstream of injection but which quickly decays due to the small coolant mass and jet dilution. As the blowing ratio increases, an increase in jet penetration and subsequent dilution lowers the effectiveness immediately downstream of injection, but increases further downstream as the injected coolant mass increases with blowing ratio.

2.6 Bibliography

[1] Goldstein, R. J., Eckert, E. R. G., and Burggraf, F., 1974. "Effects of hole geometry and density on three-dimensional film cooling". *Int. Journal of Heat and Mass transfer,* ***17***, pp. 595–607.

[2] Bunker, R. S., 2005. "A review of shaped hole turbine film-cooling technology". *Journal of Heat Transfer,* ***127***, pp. 441–453.

[3] Mick, W. J., and Mayle, R. E., 1988. "Stagnation film cooling and heat transfer including its effect within the hole pattern". *Journal of Turbomachinary,* ***110***, pp. 66–72.

[4] Mehendale, A. B., and Hand, J. C., 1992. "Influence of high mainstream turbulence on leading edge film cooling heat transfer". *Journal of Turbomachinary,* ***114***, pp. 707–715.

[5] Ekkad, S. V., Han, J. C., and Du, H., 1998. "Detailed film cooling measurements on a cylinder leading edge model: Effect of free-stream turbulence and coolant density". *Journal of Turbomachinary,* ***120***, pp. 799–807.

[6] Johnston, C. A., Bogard, D. G., and McWaters, M. A., 1999. "Highly turbulent mainstream effects on film cooling of a simulated airfoil leading edge". *ASME Turbo Expo*(ASME Paper Number 99-GT-261).

[7] Cruse, M. W., Yuki, U. M., and Bogard, D. G., 1997. "Investigation of various parametric influences on leading edge film cooling". *ASME Turbo Expo*(ASME Paper Number 97-GT-296).

[8] Yuki, U. M., Bogard, D. G., and Cutbirth, J. M., 1998. "Effect of coolant injection on heat transfer for a simulated turbine airfoil leading edge". *ASME Turbo Expo*(ASME Paper Number 98-GT-431).

[9] Ou, S., and Rivir, R. B., 2001. "Leading edge film cooling heat transfer with high free stream turbulence using a transient liquid crystal image method". *Int. Journal of Heat and Fluid Flow,* ***22***, pp. 614–623.

[10] Simoneau, R. J., and Simon, F. F., 1993. "Progress towards understanding and predicting heat transfer in the turbine gas path". *Int. Journal of Heat and Fluid Flow,* ***14***, pp. 106–128.

[11] Chernobrovkin, A., and Lakshminarayana, B., 1999. "Numerical simulation and aerothermal physics of leading edge film cooling". *Proceedings of Institution of Mechanical Engineers,* ***213***, pp. 103–118.

[12] Lakehal, D., Theodoridis, G. S., and Rodi, W., 2001. "Three-dimensional flow and heat transfer calculations of film cooling at the leading edge of a symmetrical turbine blade model". *Int. Journal of Heat and Fluid Flow,* ***22***, pp. 113–122.

[13] York, D. W., and Leylek, J. H., 2002. "Leading-edge film cooling physics-part 1: Adiabatic effectiveness". *ASME Turbo Expo*(ASME Paper Number GT-2002-30167).

[14] Lin, Y. L., and Shih, T. I. P., 2001. "Film cooling of a cylindrical leading edge with injection through rows of compound angle holes". *Journal of Heat Transfer,* ***123***, pp. 645–654.

[15] Acharya, S., Tyagi, M., and Hoda, A., 2001. "Flow and heat transfer predictions for film cooling". *Annals of the New York Academy of Sciences,* ***934***(1), pp. 110–125.

[16] Tyagi, M., and Acharya, S., 2003. "Large eddy simulation of film cooling flow from an inclined cylindrical jet". *Journal of Turbomachinary,* ***125***, pp. 734–742.

[17] Lui, K., and Pletcher, R. H., 2005. "Large eddy simulation of discrete hole film cooling in a flat plate turbulent boundary layer". 38^{th} *AIAA Thermophysics Conference*(AIAA Paper Number 2005-4944).

[18] Iourikina, I. V., and Lele, S. K., 2005. "Towards large eddy simulation of film cooling flows on a model turbine blade leading edge". 43^{rd} *AIAA Aerospace Science Meeting and Exhibit*(AIAA Paper Number 2005-0670).

[19] Iourikina, I. V., and Lele, S. K., 2006. "Large eddy simulation of film cooling above the flat surface with a large plenum and short exit holes". 44^{rd} *AIAA Aerospace Science Meeting and Exhibit*(AIAA Paper Number 2006-1102).

[20] Guo, X., Meinke, M., and Schröder, W., 2006. "Large-eddy simulation of film cooling flows". *Computers and Fluids,* ***35***(6), pp. 587–606.

[21] Rozati, A., and Tafti, D. K., 2008. "Large-eddy simulations of leading edge film cooling: Analysis of flow structures, effectiveness, and heat transfer coefficient". *Int. Journal of Heat and Fluid Flow,* ***29***(1), pp. 1–17.

[22] Rozati, A., and Tafti, D. K., 2008. "Effect of coolant–mainstream blowing ratio on leading edge film cooling flow and heat transfer – les". *Int. Journal of Heat and Fluid Flow,* ***29***(1), pp. 857–873.

[23] Sreedharan, S. S., and Tafti, D. K., 2008. "Large eddy simulations of a three-row leading edge film cooling geometry". *Proceedings of IMECE*(ASME Paper Number IMECE2008-67019).

[24] Germano, M., Piomelli, U., Moin, P., and Cabot, W. H., 1991. "A dynamic subgrid-scale eddy viscosity model". *Physics of Fluid A,* ***3***, pp. 1760–1765.

[25] Moin, P., Squires, K., and Cabot, W. H., 1991. "A dynamic subgrid model for compressible turbulence and scalar transport". *Physics of Fluids A,* ***3***, pp. 2746–2757.

[26] Tafti, D., 2001. "Genidlest- a scalable parallel computational tool for simulating complex turbulent flows". *Proceedings of ASME Fluids Engineering Division,* ***256***.

[27] Chong, M. S., Perry, A. E., and Cantwell, B. J., 1990. "A general classification of three dimensional flow fields". *Physics of Fluids A,* ***2***(5), pp. 765–777.

[28] Arts, T., and Bourguignon, A. E., 1990. "Behavior of a coolant film with two rows of holes along the pressure side of a high-pressure nozzle guide vane". *Transactions of ASME,* ***112***, pp. 512–520.

[29] Zhang, L., and Moon, H. K., 2008. "The effect of wall thickness on nozzle suction side film cooling". *ASME Paper Number GT2008-50631.*

3. EFFECT OF BLOWING RATIO ON SYNGAS FLYASH PARTICLE DEPOSITION ON A THREE-ROW LEADING EDGE FILM COOLING GEOMETRY USING LARGE EDDY SIMULATIONS

Abstract

A numerical study is performed to investigate deposition of Syngas ash in the leading edge region of a turbine vane. The leading edge of the vane is modeled as a symmetric semi-cylinder with a flat after body. Three rows of coolant holes located at stagnation and at $\pm 21.3^{\circ}$ from stagnation are simulated at blowing ratios of 0.5,1.0,1.5 and 2.0. Large Eddy Simulation (LES) is used to model the flow field of the coolant jet-mainstream interaction and Syngas ash particles are modeled using a Lagrangian framework. Ash particle sizes of 5 and 7 micron are considered. Under the conditions of the current simulations, both ash particles have Stokes numbers less than unity of O(1) and hence are strongly affected by the flow and thermal field generated by the coolant interaction with the mainstream. Because of this, the stagnation coolant jets are quite successful in pushing the particles away from the surface and minimizing deposition in the stagnation region. Overall, about 7% of the 5 μm particles versus 14% of the 7 μm particles are deposited on the surface at B.R.=0.5. An increase to B.R.=2, increases deposition of the 5 micron particles to 10% while decreasing deposition of the 7 micron particles to 11%.

3.1 Introduction

Syngas produced from coal gasification, despite gas cleanup procedures, contains traces of flyash particles ($1\mu m$-$10\mu m$, [1–3]). The residual ash particles achieve a molten state in the gas turbine combustor and are carried through to the hot gas

A part of this work is published in IGTI ASME paper # GT09-59326

flow path. The first stage vanes are the most susceptible to damage in the form of deposition and erosion. Deposition increases the surface roughness on the vane surface and thus increases skin friction drag [4]. In the case of film-cooling, molten ash deposition build up can cause blockages in film cooling holes, leading to deterioration in effectiveness [5] and overheating of the vane. Deposited ash containing alkali sulphates, phosphates and hydroxides can also lead to corrosion. Additionally, solid ash particles can degrade the thermal barrier coating [6] by erosion and contribute to spallation of the coating. Hence, knowledge of the mechanisms responsible for deposition and erosion and methods of mitigation can help improve the operational life of the turbine components and reduce the risk of catastrophic failures.

Impaction of particulate matter (mostly ash) has received attention in past studies which have focused on the effect of particle size on impaction of the first stage stator and rotor. The trajectory of particles is governed by the action of different forces due to aerodynamic drag, lift, gravity, unsteady motion, pressure gradients, turbulent eddies, Brownian impaction of molecules, and at large temperature gradients, that of thermophoresis. Random Brownian motion is caused by bombardment of fluid molecules on the particle and thermophoretic effects are brought about by large temperature gradients. Although in most situations the drag force is dominant, other forces can dominate under certain conditions. Menguturk and Sverdrup [7] performed a modeling study on particle sizes between 0.001 - 3 μm. They modeled an Eulerian description of the particles with Brownian forces, and turbulent eddy diffusion. In this range they identified three primary mechanisms of deposition - that due to Brownian motion for d_p <0.1 μm, mixed Brownian and turbulent eddy impaction for 0.1< d_p <2 μm and eddy impaction for d_p >2 μm. Ahluwalia et al. [8] studied the adhesion or deposition of fly ash to gas turbine blades. They found that the sticking coefficient (ratio of particle deposition to particle delivery) varied from 0.0003 to 0.11 on the pressure surface and was a strong function of the gas and surface temperatures but rather insensitive to the impact angle.

Wenglarz [1] studied the major factors affecting deposition erosion and corrosion (DEC) in turbines operating with coal fuels. He identified particle size distribution and the level of molten species as two of the important parameters which need to be controlled and recommended that particles larger than 10 μm should be kept to less than 1-5 ppm for turbine erosion lifetimes substantially greater than 10,000 hours. To reduce molten deposits forming on surfaces he recommended the use of highly cooled surfaces. Stringer and Drenker [9] suggest limits of <0.1 ppm of particles >20 μm, <1 ppm for sizes 10-20 μm and <10 ppm for 4-10 μm. Particles smaller than 4 μm, were found to cause few problems.

More recently, a series of experiments were conducted at Brigham Young University to investigate deposition dynamics on a flat plate, which is representative of turbine vane. Bons et. al. [3] investigated deposition of ash particulate from synfuels like coal, petcoke, straw and sawdust on a TBC coated plate inclined at 45°. They found that the coal and petcoke particles formed large deposits (1mm -2 mm), which when cooled separated from the surface and left a thin layer ($\sim$100 μm) of deposit on the TBC. However, biomass products (straw) formed deposits with a centerline average roughness value of 40 μm, which corresponds to an increase in heat transfer coefficient by 20% and an increase in skin friction drag by 140% on a representative turbine vane ($Re_c \sim 1 \times 10^6$). Following this, Wammack et. al. [10] investigated deposition dynamics on different surface treated samples. The samples under study were: 1) Bare polished metal (average roughness $\sim 0.1\mu m$) 2) Polished TBC with bondcoat (average roughness $\sim$ 0.6 μm), 3) Unpolished oxidation resistant coating with bondcoat (average roughness $\sim$ 16 μm). They found that the initial surface treatment affected the evolution of deposition. After a two hour test, bare polished metal did not hold the deposit when the plate was cooled (thermal cycling). They also found the particle deposits penetrating the TBC significantly, lead to potential spallation. Later, Crosby et. al. [11] investigated the effect of ash particulate deposition as a function of particle size (3 μm -16 μm), gas temperature (860° C - 1183° C) and backside impingement cooling of the plate. A more obvious conclusion observed was,

increasing the particle size increases the deposition in a non-linear fashion. Moreover, lowering the frontside surface temperature by 100° C, through backside cooling, reduces the deposition thickness by a factor of 4. These results opened avenues to see the effect of deposition on a film cooled plate. Ai et. al. [12] investigated ash particle deposition on film cooled plate. They evaluated the influence of coolant hole shape, spacing and coolant to mainstream blowing ratio on deposition. They report that the metal surface temperature significantly alters the capture efficiency which is defined as the ratio of the amount of deposit to the amount of ash fed into the reactor. For the cylindrically shaped holes, as the blowing ratio increased from 0.5 to 2.0, the capture efficiency decreases by 40%. However, the capture efficiency is higher, by an order of magnitude, for a target material coated with TBC than for the polished bare metal. All the above studies summarize factors that affect the extent of deposition on the turbine vane surface including gas temperature, surface temperature, blowing ratio, particle size and composition and the geometric properties of the vane surface.

Recent work on deposition in turbomachines is summarized in a review paper by Hamed et al. [13]. Review includes an extensive pool of studies on deposition conducted experimentally and numerically. The experiments found the amount of deposition was a function of particle inertia and temperature.

There have been few numerical studies of deposition. Shah and Tafti [14] also used Lagrangian particle dynamics to compute the deposition and erosion in a ribbed internal cooling duct. The turbulence in the flow field is resolved using the LES technique that provided a firm theoretical basis for modeling particle trajectories. Results presented particle impingement locations, impact velocity, impact angles for sand particles sizes of 10 μm, 50 μm and 100 μm.

The leading edge of the first stage nozzle guide vane is one of the most vulnerable sections to deposition. While most past studies have focused on particle impaction in the first stage stator and rotor, the objective of this paper is to investigate the dynamics of ash deposition and erosion in a leading edge vane geometry with film cooling. LES is used for resolving the turbulent interaction between film cooling

jets and the mainstream flow with Lagrangian particle dynamics to simulate the ash particles. This follows an earlier study [15] which investigated film-cooled geometry with two rows of holes on either side of stagnation. It was established that the particles with Stokes numbers much less than unity did not pose a serious threat to deposition, whereas particles at higher Stokes numbers (>1) impacted the surface by virtue of their inertia and jet blowing ratio (up to 1.2) did have not have a substantial impact on their trajectories. Particles with Stokes number of O(1) were found to be the most amenable to manipulation by the coolant jets. The current study is an extension of [15] but for a more realistic three-row cooling geometry at the leading edge and for coolant blowing ratios ranging from 0.5 to 2.0. Two ash particle sizes of 5 μm and 7 μm are investigated.

3.2 Methodology

The solution methodology used to obtain the effect of blowing ratio on syngas flyash particle is two fold. First, a high resolution LES is used to solve for flow field dynamics for each blowing ratio. Second, a Lagrangian tracking algorithm is used to track the syngas flyash particles which are injected in the flow field. This section states the governing equations used for the carrier phase and dispersed phase, the computational model, flyash properties and the flow conditions.

3.2.1 Governing equations: Carrier Phase

The governing transport equations which include the incompressible mass, momentum and energy conservation are solved in a generalized body-fitted coordinate system. The equations are non-dimensionalized using a characteristic length scale D, characteristic velocity scale U_∞, and a characteristic temperature scale $(T_\infty - T_c)$. The non-dimensional time dependent equations are as follows:

Continuity

$$\frac{\partial}{\partial \xi_j}\left(\sqrt{g}\bar{U}^j\right) = 0 \tag{3.1}$$

Momentum

$$\frac{\partial}{\partial t}\left(\sqrt{g}\bar{u}_i\right) + \frac{\partial}{\partial \xi_j}\left(\sqrt{g}\bar{U}^j\bar{u}_i\right) = -\frac{\partial}{\partial \xi_j}\left(\sqrt{g}(\vec{a}^j)_i\bar{p}\right) + \frac{\partial}{\partial \xi_j}\left(\left(\frac{1}{Re}+\frac{1}{Re_t}\right)\sqrt{g}g^{jk}\frac{\partial \bar{u}_i}{\partial \xi_k}\right) \tag{3.2}$$

Energy

$$\frac{\partial}{\partial t}\left(\sqrt{g}\bar{\theta}\right) + \frac{\partial}{\partial \xi_j}\left(\sqrt{g}\bar{U}^j\bar{\theta}\right) = \frac{\partial}{\partial \xi_j}\left(\left(\frac{1}{PrRe}+\frac{1}{Pr_tRe_t}\right)\sqrt{g}g^{jk}\frac{\partial \bar{\theta}}{\partial \xi_k}\right) \tag{3.3}$$

where $\vec{a}^i$ are the contravariant basis vectors [*] , $\sqrt{g}$ is the Jacobian of the transformation, $g^{(ij)}$ is the contravariant metric tensor, $\sqrt{g}U^j = \sqrt{g}(\vec{a}^j)_i u_i$ is the contravariant flux vector, u_i is the Cartesian velocity vector, and θ is the non-dimensional temperature. The overbar in the continuity, momentum and energy equations denote grid filtered quantities. Re_t is the inverse of the non-dimensional turbulent eddy-viscosity and is obtained by the Smagorinsky model.

$$\frac{1}{Re_t} = C_s^2(\sqrt{g})^{(2/3)}|\bar{S}|$$

where $|\bar{S}|$ is the magnitude of the strain rate tensor given by $|\bar{S}| = \sqrt{(2\bar{S}_{ik}\bar{S}_{ik})}$. The Smagorinsky constant C_s^2 is obtained via the dynamic procedure [16] and is contrained to be positive. The turbulent Prandtl number is assumed to have a constant value of 0.5 [17].

3.2.2 Governing equations: Dispersed Phase

The dispersed phase is modeled in the Lagrangian framework. The model currently used has been described in [18]. The model is implemented in an unstructured multiblock, multiprocessor framework and validation in turbulent channel flow has been reported in [14]. The particle sizes investigated in this study are in the range of 1 - 10 μm. In this range of particle sizes, among all the forces acting on the particle,

[*]The notation $(\vec{a}^j)_i$ is used to denote the i-th component of vector $\vec{a}^j$, $(\vec{a}^j)_i = \partial \xi_j / \partial x_i$

drag force dominates the particle motion [2]. Additionally, in practical situations the concentration of flyash particles are very dilute in the mainstream, hence inter particle interactions and particle-to-fluid interactions are neglected. The equations for particle motion and temperature in non-dimensional form are as follows:

Motion

$$\frac{du_i^p}{dt} = -\frac{1}{St_p}\left(1 + 0.15Re_p^{0.687}\right)\left(u_i^p - u_i^f\right) \tag{3.4}$$

Location

$$\frac{dx_i^p}{dt} = u_i^p \tag{3.5}$$

Energy

$$\frac{d\theta^p}{dt} = \frac{1}{St_{conv}}\left(\theta^f - \theta^p\right) + \frac{1}{St_{rad}}\left(1 - \theta^p\right) \tag{3.6}$$

where St_p is the particle momentum Stokes number defined as $St_p = \frac{(\rho_p^* d_p^{*2} U_{jet}^*)}{(18\mu L_c^*)}$, St_{conv} is the particle convective thermal Stokes number defined as $St_{conv} = \frac{(\rho_p^* c_p^* d_p^* U_{jet}^*)}{(6hL_c^*)}$, St_{rad} is the particle radiative thermal Stokes number defined as $St_{rad} = \frac{(\rho_p^* c_p^* d_p^* U_{jet}^*)}{(6h_r L_c^*)}$, with the effective radiative heat transfer coefficient defined as $h_r = \epsilon\sigma(T_p + T_a)(T_p^2 + T_a^2)$[†]. The momentum and convective Stokes numbers are defined assuming low relative particle Reynolds number ($Re_p < 1$), $C_d = 24/Re_p$ and $Nu_p = 2.0$ [19].

3.3 Computational model

3.3.1 Geometry description

The computational domain models the leading edge of a vane as a semi-cylindrical form with a flat after body. Three rows of film cooling holes are employed. One row is located at stagnation and two rows are located at ±4d, on either side of the stagnation line. The lateral pitch spacing (P) between two holes for any given row is 4.5d, and the relative position of the holes on the upper half and lower half are staggered with respect to the stagnation hole. The origin is fixed at the center of the

[†]For an estimate of lowest radiative Stokes number ($T_p = T_\infty$)

domain at stagnation with the stagnation hole located at z = -1.125d and staggered off-stagnation holes located at z = 1.125d. The coolant hole diameter ratio (D/d) is 21.5 and the length ratio of the coolant pipe (L/d) is 10.75 . The coolant is injected laterally at 45° to the surface with a compound angle of 90° to the mainstream. Figure 3.1 shows the head-on view of the leading edge model. The dotted line shows the computational domain. Figure 3.2 shows the computational domain of interest as the shaded region. It extends 10D in the x-direction, 5D in y-direction and 4.5d in the spanwise z-direction.

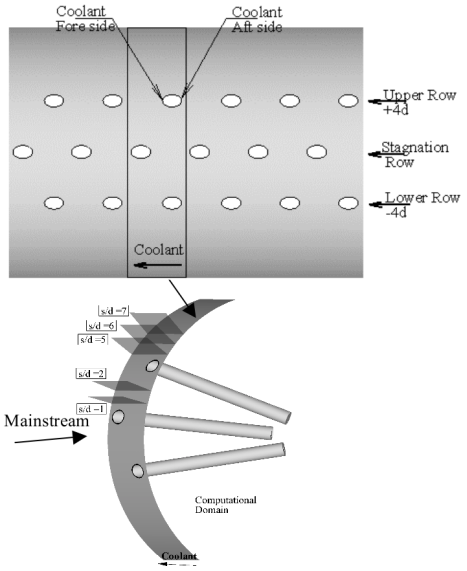

Figure 3.1.: Leading edge vane model and near field streamwise planes used in presenting results.

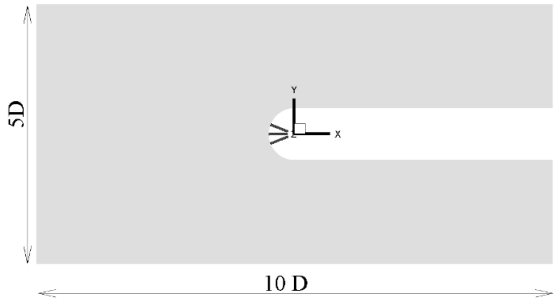

Figure 3.2.: Computational domain in side view (X-Y plane)

Table 3.1: Leading edge geometry and flow properties

Leading Edge Geometry	
Blade leading edge diameter (D^*) $[m]$	0.01
Coolant jet diameter (d^*) $[m]$	4.65×10^{-4}
Span-wise pitch (p^*/d^*)	4.5
Flow Properties	
Free stream velocity (U^*_∞), $[m/s]$	40
Free stream temperature (T^*_∞), $[K]$	1600
Free stream pressure (P^*_∞), $[atm]$	20
Free stream density (ρ^*_∞), $[kg/m^3]$	4.4
Particle density (ρ^*_p), $[kg/m^3]$	2500
Particle Specific heat (c^*_p), $[J/kgK]$	250
Coolant temperature (T^*_j), $[K]$	775
Ash softening Temperature, $[K]$	1500
Coolant-to-mainstream density ratio	2.071
Coolant-to-mainstream blowing ratio (U^*_j/U^*_∞)	0.5, 1.0, 1.5, 2.0

Table 3.2: Particle Stokes number

d^*_p (μm)	St_p	St_{conv}	St_{rad}
5	0.25	0.0578	2.24
7	0.49	0.113	3.14

The flow conditions and the particle properties used to compute the Stokes number are tabulated in [Table 3.1] . The Stokes number signifies the time that a

Computations assumes a coolant to mainstream density ratio of 1 (Table 3.1)

particle takes to respond to a local change in the fluid velocity (momentum stokes number) or fluid temperature (thermal stokes number). A Stokes number much less than 1 indicates that the particle responds to the changes in the fluid surrounding it almost instantaneously. And a Stokes number greater than 1 indicates that the particle takes a long time to adjust to changes in surrounding fluid. The momentum and the thermal Stokes number for the particle sizes considered in this study are tabulated in Table 3.2.

3.3.2 Boundary conditions

The adiabatic wall approach is used to predict the adiabatic wall temperature and effectiveness. Therefore, the surface is maintained at zero wall flux, the non-dimensional coolant temperature is set to 0 and the non-dimensional mainstream temperature is set to 1. Periodic boundary conditions are applied in the span (z-direction) to simulate an infinite row of holes. To simulate a linear cascade arrangement, periodic boundary conditions are also applied in the y-direction (figure 3.2). No penetration and no slip conditions are applied on the vane surface and on the coolant pipe wall. The mainstream inlet condition is a constant velocity profile with no turbulence intensity and a convective outflow boundary condition is applied at the exit. The inlet boundary condition for the coolant pipe is also a constant velocity profile applied normal to the cross-section of the pipe.

The particles are injected 0.36D upstream of the leading edge extending the full lateral dimension of the computational domain and 0.35D on either side of the symmetry plane (or stagnation line). Hence the total coverage is 70% of the projected area of the leading edge. The coverage was not extended to the full projected area because trial runs showed that particles injected outside of the 0.7D envelope did not interact with the vane surface but simply flowed around the leading edge as the flow diverged on approach to the leading edge. A total number of 362,500 particles are injected at this location. Initially upon particle injection, the particle velocities and temperatures are set to the same as fluid velocity and temperature. Subsequently,

the governing equations of motion of these particles are integrated using a third order Adams-Bashforth method in the Lagrangian frame of reference to obtain the velocity, location, and temperature. Molten particles in the free-stream at T=1600K deposit on the vane surface if their temperature is above the ash softening temperature of 1500K. If the particles are cooled below the softening temperature they are assumed to be solid and behave as erosive particles.

In the present study, the free stream Reynolds number based on leading edge diameter and the free stream velocity is 32,000. The effect of coolant to mainstream blowing ratio of 0.5, 1.0, 1.5 and 2.0, on ash particle sizes of 5 μm and 7 μm is investigated.

3.3.3 Solver controls

The simulation uses the in-house conservative finite volume code, GenIDLEST (Tafti [20]). The carrier phase (fluid) is computed using LES and the discrete phase (particles) is solved using the Lagrangian particle tracking algorithm [18]. The discretization of the governing equations (carrier phase) uses a second order central difference scheme on a non-staggered grid topology. The convergence criterion for the momentum, pressure and the energy are 1×10^{-6}, 1×10^{-6} and 1×10^{-6} respectively at each time step. The time step is set at 7×10^{-5} for B.R. = 0.5 and B.R. = 1.0 and 6×10^{-5} for B.R. =1.5 and B.R. = 2.0. The flow is first allowed to develop and averaged for more than 20 non-dimensional time units before the particles are injected in the freestream. The trajectories of the particles injected are based on the instantaneous flow field. The particles are tracked and allowed to run until all the particles cross the plate. All the results shown here are computed using 160 processors on Virginia Techs high performance terascale supercomputing facility: SYSTEM X.

3.4 Discussion of results

The flow and temperature field generated by the coolant jet and mainstream interaction are crucial to the aero-thermal behavior of particles and whether they deposit on the surface. The aerodynamics of jet-mainstream interaction can either push the particle away from the vane surface or entrain the particle near the surface. In the same manner, the thermal field generated by the jet-mainstream interaction influences the temperature of the particle. The momentum stokes number governs the particle trajectory, whereas the response time for the particles to the changes in temperature within the flow field is regulated by the thermal stokes number. The coolant jet mainstream mixing produces turbulent eddies which not only alter the particle trajectory but also change the particle temperature. If the thermal Stokes number is small, any interaction of the particle with the coolant jet will lower its temperature below the softening temperature.

3.4.1 Flow and thermal field

To get an insight of the coolant jet mainstream mixing, instantaneous coherent structures of turbulence are shown. Figure 3.3 shows the iso-vorticity coherent turbulent structures for coolant to mainstream blowing ratio of 0.5 and 2.0. These structures are extracted by using the vortex eduction procedure by Chong et al. [21]. The magnitude (iso-vorticity value, Figure 3.3) of the iso-vorticities represent the strength of the vortices. At low blowing ratio (B.R. = 0.5), the vortical coherent structures are well defined. A ring vortex generated at the stagnation jet convects along the stagnation line which then destabilizes and moves downstream of the vane surface under the influence of the accelerating mainstream flow. The vortex generated by the off-stagnation holes quickly aligns to the vane surface and protection extends to a fraction of the pitch. This occurrence is again caused by the influence of accelerating mainstream flow. As the blowing ratio is increased (B.R. = 2.0), the coolant jet penetrates further into the mainstream and is diluted by turbulent diffusion. At

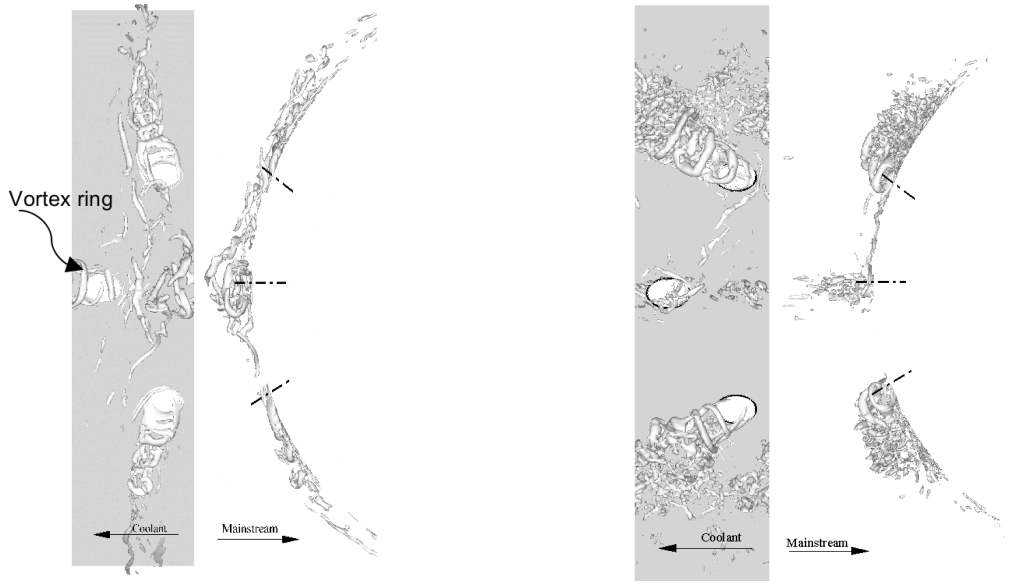

(a) Front View Side View (b) Front View Side View

Figure 3.3.: Structure of coherent vorticity (a) B.R. 0.5 (Iso-surface value = 30) (b) B.R. 2.0. (Iso-surface value = 75)

this high blowing ratio, the little coherence that is seen in figure 3.3a, disintegrates to form small scale vortical structures.

Figure 3.4 shows the contours of adiabatic effectiveness that is achieved by the film cooling on the vane surface to protect the vane surface from high temperatures at different coolant to mainstream blowing ratio. Figure 3.5 shows the line plots of laterally averaged adiabatic effectiveness along the span of the vane surface as a function of downstream location (s/d). The spanwise average is found by averaging across the upper and lower halves of the geometry. The surface adiabatic effectiveness in the stagnation region is a function of the jet penetration and mixing and the amount of coolant injected. At B.R.=0.5, jet penetration into the mainstream is the smallest amongst the different blowing ratios resulting in the least amount of mixing. Hence it has the largest effectiveness at the stagnation line. However, because of the larger injected mass at B.R.=1.0 and the redirection of the coolant to the vane surface, the

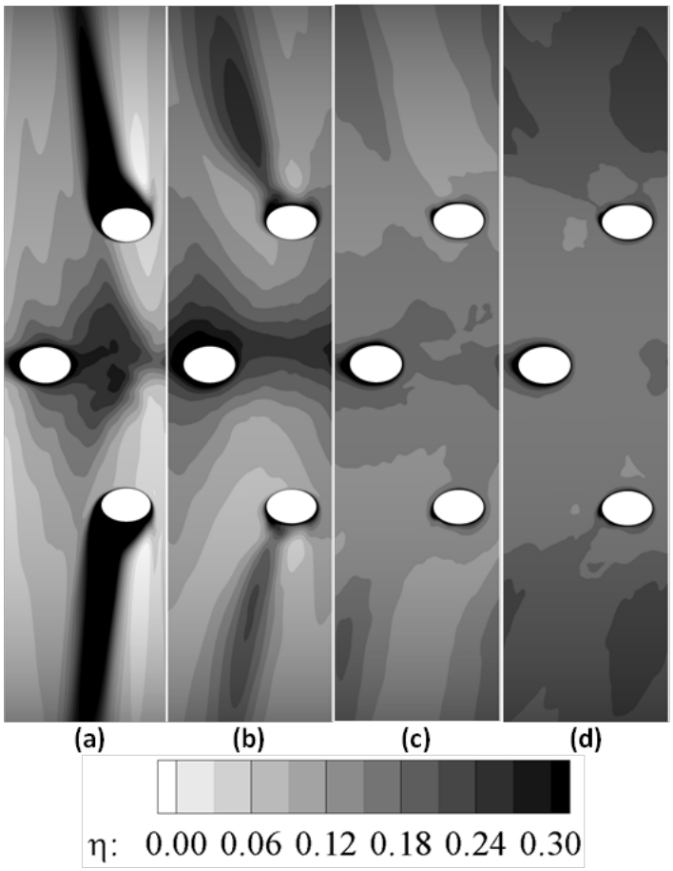

Figure 3.4.: Effectiveness on the vane surface (a) B.R. 0.5 (b) B.R. 1.0 (c) B.R. 1.5 (d) B.R. 2.0

adiabatic effectiveness downstream of the stagnation line is higher than B.R.=0.5. As the blowing ratio increases further to 1.5 and 2.0, the effectiveness decreases in the immediate vicinity of the stagnation line as the jet penetrates further into the mainstream but increases downstream of stagnation.

The behavior of the adiabatic effectiveness follows the same principles downstream of the second row of injection. There is a balance between injected coolant mass and jet penetration and mixing. At the lowest blowing ratio of 0.5, the injected coolant remains close to the surface and provides the highest effectiveness immediately downstream of injection. However the effectiveness decays rapidly, as a result of the smaller mass of coolant and lower lateral spreading of the coolant. As the blowing ratio increases to 1.0, the larger initial penetration of the jet into the mainstream reduces the effectiveness immediately downstream of injection, but which increases

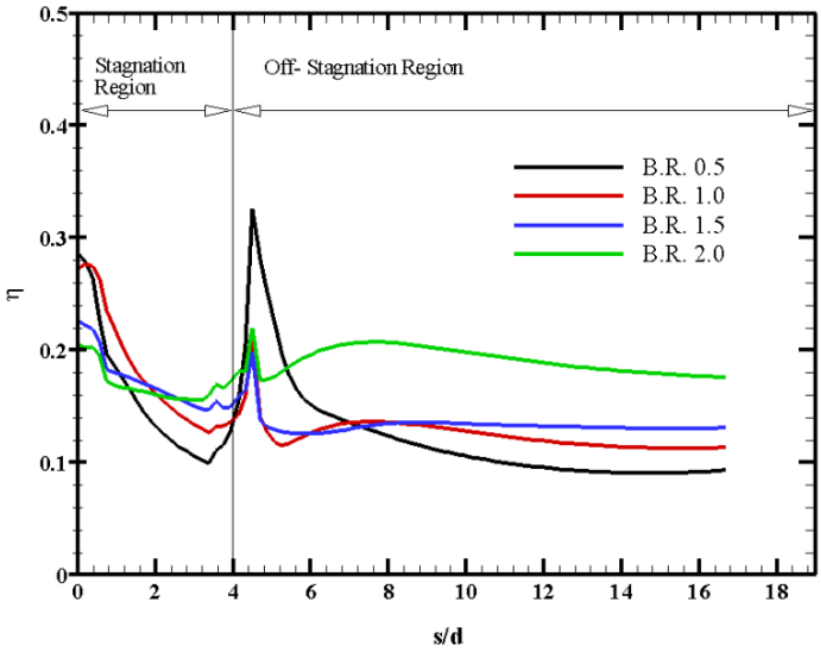

Figure 3.5.: Lateral span averaged effectiveness on the vane surface.

as the coolant is pushed back to the surface. At B.R.=1.5, the penetration into the mainstream is larger but because of the larger coolant mass, the redirection of coolant back to the surface dominates downstream, and increases the effectiveness. Similar to B.R.=1.5, at B.R.=2.0, in spite of the high T.K.E. generated and the intense mixing between the jet and the mainstream, the larger coolant mass injected and the larger lateral spread of the jet dominates the adiabatic effectiveness at the surface.

3.4.2 Deposition

Deposition on the vane surface is influenced by whether the coolant jets are successful in blowing the particles away from the surface or whether the particles approaching the surface are cooled to a solid phase. In the present chapter, the deposition model uses the softening temperature of the flyash particles (Table 3.1) as the criterion for deposition. If the temperature of the particle colliding with the surface is more than the softening temperature then that particle is deposited on the surface. If the particle temperature is lower than the softening temperature it

undergoes an elastic collision with the vane surface and is denoted as an erosive particle.

Figure 3.6 shows the percentage of particles being deposited on the vane surface. Both, the 5 μm and 7 μm particles are sensitive to the blowing ratio as the momentum Stokes number for both particle sizes are less than unity [Table 3.2]. At B.R. = 0.5, the stagnation jet blows the particles (5 μm and 7 μm) in the lateral direction. The stagnation coolant jet remains attached and confined to the stagnation line [figure 3.3a]. The deposition of the particles is seen above and below the core of the stagnation coolant jet [figure 3.6]. The vortical structures formed in the stagnation region alter the particle trajectories such that they follow the vortex streams. Most of these particles have enough residence time to be cooled below the softening temperature and hence do not deposit in the stagnation region and along the coolant path. At B.R.=0.5, the coolant exiting from the off-stagnation jet also stays attached to the surface (figure 3.3a) and protects part of the pitch from deposition along the coolant path. The 7 μm particles on account of their higher momentum and thermal Stokes numbers, show more deposition over a larger area between coolant paths.

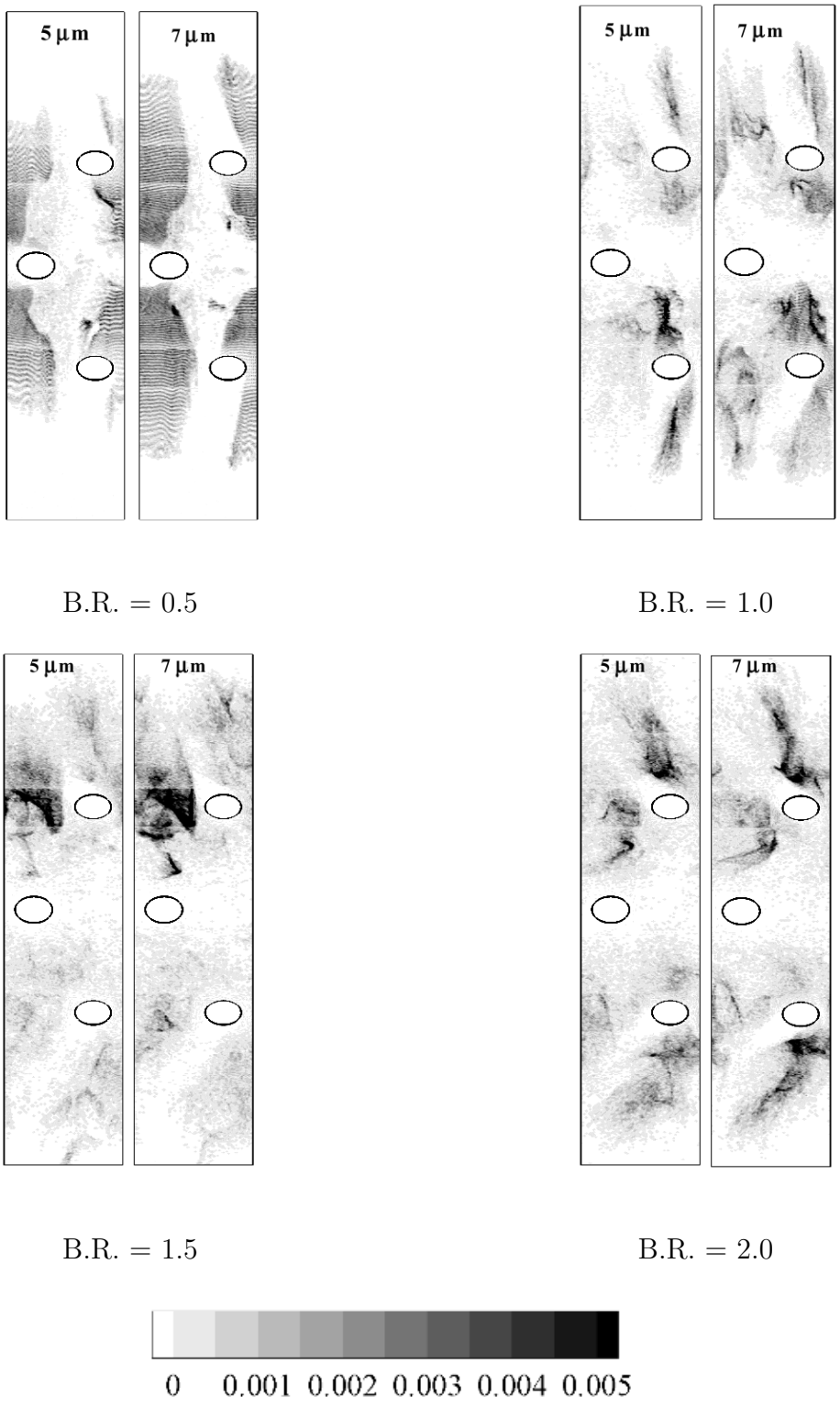

Figure 3.6.: Percentage of particles depositing on leading edge vane surface (direction of coolant is from right to left)

Increasing blowing ratio decreases the effectiveness in the stagnation region (figure 3.6). As the blowing ratio is increased to 1, 1.5 and 2.0, the coolant core laterally penetrates further into the mainstream. The penetration is much larger at the stagnation row which has two effects conducive to protecting the surface from deposition. First, the increased momentum of the coolant jets succeed in blowing the particles away from the stagnation region, and second, the particles are in contact with the coolant (albeit mixed with free-stream) long enough to lower their temperature below the softening temperature. In spite of the surface temperature increasing with blowing ratio in the stagnation region (decreasing effectiveness), very few particles reach the surface in the stagnation region. However, immediately downstream of the stagnation hole there is a heavy deposit concentration for B.R.=1.5 and 2.0. Animations at B.R.=2.0 shows that a fountain flow is set up in the stagnation region. The stagnation jets entrain particles from near the surface on either side, blow them away from the surface, most of which are pushed back to the surface on encountering the opposing free-stream flow on either side of stagnation. During this cycle, when in contact with the stagnation jet on the outward trajectory, the particles are cooled to below the softening temperature. However once the particles are pushed into the freestream they once again heat up above the softening temperature and when pushed back toward the vane surface, deposit on either side of stagnation immediately downstream of the stagnation hole. The deposits due to this phenomenon are especially heavy at B.R.=1.5. Although not observed directly, it is suspected that the same phenomenon is responsible for the heavy deposits immediately upstream of the off-stagnation hole at B.R.=1. The shift in lateral location can be attributed to the lower lateral momentum of the stagnation jet at B.R.=1.0. An additional effect which is evident is, as the blowing ratios increase, deposition also increases on the aft-side of the off-stagnation jets. This is a region of entrainment of hot freestream fluid, which intensifies as the blowing ratio increases and the jet lifts off the surface. The entrained mainstream fluid carries ash particles with it which deposit on the surface.

Some particles penetrate into the coolant holes, but they are cooled quickly to below their softening temperature resulting in no deposition.

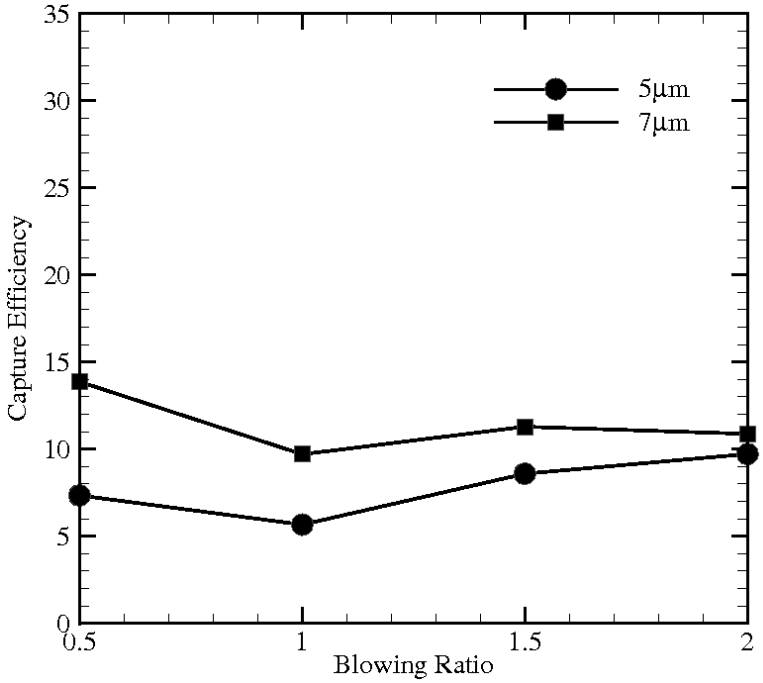

Figure 3.7.: Capture efficiency as a function of B.R.

Overall deposition is a function of the particle Stokes numbers (momentum and thermal), blowing ratio, and the softening temperature in relation to the mainstream and coolant temperatures. Figure 3.7 shows the capture efficiency for the 5 and 7 μm particles as a function of blowing ratio. Capture efficiency is defined as the percentage of particles that deposit to the total number of particles injected which spans the projected vane area at the inlet. In the present case, the plane of particle injection covers 70% of the projected vane area and the remaining 30% is assumed to disperse and flow with the streamlines without interacting with the vane surface. The graph in figure 3.7 shows 7% of the 5 μm particles versus 14% of the 7 μm particles are deposited on the surface at B.R. 0.5. At this blowing ratio the coolant path covers a fraction of the vane pitch and the simulated deposition is purely due to inertial impaction of the particles in the areas where there is little or no presence of film cooling. At B.R.=1, there is a decrease in deposition for both particle sizes,

which is due to the presence of film cooling. However, as the blowing ratio increases to 1.5, deposition increases. This can be attributed to particles that are caught up in the asymmetrical vortex pair causing mainstream entrainment beneath the coolant jet. A further increase in blowing ratio to 2.0 results in a slight decrease in deposition for the larger particles but results in an increase for the 5 μm particles. A clear trend in the results is the relative insensitivity of deposition on particle size or Stokes numbers (both less than unity but of O(1) for momentum and of O(0.1) for thermal) as the blowing ratio increases. Another clear trend for both particle sizes is that an optimal blowing ratio exists at which deposition is minimized (B.R. $\sim$ 1.0) in the leading edge region.

3.5 Conclusions

Computational studies have been carried out on a three-row leading edge vane geometry to investigate ash deposition for particle sizes of 5 and 7 μm and jet to mainstream blowing ratios of 0.5, 1.0, 1.5 and 2.0. The simulations use LES for an accurate representation of the highly turbulent flow field with Lagrangian dynamics for the ash particles.

The momentum Stokes number is the single most important parameter which regulates the particle trajectory in the flow field by its response to the flow field surrounding it followed by the jet-mainstream blowing ratio. While the momentum Stokes number is a good indicator of whether an ash particle gets near the vane surface, the thermal Stokes number together with the ash softening temperature in relation to the mainstream, coolant, and surface temperature govern whether an ash particle deposits on the surface. The amount of coolant mass injected or B.R. also has an effect.

Under the conditions of the current simulations, both ash particles have Stokes numbers less than unity of O(1) and hence are amenable to be strongly affected by the flow and thermal field generated by the coolant interaction with the mainstream.

Because of this, the stagnation coolant jets are quite successful in pushing the particles away from the surface and minimizing deposition in this region.

Deposition is concentrated downstream of the stagnation row in regions where particles entrained into the stagnation coolant jets are pushed out into the mainstream, are heated up and are pushed back down on to the surface where they deposit. As the blowing ratio increases, the aft side of the off-stagnation coolant path is susceptible to deposition due to the strong mainstream entrainment in this region which carries particles to the wall. Overall, about 7% of the 5 μm particles versus 14% of the 7 μm particles are deposited on the surface at B.R. 0.5. At B.R.=1, there is a decrease in deposition for both particle sizes, but which increases as the blowing ratio increases to 1.5. A further increase in blowing ratio to 2.0 results in a slight decrease in deposition for the larger particles but results in an increase for the 5 μm particles. A clear trend in the results is the relative insensitivity of deposition on particle size or Stokes numbers (both less than unity but of O(1) for momentum and of O(0.1) for thermal) as the blowing ratio increases. Another clear trend for both particle sizes is that an optimal blowing ratio exists at which deposition is minimized (B.R. $\sim$ 1.0) in the leading edge region.

Overall, for particles of size 5 μm, there is a combined increase in deposition and erosive particles (see § Appendix D) from 11% to 17% as the blowing ratio increases from 0.5 to 2.0. The 7 μm particles, on the other hand decrease from 24% to about 21% as the blowing ratio increases from 0.5 to 2.0.

3.6 Bibliography

[1] Bunker, R. D., 1985. "Deposition, erosion and corrosion protection for coal-fired gas turbine". *ASME Paper Number 85-IGTI-61.*

[2] Tabakoff, W., 1991. "Measurements of particles rebound characteristics on materials used in gas turbines". *Journal of Propulsion,* ***7***(5), pp. 805–813.

[3] Bons, J. P., Crosby, J., Wammack, J. E., Bentley, B. I., and Fletcher, T., 2005. "High pressure turbine deposition in land based gas turbines from various synfuels". *ASME Paper Number GT-2005-68479.*

[4] Schmidt, D. L., Sen, B., and Bogard, D. G., 1996. "Effects of surface roughness on film cooling". *ASME Paper Number 95-GT-299.*

[5] Bunker, R., 2000. "Effect of partial coating blockage on film cooling effectiveness". *ASME Paper Number 2000-GT-244.*

[6] Bons, J. P., Taylor, R., McClain, S. T., and Rivir, R. B., 2001. "The many faces of turbine surface roughness". *Journal of Turbumachinery,* ***123***, pp. 739–748.

[7] Menguturk, M., and Sverdrup, E. F., 1982. "A theory for fine particle deposition in two-dimensional boundary layer flows and application to gas turbines". *Journal of Engineering for Power,* ***104***, pp. 69–76.

[8] Ahluwalia, R. K., Im, K. H., and Wenglarz, R. A., 1989. "Flyash ashesion in simulated coal-fired gas turbine environment". *Journal of Engineering for Gas Turbine and Power,* ***111***, pp. 672–678.

[9] Stringer, J., and Drenker, S., 1981. "Turbine erosion problems and hot gas clean-up requirements for pfb combustion". *Proceedings of American Power Conference,* ***43***, p. 943.

[10] Wammack, J. E., Crosby, J., Fletcher, D., Bons, J. P., and Fletcher, T., 2006. "Evolution of surface deposits on a high pressure turbine blade, part i: Physical characteristics". *ASME Paper Number GT-2006-91246*.

[11] Crosby, J. M., Lewis, S., Bons, J. P., Ai, W., and Fletcher, T., 2007. "Effects of particle size, gas temperature, and metal temperature on high pressure turbine deposition in land based gas turbines from various synfuels". *ASME Paper Number GT2007-27531*.

[12] Ai, W., Murray, N., Fletcher, T., Harding, S., Lewis, S., and Bons, J. P., 2008. "Deposition near film cooling holes on a high pressure turbine vane". *ASME Paper Number GT-2008-50901*.

[13] Hamed, A., Tabakoff, W., and Wenglarz, R., 2006. "Erosion and deposition in turbomachinery". *Journal of Propulsion and Power,* ***22***(2), pp. 350–360.

[14] Shah, A., and Tafti, D., 2007. "Transport of particulates in an internal cooling ribbed duct". *Journal of Turbomachinery,* ***129***(4), pp. 816–825.

[15] Rozati, A., Tafti, D., and Sreedharan, S., 2008. "Effect of snygas ash particle size on deposition and erosion of a film cooled leading edge". *ASME Paper Number HT2008-56155*.

[16] Germano, M., Piomelli, U., Moin, P., and Cabot, W. H., 1991. "A dynamic subgrid-scale eddy viscosity model". *Physics of Fluids A,* ***3***, pp. 1760–1765.

[17] Moin, P., Squires, K., and Cabot, W. H., 1991. "A dynamic subgrid model for compressible turbulence and scalar transport". *Physics of Fluids A,* ***3***, pp. 2746–2757.

[18] Shah, A., 2005. "Development and application of a dispersed two-phase flow capability in a general multi-block navier stokes solver". Master's thesis, Virginia Tech.

[19] Klienstreuer, C., 2003. *Two phase flow: Theory and applications*. Taylor and Francis.

[20] Tafti, D., 2001. "Genidlest- a scalable parallel computational tool for simulating complex turbulent flows". *Proceedings of ASME Fluids Engg. Division,* ***256***.

[21] Chong, M. S., Perry, A. E., and Cantwell, B. J., 1990. "A general classification of three dimensional flow fields". *Physics of Fluids A,* ***2***(5), pp. 765–777.

4. COMPOSITION DEPENDENT MODEL FOR THE PREDICTION OF SYNGAS ASH DEPOSITION IN TURBINE GAS HOTPATH

Abstract

An improved physical model to predict flyash deposition is developed and discussed in this chapter. This model differs from its predecessor [1, 2] by accounting for deposition of syngas ash particles below the ash softening temperature. The modified deposition model is based on the critical viscosity approach. To test this model, deposition of ash particles impacted on a flat, 45° wedge shape geometry is computed and the results obtained from the numerical model are compared to Crosby et al. [3]. Large Eddy Simulation (LES) is used to model the flow field and flyash particles are modeled using a discrete Lagrangian framework. Results quantify deposition for 4 micron particles of various ash composition samples. Most of the deposition occurs at the stagnation region of the target plate. At 1456 K, out of all the ash samples considered in this study, WY and ND ash sample show the highest capture efficiency (15%) and KL1 ash sample exhibits the lowest capture efficiency (0.02%). In general, capture efficiencies for all ash samples followed an exponential trend with temperature. Additionally, this model is also compared to results obtained from the flat plate deposition experiments conducted here at Virginia Tech using PVC particles [4]. In the case of PVC particles, the sticking probability in the deposition model assumed an exponential increase in deposition rate with temperature and was calibrated with one experimental data point. The results obtained from this model for PVC particles showed excellent agreement with the experimental measurements over a range of temperatures.

A part of this work is submitted to the International Journal of Heat and Fluid Flow

4.1 Introduction

The vision of DOE's fossil energy turbine program is to provide power generation technology essential to the success of advanced fossil energy power systems based on Integrated Gasification Combine Cycle (IGCC) before 2015 time frame [5]. One of the key capabilities needed to achieve this goal is the use of Syngas from coal gasification. One of the issues in achieving this goal relates to the durability of turbine components subjected to a harsh high temperature, high pressure, and high velocity environment in the gas path immediately downstream of the combustor. Despite advances in gas cleanup procedures, Syngas produced from coal gasification contains traces of flyash particles whose diameters range from 1 μm to 10 μm [6–8]. The components most likely to experience deposition and erosion and corrosion (DEC) are the first stage nozzle guide vane, the hub and tip regions. One of the region's most susceptible to DEC is the leading edge region of the vane. Deposition and erosion increases the surface roughness of the vane, causing the heat transfer coefficient to increase [9]. In extreme cases, deposition can also lead to blockage of the coolant flow. Kawagishi et al. [10] reported a decrease in stage efficiency by 20% due to deposition. To accurately predict the extent of damage to the turbine vane, it is important to identify and understand the underlying physical processes that lead to deposition.

Experiments have shown that ash deposition is sensitive to turbine inlet gas temperatures [8, 11, 12] which can be in the range of 1600-1900K. The softening temperature (ST) for most of the coal flyash composition is found to be in a range of 1450K - 1500K [11, 13]. This implies that the flyash particles exiting the combustor are molten and sticky. These hot molten particles are transported to the vane surface and interact with the cooling jets. The particle's residence time together with its thermal inertia decides the physical state of the particle when it comes into contact with the vane surface. Our previous studies [1, 2] modeled the physical state of the particle by defining a particle softening temperature , which acts as an on-off switch for particle deposition. If the particle temperature is above the softening tempera-

ture, it is assumed to stick to the surface or otherwise rebound back into the flow. However in reality, the ash particle deposition is not a discontinuous function of a single softening temperature. At ST, ash is making a transition from an initial deformation temperature to fluidity. At this temperature the ash particles are said to be in plastic state and show a tendency to stick to the vane surface. To predict the amount of deposition better, this chapter discusses an improved model to its predecessor by accounting for ash composition and estimating deposition at temperatures below the ash softening temperature.

Bons and co-workers have conducted considerable amount of research to identify factors influencing flyash particle deposition in gas turbine (GT) applications. Jensen et al. [14] describe the Turbine Acceleration Deposition Facility (TADF) used to study the deposition of ash particles on the first stage turbine blades in land based turbines. Following the validation of TADF, Bons et al. [8] presented a comparative analysis of various alternative fuels like straw ash, sawdust ash, coal and petcoke at actual engine conditions. The particles injected had a mass mean diameter of 10 μm. They observed penetration of particles into the cracks of the thermal barrier coating (TBC), consequently hampering the performance of the blade material system. Wammack et al. [15] investigated the physical characteristics of the evolution of surface deposition on a turbine blade. Their experiments concluded the following: first, the deposit roughness height and shape experience a temporary lull in growth during the deposit evolution. Second, the initial surface roughness has a significant effect on deposit growth. Third, thermal cycling combined with particle deposition caused extensive TBC spallation while thermal cycling alone caused none. Hence the deposit penetration into the TBC was a significant contributor to spallation. Crosby et al. [3] then characterized the effect of particle size, gas temperature and cooling of the blade sample from the backside on deposition from coal derived fuels. All the effects were studied independently. The conclusions from their study are as follows. First, deposition increased by a factor of 2 as the mass mean diameter of the particle was increased from 3 μm to 16 μm. Second, particle deposition decreased with decreasing

gas temperature. The threshold gas temperature at which ash particle deposition initiates was found to be 960^{o}C. Furthermore, they concluded that the TBC damage was reduced as the cooling levels were increased.

Among all the studies carried out on ash DE, it was found that ash particle size distribution and their physical properties were among the factors that influenced DE [6]. The level of molten species contained in flyash particles is a function of its chemical composition. Wenglarz [6] observed the sticking fraction of ash particles to be primarily dependent on the surface temperatures. They define the sticking fraction as the mass fraction of particles deposited to the mass of particles injected. In order to reduce molten deposits, he recommends high rates of wall surface cooling. Ahluwalia et al. [16] investigated flyash particle (15 μm and 40 μm) deposition on a wedge shaped (10° , 30° and 45°) target model, representative of a real gas turbine engine condition. They found the sticking coefficient to be 0.04 to 0.11 at gas temperatures of 1325K. Deposition rates were found to increase in a non-linear manner with an increase in wall surface temperature. They also reported that the deposition of the flyash particles was significantly more sensitive to the surface temperature than to other factors such as the impact angle. Another study by Wenglarz and Fox [11, 17] also confirmed the above observation. The above studies show that the physical state of ash particles is a decisive factor in the accurate prediction of deposition.

Walsh et al. [18] used particle viscosity as a means to measure the physical state of the particle to account for observed influences of various ash composition and temperature on deposition. They assumed that the sticking probability is inversely proportional to the viscosity of ash. Along similar lines, Huang et al. [19] also used the viscosity approach to predict the deposition of flyash particles. The model calculates the particle viscosity based on chemical composition and the temperature of the flyash particles. An empirical value of reference viscosity for a given ash sample is chosen, which then governs deposition of the flyash particles. If the ash particle viscosity is less than the reference viscosity then they are assumed to deposit upon impact. The deposition results showed good agreement with experiments for a class

of fouling coal ash samples. An alternative to this approach is to use melt fractions. Ash particles are assumed to deposit when they acquire a minimum percentage of melt fraction (anywhere from 15% to 30%). Consequently, particle temperatures are computed for a range of melt fractions that form sticky particles. Zhou et al. [20] investigated deposition of hot molten flyash particles (0.27 μm, 8 μm and 58 μm) on a circular cooled probe. Their numerical deposition model, similar to Hansen et al. [21] and Kær [22], assumed particles to stick when the melt fraction was in the range of 10% to 70%. The particles above 70% were assumed to form molten slag.

Mueller et al. [23] and Strandstörm et al. [24] validated their melt fraction based deposition model with experiments. The experiment injected molten salts (1373K) representative of ash properties on a cooled probe (803K). They assumed a melt fraction of 15% to 70% to characterize particle sticking. For particle sizes less than 75 μm, their deposition results showed excellent agreement with the experiments. However, the results over estimated the rates of deposition for particles that were greater than 75 μm in size. In order to account for this discrepancy, they combined a rebound model to the melt fraction deposition criteria. This model solved for conservation of mass and energy around the impacting particles greater than 75 μm in size. Depending on the value of the excess energy, the particles could stick or rebound. An extensive review including experimental and analytical studies on this mechanism of deposition is conducted by Hamed et al. [12]. For cases where the gas temperatures are lower than the ash softening temperature El Batsh [25] uses impact/capture velocity as a criterion for deposition. This model requires the elastic properties of the particles and surface materials. Higher values of Young's modulus decrease the capture velocity and results in reduced sticking probabilities. This model does not account for the stickiness of molten particles (capillary forces), which are often an order of magnitude higher than other surface forces such as van der Walls attractive forces. Ai and Fletcher [**?**] have used El-Batsh's deposition model to estimate deposition of 13.4 μm ash particles on a 45° inclined flat plate with film cooling. However, in a separate study, to account for temperature changes in the

deposition model, they developed a correlation of Young's modulus as a function of temperature by calibrating their deposition simulations with experiments. This semi-empiricism in the deposition model gave good agreement with experimental results. Results showed the capture efficiency to increase with increasing blowing ratio.

In summary, both approaches, the viscosity approach and melt fraction approach give similar results for the temperatures at which sticking occurs [22]. The viscosity approach is based on the fact that at impact, lower the viscosity higher is the extent of particle deformation, which in turn increases the tendency of particle sticking. This work uses the viscosity approach to estimate rate of deposition and the results for ash particles are validated with experiments conducted by Crosby et al. [3].

4.2 Objective

The objective of this study is to validate a newly developed deposition model based on sticking probability. The study is novel in that it integrates different sources of published experimental data to form a holistic numerical model to predict ash deposition. The deposition model computes the sticking probabilities as a function of particle temperature and ash composition. In order to validate this model, numerical simulations of ash deposition were conducted on a flat plate inclined at 45° to an impinging ash laden jet. The ash deposition results obtained were validated with experiments by Crosby et al. [3]. This model was also extended to calibrate deposition results from experiments which used PVC particles representative of coal ash to simulate deposition on a flat plate [4]. This model facilitates future studies on the dynamics of ash deposition and erosion in a leading edge vane geometry with film cooling.

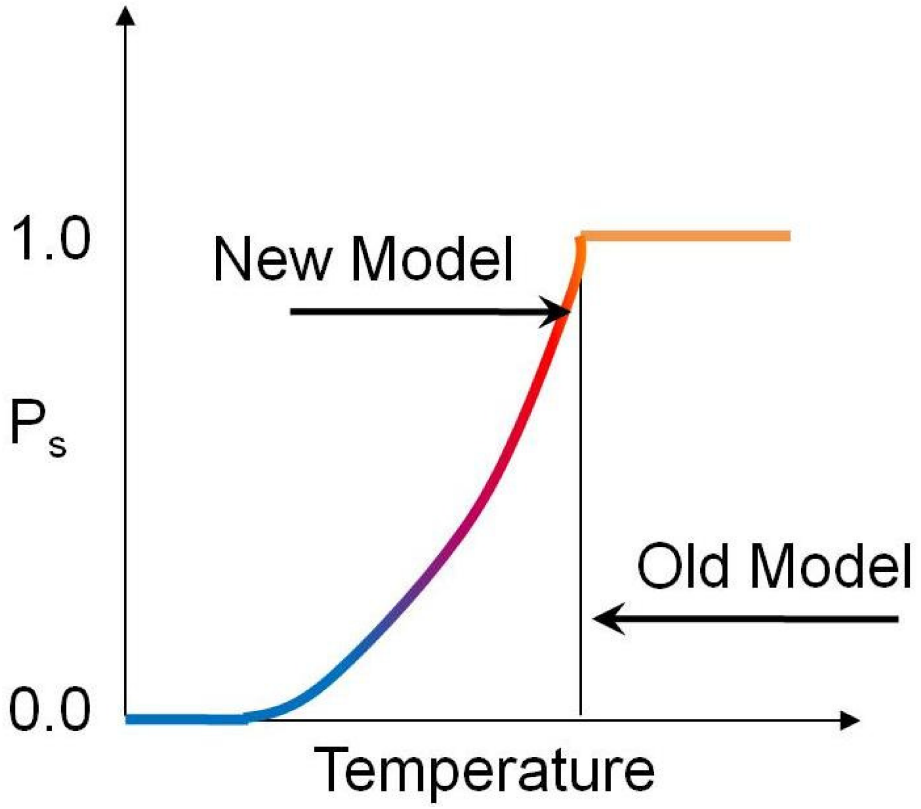

Figure 4.1.: Transition to modified deposition model using critical viscosity approach (P_s - sticking probability, T_s - ash softening temperature.)

4.3 Methodology

4.3.1 Deposition model

In our previous studies (Chapter 3) [2], the effect of jet blowing ratio and particle size or particle Stokes number on deposition and erosion was investigated. Results were presented for two particle diameters of 5 and 7 microns with four coolant-to-mainstream blowing ratios of 0.5, 1.0, 1.5 and 2.0. In this study, the deposition model (Figure 4.1) was implemented as a step function, changing the sticking probability from 0 to 1 at the ST. In order to account for flyash deposition below the ST, a more physical deposition model is developed and discussed in this chapter.

4.3.2 Calculating the sticking probability of ash

The previous deposition model was unable to predict deposition below the softening temperature. The modified deposition model incorporates deposition based on the concept of sticking probability. The sticking probability is computed based on the critical viscosity approach. Critical viscosity is defined at a temperature above which the viscosity rapidly decreases. In terms of sticking probability, viscosity at or below the critical viscosity is assumed to have a sticking probability of unity and at all other particle temperatures it is calculated based on the following equation: (Eq. 4.1):

$$P_s(T_p) = \frac{\mu_{crit}}{\mu_{T_p}} \tag{4.1}$$

where μ_{T_P} is the viscosity at the particle temperature. Ash is composed of multiple inorganic compounds, which vary substantially with the type of coal used for gasification, and a model by Senior and Srinivasachar [26] is used to compute ash viscosity as a function of temperature. The model categorizes ash into constituents that increase the viscosity, constituents that decrease the viscosity, and some constituents which do both. Viscosity is calculated based on the following equation (Eq. 4.2):

$$\log\left(\frac{\mu}{T_p}\right) = A + \frac{10^3 B}{T_p} \tag{4.2}$$

The terms A and B in the above equation vary based on ash composition. The parameter describing this compositional dependence in terms A and B is referred to by the acronym NBO/T which stands for non-bridging oxygen to tetrahedral oxygen.

$$\frac{NBO}{T} = \left\{ \frac{\mathrm{CaO} + \mathrm{MgO} + \mathrm{FeO} + \mathrm{Na_2O} + \mathrm{K_2O} - \mathrm{Al_2O_3} - \mathrm{FeO_3}}{((\mathrm{SiO_2} + \mathrm{TiO_2})/2) + \mathrm{Al_2O_3} + \mathrm{Fe_2O_3}} \right\} \tag{4.3}$$

The constituents CaO, MgO, FeO etc. are mole fractions of oxides present in ash. Hence, viscosity of coal ash is computed using the following procedure:

1. Determine mole fractions of all oxides.

2. Determine NBO/T (Eq. 4.3).

3. Compute the constants A* and B [26].

$$A_H = -3.81629 - 0.46341 \times B - 0.35342 \times \frac{NBO}{T}$$

$$A_L = \begin{cases} -1.982 - 0.902473 \times B & , 1.3 \leq NBO/T \\ 1.478718 - 0.902473 \times B - 2.662091 \times NBO/T & , 0.2 \leq NBO/T < 1.3 \\ 8.223 - 0.902473 \times B - 36.3835 \times NBO/T & , 0.0 \leq NBO/T < 0.2 \\ 8.223 - 0.902473 \times B - 0.35342 & , NBO/T < 0.0 \end{cases}$$

$$B = b_0 + b_1\alpha + b_2\alpha^2 + N(b_3 + b_4\alpha + b_5\alpha^2) + N^2(b_6 + b_7\alpha + b_8\alpha^2) + N^3(b_9 + b_10\alpha + b_11\alpha^2)$$

where:

$$\alpha = \frac{\text{CaO}}{(\text{CaO} + \text{Al}_2\text{O}_3)}$$

and co-efficient's of B are as follows:

	High Temp.	Low Temp.		High Temp.	Low Temp.
b_0	-224.98	-7563.46	b_6	-957.94	-46484.8
b_1	636.67	24431.69	b_7	3366.61	146008.4
b_2	-418.7	-17685.4	b_8	-2551.71	-104306.0
b_3	823.89	32644.26	b_9	387.32	21904.63
b_4	-2398.32	-103681.0	b_{10}	-1722.24	-98194.8
b_5	1650.56	74541.33	b_{11}	1432.08	48429.31

$$A = max(A_H, A_L) \text{ and } B = max(B_H, B_L)$$

*The value of A are corrected values pointed out by Vargas [27]

4. Compute viscosity as a function of temperature.

The paper by Senior and Srinivasachar [26] gives further details on the viscosity model. The model is valid for predicted viscosities up to 10^9 Pa-s. In this study we have implemented an empirical relation to compute the ash softening temperature as a function of ash composition [28]. The empirical formula used for computing ash softening temperature offers a rough estimate of the ash softening temperature. Hence this formula is used only for ash samples whose softening temperature is unknown. Most of the ash samples investigated in this study have the criteria where the content of SiO_2 is no greater than 60% (by wt.), the content of Al_2O_3 is no greater than 60% (by wt.) and the content of Fe_2O_3 is no greater than 15% (by wt.). Then the ash softening temperature, satisfying the above mentioned criteria, is calculated using the regression formula as:

$$\begin{aligned} T_{soft} &= 92.55 \cdot SiO_2 + 97.83 \cdot Al_2O_3 + 84.52 \cdot Fe_2O_3 \\ &\quad +83.67 \cdot CaO + 81.04 \cdot MgO + 91.92 \cdot a - 7891 \end{aligned} \tag{4.4}$$

where: $a = (100 - (SiO_2 + Al_2O_3 + Fe_2O_3 + CaO + MgO))$

Table 4.1 lists some representative ash samples used in the present study. The ExBC ash sample is the ash sample which has the same constituents as that used in the experiments [3]. Figure 4.2 shows the temperature - viscosity variations of the ash samples shown in Table 4.1. Symbols in the figure represent critical viscosities at the calculated softening temperatures.

4.3.3 Implementation of deposition model

For each ash composition, the critical viscosity of ash is computed at the softening temperature (Eq. 4.2). Each time a particle impacts the surface at a temperature lower than the ST, its viscosity is calculated (Eq. 4.2). Then equation

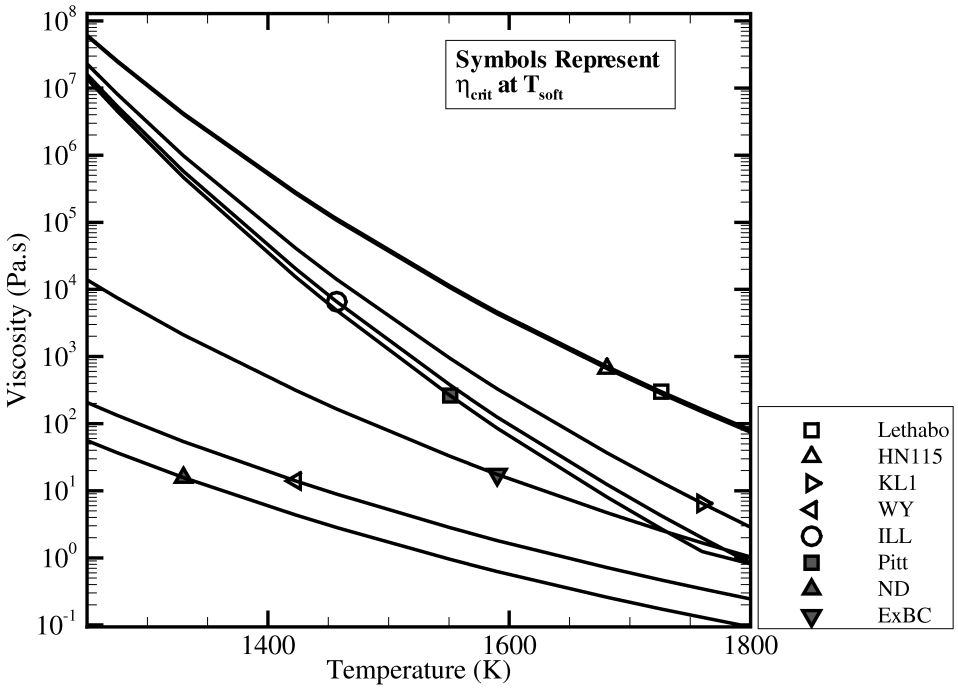

Figure 4.2.: Temperature - viscosity variation for various ash samples.

(Eq. 4.1) is used to calculate the actual sticking probability. In order to implement this formulation, a uniform random number generator is used to generate random sticking probabilities for each particle impact. If the random sticking probability of the particle is less than the actual sticking probability then the particle is assumed to deposit. Any particle that impacts the surface at a temperature higher than the ST is deposited. In order to use this approach, the particle sample size should be large enough for the capture efficiency to asymptote to the actual sticking probability.

4.3.4 Description of geometry

A flat, 45° wedge shape geometry, similar to the experiments conducted by Crosby et al. [3] is used to test the modified deposition model. An ash particle laden jet impinges on the flat plate. The computational domain is as shown in Figure 4.3. All the dimensions are based on the characteristic length ($L_c = 0.0254m$). The inlet tube has a square cross-section of side length $0.89L_c$ and is $8.5L_c$ long. The target

Table 4.1: Chemical composition of some coal ash samples (%wt.)([29–31])

	Lethabo	HN115	KL1	WY	ILL	Pitt	ND	ExBC [3]
SiO_2	60.33	42.3	47.1	35.59	46.62	50.37	23.68	55.44
Al_2O_3	29.73	34.5	35.3	15.15	14.41	21.04	7.94	18.39
Fe_2O_3	2.68	6.17	4.72	7.53	26.80	21.23	9.82	5.00
TiO_2	1.37	2.24	1.9	1.40	0.73	1.14	0.47	1.46
P_2O_5	0.41	0.55	0.19	3.02	1.00	0.90	3.85	2.00
CaO	3.58	8.55	5.67	18.92	2.74	1.37	18.43	6.66
MgO	1.19	1.00	0.75	4.76	0.72	0.65	7.44	3.26
Na_2O	0.14	0.21	0.26	2.10	0.88	0.53	10.20	5.09
K_2O	0.45	0.76	1.33	1.01	3.15	2.00	1.35	1.71
S	0.10	0.04	0.03	10.53	2.94	0.78	16.82	0.98
MnO	0.02	0.00	0.00	0.00	0.00	0.00	0.00	0.00
$T_{soft}K$	1726	1633	1773	1423	1457	1551	1330	1551

specimen is also a square plate with a side length of $0.63L_c$, inclined at 45° with a flat after-body (shaded - dark grey). The target specimen is in-line with the square tube. The gap between the tube exit and the target section is $1.5L_c$. The computational domain extends $25L_c$ in streamwise X-direction, $10L_c$ in Y-direction and $10L_c$ in the Z-direction.

4.3.5 Computational grid

An LES grid is constructed using a multi-block topology. The baseline grid has a size of 17.84 million cells. Figure 4.4 shows the spacing of the grid points in the wall normal direction.

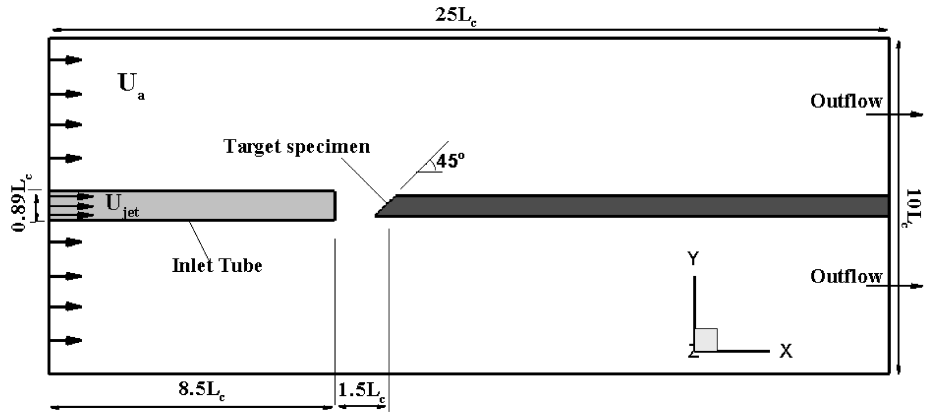

(a) Side View

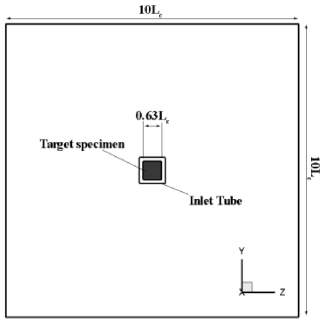

(b) Front View

Figure 4.3.: Computational Domain.

4.3.6 Boundary conditions

The model is tested in a representative geometry in which an ash laden jet impinges on a target plate as shown in Figure 4.3. The basic geometrical configuration and flow conditions are similar to the experiments of Crosby et al. [3]. The target plate used in this study is a square shape as opposed to the experiment which uses a circular shaped plate. This was done to reduce the grid complexity in the present structured multi-block grid framework. This simplification does not alter the bulk

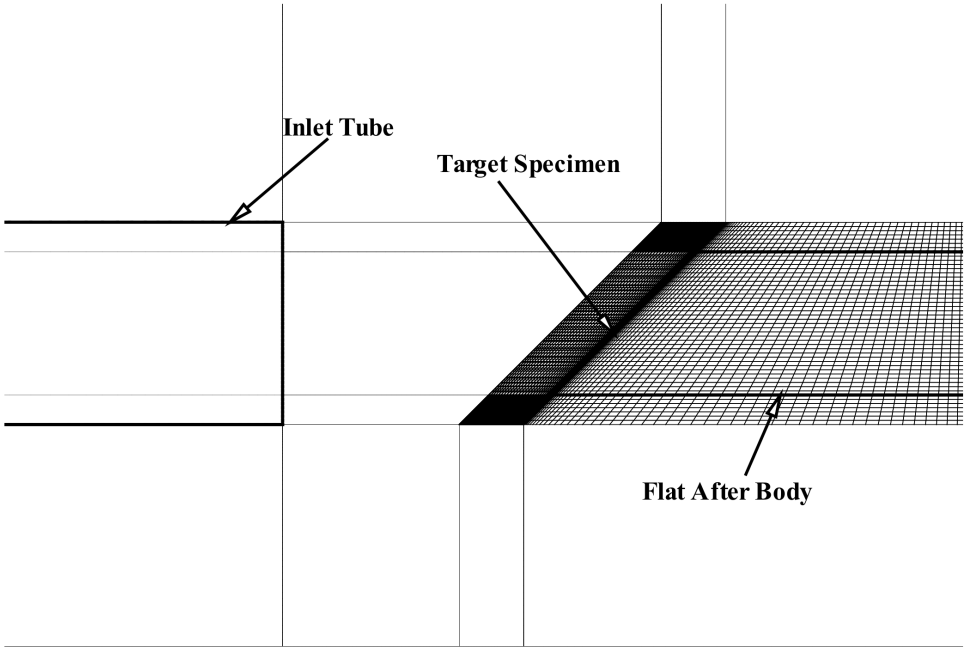

(a) Side View

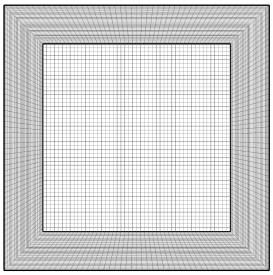

(b) Front View

Figure 4.4.: Mesh near the flat plate.

flow and particulate deposition quantities except possibly near the edges of the target plate. In the present study, the flow Reynolds number is 24,148, based on the mean velocity of the impinging jet and the side length of the target plate . This Reynolds

number (Re_L) is equivalent to the Reynolds number ($Re_D = 21,250$) used in the experiments conducted by Crosby et al. [3] on a circular target plate.

The present computations simulate the adiabatic wall case without backside cooling. Hence all walls are maintained at zero heat flux. The non-dimensional velocity (U_{jet}) in the inlet jet is set to 1 and the velocity (U_a) surrounding the inlet tube is set to 1.0×10^{-10}. The tube inlet condition has a constant velocity profile normal to the boundary. The tube inlet non-dimensional temperature (T_{jet}) is set at 1.0 and the surrounding temperature (T_a) is set to 0. A convective outflow boundary condition is set at the exit.

The flow conditions and the particle properties used to compute the particle Stokes number are tabulated in [Table 4.2]. The similarity in particle dynamics is maintained between the experiments of Crosby et al. [3] and the simulations by the proper choice of Stokes number. The Stokes number signifies the time that a particle takes to respond to a local change in the fluid velocity (momentum Stokes number) or fluid temperature (thermal Stokes number). A Stokes number much less than unity indicates that the particle responds to the changes in the fluid surrounding it almost instantaneously. The momentum Stokes number ranges from 0.12 - 0.16 over the range of jet temperatures simulated, whereas the thermal convective Stokes number remains almost constant at a value of 0.031.

The particles are injected $1.4L_c$ before the exit of the inlet tube. The particle injection plane covers 100% of the projected area of the target specimen. A total number of 25,364 particles are injected at this location. Initially upon particle injection, the particle velocities and temperatures are set the same as the fluid velocity and temperature. Subsequently, the governing equations of motion of these particles are integrated using a third order Adams-Bashforth method in the Lagrangian frame of reference to obtain the velocity, location, and temperature.

Table 4.2: Flow Properties

Length (L_c^*), m	0.0254
Inlet Jet Velocity (U_{jet}^*), m/s	184
Inlet Jet Temperature (T_{jet}^*), K	1300-1500
Ambient Temperature (T_a^*), K	300
Ambient Pressure (P_a^*), atm	1
Particle Density (ρ_p^*), kg/m^3	990
Particle Specific Heat (C_p^*), J/kgK	250
Momentum Stokes Number (St_p)	0.12
Convective Stokes Number (St_{conv})	0.03
Radiative Stokes Number (St_{rad})	5.46

4.3.7 Solution method

The flow and temperature fields are calculated using high-resolution Large-Eddy Simulations (LES). Ash particle dynamics are calculated using a Lagrangian approach in which each individual particle is tracked in the flow field based on a dynamic equation. The governing equations consisting of the incompressible mass, momentum and energy conservation are solved in a generalized body-fitted coordinate system. The equations are non-dimensionalized using a characteristic length scale (L_c), characteristic velocity scale as the jet inlet velocity (U_{jet}), and a characteristic temperature scale ($T_{jet} - T_a$). The non-dimensional time dependent equations are as follows:

Continuity

$$\frac{\partial}{\partial \xi_j}\left(\sqrt{g}\bar{U}^j\right) = 0 \tag{4.5}$$

Momentum

$$\frac{\partial}{\partial t}\left(\sqrt{g}\bar{u}_i\right) + \frac{\partial}{\partial \xi_j}\left(\sqrt{g}\bar{U}^j\bar{u}_i\right) = -\frac{\partial}{\partial \xi_j}\left(\sqrt{g}(\vec{a}^j)_i\bar{p}\right) + \frac{\partial}{\partial \xi_j}\left(\left(\frac{1}{Re} + \frac{1}{Re_t}\right)\sqrt{g}g^{jk}\frac{\partial \bar{u}_i}{\partial \xi_k}\right) \tag{4.6}$$

Energy

$$\frac{\partial}{\partial t}\left(\sqrt{g}\bar{\theta}\right) + \frac{\partial}{\partial \xi_j}\left(\sqrt{g}\bar{U}^j\bar{\theta}\right) = \frac{\partial}{\partial \xi_j}\left(\left(\frac{1}{PrRe} + \frac{1}{Pr_tRe_t}\right)\sqrt{g}g^{jk}\frac{\partial \bar{\theta}}{\partial \xi_k}\right) \tag{4.7}$$

where $\vec{a}^i$ are the contravariant basis vectors [†] , $\sqrt{g}$ is the Jacobian of the transformation, $g^{(ij)}$ is the contravariant metric tensor, $\sqrt{g}U^j = \sqrt{g}(\vec{a}^j)_i u_i$ is the contravariant flux vector, u_i is the Cartesian velocity vector, and θ is the non-dimensional temperature. The overbar in the continuity, momentum and energy equations denote grid filtered quantities. Re_t is the inverse of the non-dimensional turbulent eddy-viscosity and is obtained by the Smagorinsky model.

$$\frac{1}{Re_t} = C_s^2(\sqrt{g})^{(2/3)}|\bar{S}|$$

where $|\bar{S}|$ is the magnitude of the strain rate tensor given by $|\bar{S}| = \sqrt{(2\bar{S}_{ik}\bar{S}_{ik})}$. The Smagorinsky constant C_s^2 is obtained via the dynamic procedure [32] and is constrained to be positive. The turbulent Prandtl number is assumed to have a constant value of 0.5 [33].

The dispersed phase is modeled in the Lagrangian framework. The model currently used has been described in [34]. The model is implemented in an unstructured multiblock, multiprocessor framework and validation in turbulent channel flow has been reported in [35]. The particle sizes investigated in this study are in the range of 4 μm. In this range of particle sizes, among all the forces acting on the particle, drag force dominates the particle motion [7]. Additionally, in practical situations the concentration of flyash particles are very dilute in the mainstream, hence inter

[†]The notation $(\vec{a}^j)_i$ is used to denote the i-th component of vector $\vec{a}^j$, $(\vec{a}^j)_i = \partial\xi_j/\partial x_i$

particle interactions and particle-to-fluid interactions are neglected. The equations for particle motion and temperature in non-dimensional form are as follows:

Motion

$$\frac{du_i^p}{dt} = -\frac{1}{St_p}\left(1 + 0.15Re_p^{0.687}\right)\left(u_i^p - u_i^f\right) \tag{4.8}$$

Location

$$\frac{dx_i^p}{dt} = u_i^p \tag{4.9}$$

Energy

$$\frac{d\theta^p}{dt} = \frac{1}{St_{conv}}\left(\theta^f - \theta^p\right) - \frac{1}{St_{rad}}\left(\theta^p\right) \tag{4.10}$$

where St_p is the particle momentum Stokes number defined as $St_p = \frac{(\rho_p^* d_p^{*2} U_{jet}^*)}{(18\mu L_c^*)}$, St_{conv} is the particle convective thermal Stokes number defined as $St_{conv} = \frac{(\rho_p^* c_p^* d_p^* U_{jet}^*)}{(6hL_c^*)}$, St_{rad} is the particle radiative thermal Stokes number defined as $St_{rad} = \frac{(\rho_p^* c_p^* d_p^* U_{jet}^*)}{(6h_r L_c^*)}$, with the effective radiative heat transfer coefficient defined as $h_r = \epsilon\sigma(T_p + T_a)(T_p^2 + T_a^2)$[‡]. The momentum and convective Stokes numbers are defined assuming low relative particle Reynolds number ($Re_p < 1$), $C_d = 24/Re_p$ and $Nu_p = 2.0$ [36].

To get a quick estimate of ash deposition for various particle sizes, a computationally efficient stochastic Discrete Random Walk (DRW) model is also implemented in the present framework to predict particle trajectories that uses time averaged statistics obtained from LES calculations. This model is also referred as Eddy Interaction Model, where particles interact with eddies in the flow and their motion is computed using a constructed instantaneous velocity field [37]. Initially the particle is placed at the center of the eddy, in which the fluid velocity is assumed to be constant, characterized by its lifetime and length. The motion of the particle in a given eddy can be calculated based on the eddy velocity. The fluctuating part of this eddy velocity is found using a Gaussian distribution with zero mean and a standard deviation of unity. The characteristic scales for the eddy is determined from the turbulent statistics obtained from the flow field and are defined as follows [38]:

[‡]For an estimate of lowest radiative Stokes number ($T_p = T_{jet}$)

$$u'_{rms} = \zeta\sqrt{u'^2}; \quad v'_{rms} = \zeta\sqrt{v'^2}; \quad w'_{rms} = \zeta\sqrt{w'^2} \tag{4.11}$$

$$\tau_e = l_e/|u'_{rms}| \tag{4.12}$$

$$l_e = C_\mu^{0.5} \cdot k^{3/2}/\epsilon \tag{4.13}$$

where ζ - normally distributed random number, τ_e - eddy lifetime, l_e - eddy dissipation length scale.

In order to obtain a meaningful statistical sample from the DRW model, a large number of particles are injected at a given location. In the present case, time-averaged statistics and turbulent statistics are used from the LES calculations. A constant time scale less than the eddy lifetime (τ_e) is chosen for the present study. This will always ensure that the particles are confined within the eddy [37]. The DRW model considers anisotropic turbulence as given in (Eq.4.11) unlike isotropic turbulence that is commonly used with RANS based solver . Deposition results from the DRW model are also compared with deposition obtained from time-accurate LES calculations.

4.3.8 Solver controls

The simulation uses the in - house conservative finite volume code, GenIDLEST [39]. The carrier phase (fluid) is computed using LES and the discrete phase (particles) is solved using the Lagrangian particle tracking algorithm [34]. The discretization of the governing equations (carrier phase) uses a second order central difference scheme on a non-staggered grid topology. The convergence criterion for the momentum, pressure and the energy are 1×10^{-6}, 1×10^{-6} and 1×10^{-6}, respectively at each time step. The time step is set at 2×10^{-4}. The flow is first allowed to develop and averaged for more than 20 non-dimensional time units before the particles are

injected. The particles are tracked and allowed to run until all the particles cross the target plate. In this study, particles trajectories are computed using two approaches. One approach uses time-accurate LES and Discrete Phase Modeling (DPM) and the other approach uses mean statistics from LES and the DRW model. All the results shown here are computed using 171 processors on Virginia Techs high performance terascale supercomputing facility, SYSTEM X.

4.4 Discussion of results

Particles of $4\mu m$ diameter are simulated using the time-accurate LES simulations to study the effects of mainstream temperature and flyash compositions on deposition. Impact efficiency of particle sizes ranging from $2 - 13.4\mu m$ are investigated using the DRW model. In this present study, eight different flyash compositions are selected from the available literature (Table 4.1). First, the flow field features are discussed followed by the deposition results on the flat plate.

4.4.1 Flow and thermal fields

Figure 4.5a shows instantaneous flow streamlines and streamwise (x-direction) velocity contours. The stagnation point is located at the bottom of the flat plate. The jet fluid impacts the stagnation point and then accelerates straight and parallel to the surface of the plate and eventually exits through the outflow. Recirculation zones are found to occur just behind the plate on the flat after body.

One of the predominant features of the flow is the free shear layer mixing between the jet from the pipe and surrounding stationary fluid. Figure 4.5b shows instantaneous temperature contours in the streamwise direction. The mainstream entrainment due to the free shear layer mixing does cool the flat after body downstream of the target plate. However, at this Reynolds number ($Re_L = 24,148$), the target specimen is always at the jet temperature emanating from the pipe. Figure 4.6 shows the mean flow and thermal field in the streamwise direction.

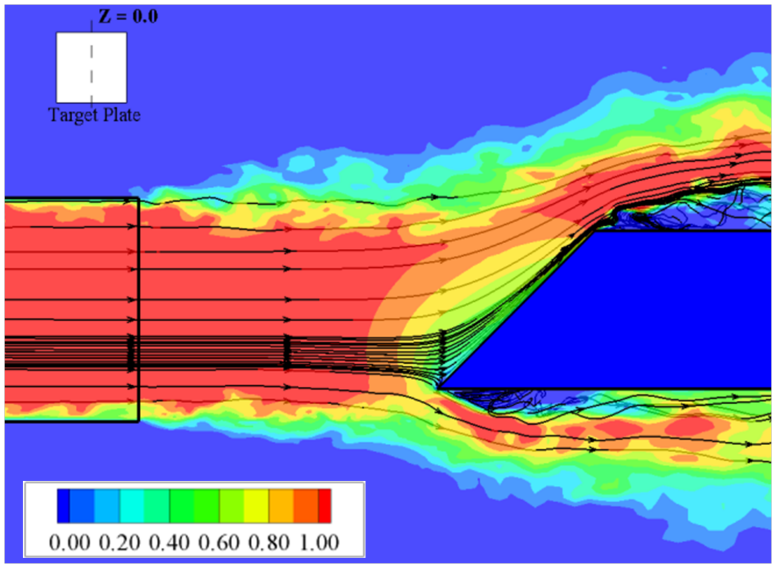

(a) Velocity contours and flow streamlines

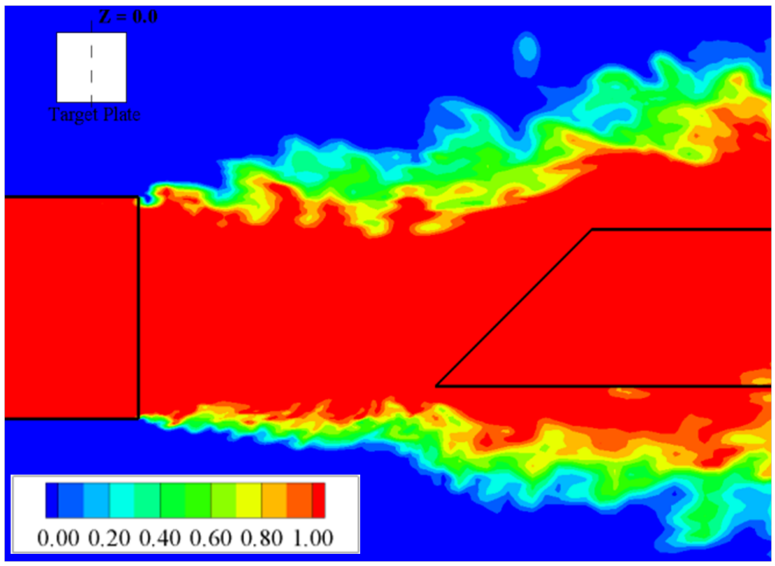

(b) Temperature contours

Figure 4.5.: Instantaneous flow features in X-Y plane (slice location: Z=0.0).

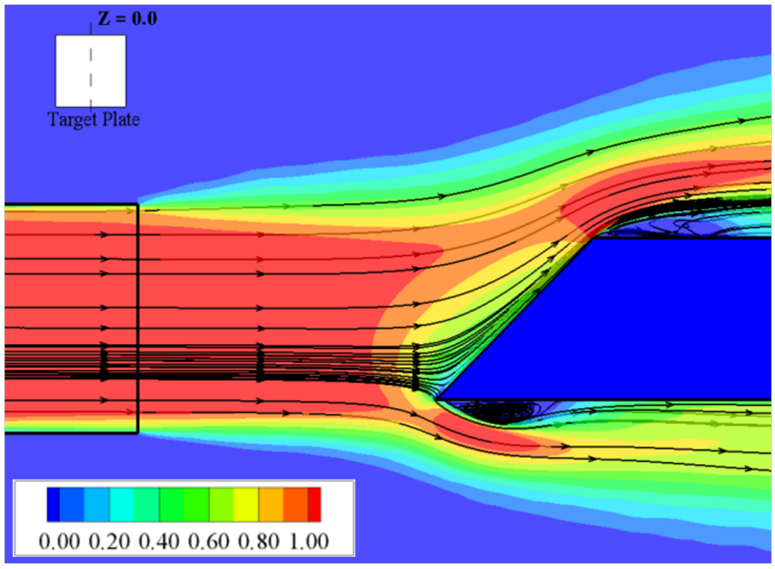

(a) Velocity contours and flow streamlines

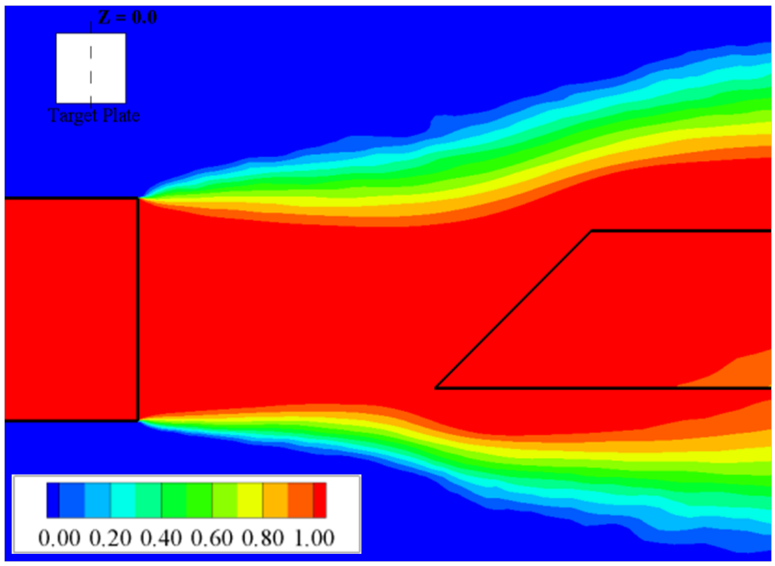

(b) Temperature contours

Figure 4.6.: Mean flow features in X-Y plane (slice location: Z=0.0).

4.4.2 Validation studies

4.4.2.1. Simulated ash experiments

Deposition and capture efficiency on the flat target plate depends on the particle sticking probability based on the particle temperature for a given ash composition.

The only possible way that a particle can cool is when it gets caught in the free shear layer and mixes with the freestream surrounding air. Particles that do not deposit undergo an elastic collision with the flat plate.

First, the particle dynamics obtained from DRW model is compared to time-accurate LES simulations. As mentioned before in §Solution Method (4.3.7) , to give a realistic estimate of deposition, the dispersion of flyash particles caused due to the presence of turbulence is modeled using a stochastic approach (Discrete Random Walk Model). The purpose of using this computationally efficient model is to give a quick estimate of capture efficiency for a range of particle sizes. This model accounts for local variations in the flow field that can potentially alter particle trajectories in an effort to simulate unsteady particle trajectories using the mean flow field. This instantaneous velocity field is obtained as a product of a normalized random number and u_{rms} from the turbulent kinetic energy (Eq. 4.11). Figure 4.7 compares instantaneous ExBC (Table 4.1) ash particle trajectories obtained from the DRW model to time-accurate LES simulations. It is clear that the DRW model under-predicts the turbulence dispersion when compared to LES simulations. The r.m.s. value is zero near the stagnation region (bottom edge) of the flat plate and then it gradually increases to about 0.15 as it exits the flat plate. Hence the turbulence dispersion effects will be in prominence at the top edge of the flat plate in the DRW model.

Impact efficiency is defined as a percentage of particles that hit the surface to the total number of particles injected. Figure 4.8a shows the variation of impact efficiency as a function of particle sizes for ExBC ash sample (Table 4.1) at 1456K. The impact efficiency increases with increasing particle diameter and this is attributed to increasing particle momentum Stokes number ($St_p(2\mu m) = 0.03$ and $St_p(14\mu m) = 1.4$). Figure 4.8b shows a corresponding variation of capture efficiency as a function of particle size at 1456K. Capture efficiency is defined as the percentage of particles that deposit to the total number of particles injected at inlet. Sticking probability of ExBC ash sample at 1456K is computed to be 0.45 (Eq. 4.1 - 4.2). For larger particle sizes resulting in 100% impact efficiency, capture efficiency will be equal to

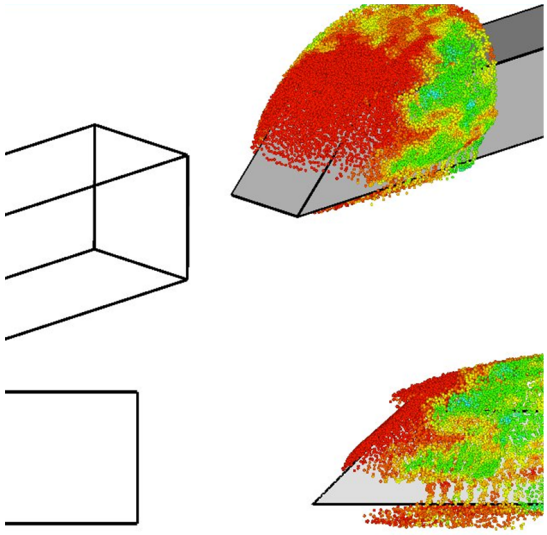

(a) DRW

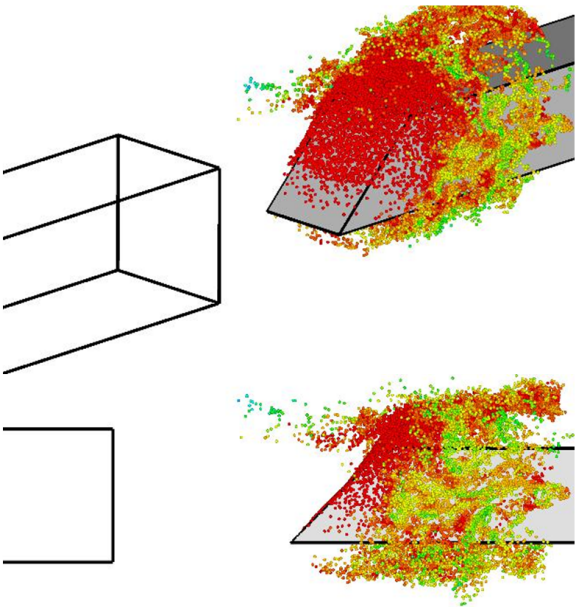

(b) LES

Figure 4.7.: Comparison of turbulence dispersion of particles obtained from DRW to time-accurate LES simulations. (Ash particles are colored with temperature)

the sticking probability for a given temperature and ash composition. Following this, it can be inferred that the capture efficiency increases with particle size and will

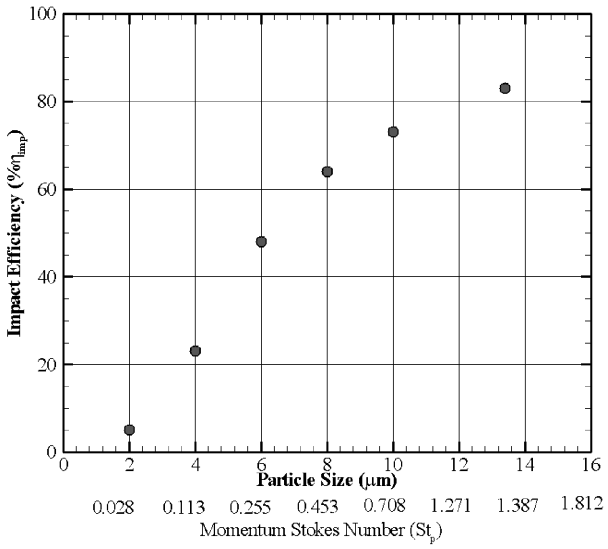

(a) Impact Efficiency

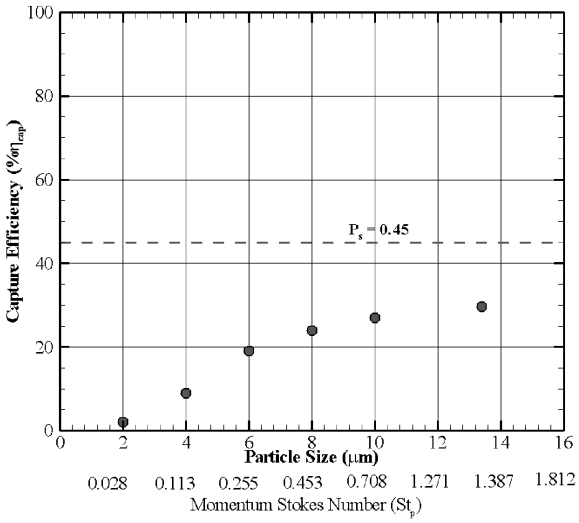

(b) Capture efficiency

Figure 4.8.: Deposition results obtained from DRW model for a range of particle sizes at 1456K.

eventually asymptote to a constant value ($\eta_{cap} \sim 45\%$ for $\eta_{imp} \sim 100\%$) for a given inlet jet temperature (1456K) as shown in figure 4.8b.

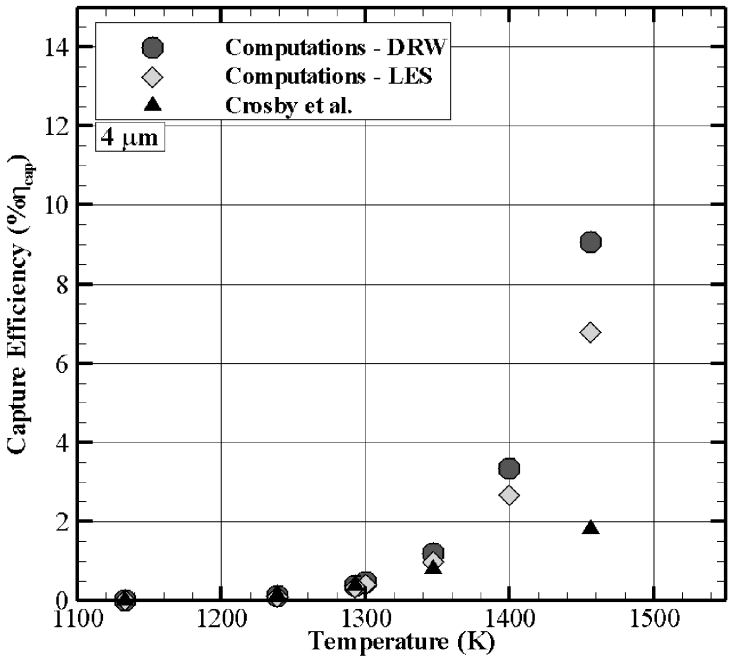

Figure 4.9.: Capture efficiency as a function of temperature, comparisons with experiments for particle size of $4\mu m$. ($T_{soft} = 1551K$).

Figure 4.9 shows quantitative comparisons of capture efficiency obtained from numerical simulations to the experiments of Crosby et al. [3] as a function of jet inlet temperature. The deposition trend matches until 1400K after which the simulated capture efficiency is higher than the experiments. Crosby et al. [3] mention in their paper that the capture efficiency reported at 1456K is lower than that observed by Wenglarz et al. [17]. This low capture efficiency might be due to the flaking of the ash particles that flow away with the mainstream. Other than these differences, the computational model shows the capability of correctly quantifying ash deposition below the softening temperature. Figure 4.9 also shows the comparison of DRW model to time-accurate LES calculations. DRW model tends to over-predict deposition at higher temperatures and this can be attributed to the lesser turbulent dispersion in the DRW model.

Figure 4.10 shows contours for flyash samples that deposit on the flat target plate at the mainstream temperature of 1456K used by Crosby et al. [3]. This figure shows 3 ash samples for which deposition is significantly visible. The particles follow the flow streamlines closely, as they have a low momentum Stokes number. Most of the deposition for all ash samples is seen to occur near the stagnation region. Deposition is also observed at the edges of the flat plate (target specimen). At 1456K, although each ash sample shows a qualitatively similar deposition pattern, the actual number of particles that deposit differ quantitatively. This can be attributed to the differences in ash viscosities at that temperature. The WY and ND ash sample have 3808 particles (15%) that stick followed by ILL ash sample with 3206 particles (12.6%) and KL1 ash sample has the least deposition with 5 particles (0.02%) at 1456K. Ash composition variation for WY and KL1 explains this occurrence, CaO is one of the constituents in WY ash sample which is around 10 times higher than that typically found in other ash samples. Ash samples that are rich in CaO reduce the viscosity of the compound and hence increase deposition [40]. Among other constituents, SiO_2 is 70% and Al_2O_3 is 40% in WY ash sample compared to that in KL11 ash sample [Table 4.1]. The temperature-viscosity variation for the WY and ND ash sample is more gradual whereas the variation for KL1 ash sample is relatively steep.

Figure 4.11 shows the capture efficiency as a function of jet temperature normalized by softening temperature for the different ash samples. All the ash samples follow a similar exponential trend for deposition. The deposition increasess exponentially with increase in temperature reaching a maximum value of 15% at the ST, indicating that only 15% of the incident particles impact the target surface while the rest are redirected with the flow.

4.4.2.2. Simulated PVC experiments

Additional computational studies were carried out to compare experimental deposition results obtained from PVC particles. Details of the experiment conducted using PVC particles can be found in [4]. The experiments consider a setup in which a target coupon is placed in the tunnel subjected to a heated freestream laden with

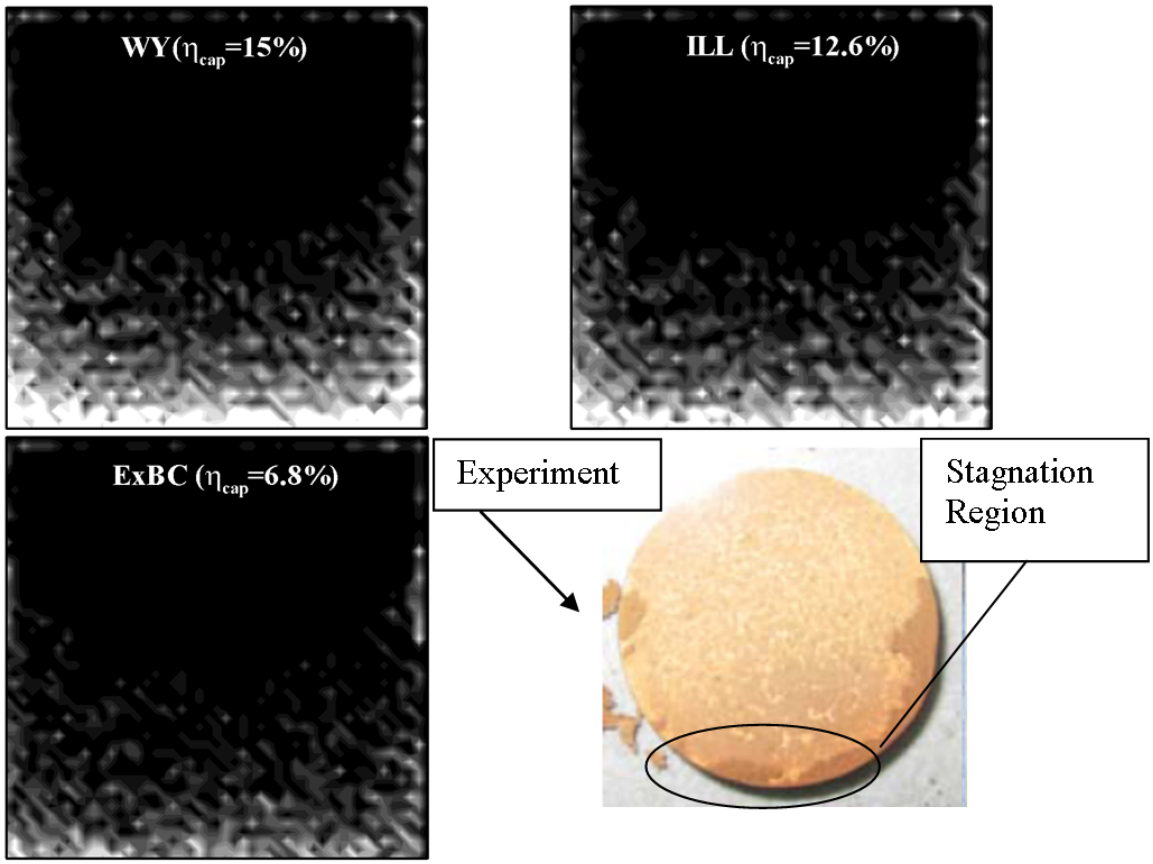

Figure 4.10.: Contours of particle deposition hits on an inclined flat plate at 1456K for different flyash composition. (The direction of the flow is into the paper) compared to experiments [3]. (Softening temperatures for ILL, WY and ExBC are 1457K, 1423K and 1551 K respectively).

PVC particles. Similarity between the computations and experiments is maintained by using flow conditions such that the particle momentum Stokes number in the experiments has a nominal value of 0.12. The temperature in this study is non-dimensionalized based on PVC melting temperature ($T = T^*/T^*_{melt}$).

The sticking probability as used for flyash cannot be used for PVC particles. Instead, as observed in ash, it is assumed that PVC adopts a similar exponential trend of the form $P_s(T_p) = P_s(T_0) \cdot exp(kT_p)$. The sticking probability (P_s) is a function of

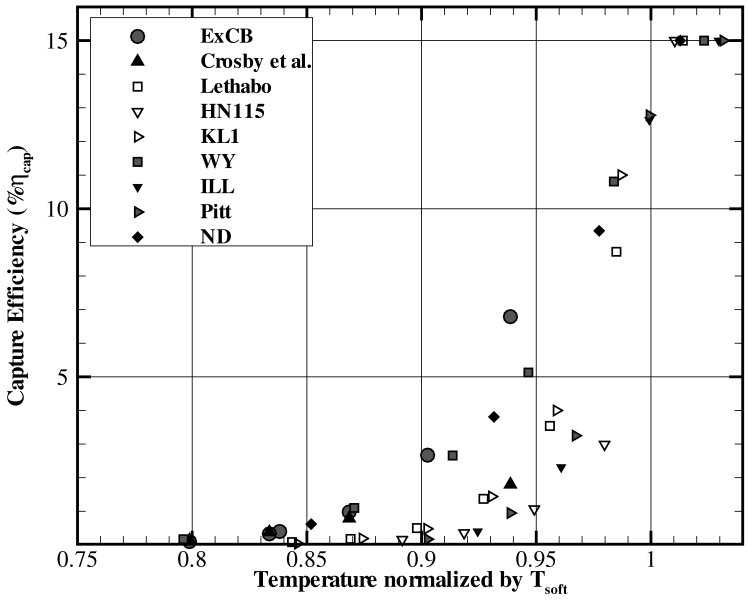

Figure 4.11.: Capture efficiency for different ash sample as a function of mainstream temperature normalized by respective ash softening temperature (Particle size - $4\mu m$).

particle temperature (T_p) impacting the wall. $P_s(T_0)$, sticking probability at 0K, is calibrated to 1.06E-05 by using one experimental data point at T=0.86. Finally, the constant k is computed assuming that PVC melts at $T^*_{melt} = 533K(P_s = 1)$.

Figure 4.12 shows the graph of capture efficiency as a function of non-dimensional temperature for the PVC particles. The numerical capture efficiency shows excellent agreement with the experimental results. The results from the numerical deposition model are tabulated in Table 4.3.

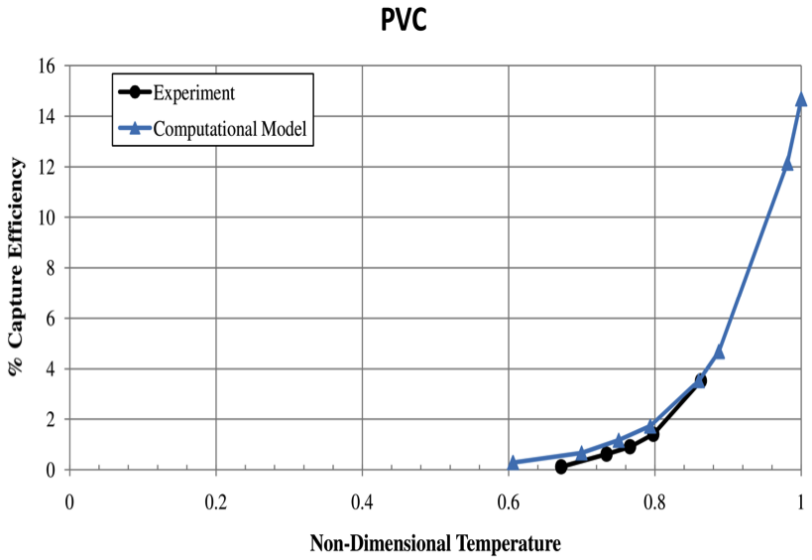

Figure 4.12.: Comparison of capture efficiency of PVC with available experiment [4].

Table 4.3: Capture efficiency on the flat plate without backside cooling

Temp. (K)	$T = T^*/T^*_{melt}$	$\%\eta_{cap}$	P_s
533	1.000	14.630	1.000
523	0.981	11.650	0.772
473	0.887	3.700	0.211
423	0.794	1.110	0.058
400	0.750	0.690	0.032
373	0.700	0.360	0.016
323	0.606	0.140	0.004

4.5 Summary and conclusions

An improved physical model to predict flyash deposition is developed based on the critical viscosity approach. To test this model, deposition of ash particles impacted on a flat, 45° wedge shape geometry is computed and the results obtained from the numerical model are compared to Crosby et al. [3]. Large Eddy Simulation (LES) is used to model the flow field and flyash particles are modeled using two approaches, namely DPM using time-accurate LES solutions and DRW model using the mean statistics obtained from LES calculations. Results quantify capture efficiency for 4 micron particles obtained from the DRW model and DPM and compare them to available experiments. Subsequently, qualitative comparisons are also carried out for various ash samples. It is shown that the model is sensitized to temperature and ash composition and compares well with experiments done with ash. Additionally, this model is also compared to results obtained from the flat plate deposition experiments conducted here at Virginia Tech using PVC particles showing good agreement with the measurements over a range of temperatures. Based on these tests, the modified deposition model will be extended to investigate deposition on the leading edge of a film-cooled turbine vane.

4.6 Bibliography

[1] Rozati, A., Tafti, D., and Sreedharan, S. S., 2010. Effect of syngas ash particle size on deposition and erosion of a film cooled leading edge. In Press.

[2] Sreedharan, S. S., and Tafti, D. K., 2009. "Effect of blowing ratio on syngas fly ash particle deposition on a three-row leading edge film cooling geometry using large eddy simulations". *ASME Paper No. GT2009-59326*.

[3] Crosby, J. M., Lewis, S., Bons, J. P., Weiguo, A., and Fletcher, T., 2007. "Effects of partilce size, gas temperature, and metal temperature on high pressure turbine deposition in land based gas turbines from various synfuels". *ASME Paper No. GT2007-27531*.

[4] Wood, E., Vandsburger, U., Ng, W., and Lapera, S., 2010. "Syngas ash deposition particle substitution method for experimentation". *ASME Paper No. GT2010-22445*.

[5] Dennis, R., 2003. "First international conference on gas turbine technology". *Presentation Report*, July 10-11.

[6] Wenglarz, R. D., 1985. "Deposition, erosion and corrosion protection for coal-fired gas turbine". *ASME Paper No. 85-GT-61*.

[7] Tabakoff, W., 1991. "Measurements of particles rebound characteristics on materials used in gas turbines". *Journal of Propulsion,* **7**(5), pp. 805–813.

[8] Bons, J. P., Crosby, J., Wammack, J. E., Bentley, B. I., and Fletcher, T., 2005. "High pressure turbine deposition in land based gas turbines from various synfuels". *ASME Paper No. GT-2005-68479*.

[9] Bons, J. P., 2002. "St and c_f augmentation for real turbine roughness with elevated freestream turbulence". *Journal of Turbomachinery,* ***124***, pp. 632–644.

[10] Kawagishi, H., Nagao, S., and Kawasaki, S., 1992. "Performance evaluation of geothermal steam turbine with scaled deposits". *PWR, Steam Turbine-Generator Developments for Power generation Industry,* ***18***.

[11] Wenglarz, R. A., and Fox, R. G., 1990. "Chemical aspects of deposition/corrosion from coal-water fuels under gas turbine conditions". *Journal Engineering for Gas Turbines and Power,* ***112***(1), pp. 1–8.

[12] Hamed, A., Tabakoff, W., and Wenglarz, R., 2006. "Erosion and deposition in turbomachinery". *Journal of Propulsion and Power,* ***22***(2), pp. 350–360.

[13] Crosby, J. M., 2007. "Particle size, gas temperature, and impingement cooling effects on high pressure turbine deposition in land based gas turbines from various synfuels". Master's thesis, Brigham Young University.

[14] Jensen, J. W., Squire, S. W., and Bons, J. P., 2005. "Simulated land-based turbine deposits generated in an accelerated deposition facility". *Journal of Turbomachinery,* ***127***, pp. 462–470.

[15] Wammack, J. E., Crosby, J., Fletcher, D., Bons, J. P., and Fletcher, T., 2006. "Evolution of surface deposits on a high pressure turbine blade, part 1: Physical characteristics". *ASME Paper No. GT2006-91246.*

[16] Ahluwalia, R. K., Im, K. H., and Wenglarz, R., 1989. "Fly ash adhesion in simulated coal-fired gas turbine environment". *Journal Engineering for Gas Turbines and Power,* ***111***, pp. 672–678.

[17] Wenglarz, R. A., and Fox, R. G., 1990. "Physical aspects of deposition/corrosion from coal-water fuels under gas turbine conditions". *Journal Engineering for Gas Turbines and Power,* ***112***(1), pp. 9–15.

[18] Walsh, P. M., Sayre, A. N., Loehden, D. O., Monroe, L. S., Beer, J. M., and Sarofim, A. F., 1990. "Deposition of bituminous coal ash on an isolated heat exchanger tube: Effects of coal properties on deposit growth". *Progress in Energy and Combustion Science,* ***16***, pp. 327–334.

[19] Huang, L. Y., Norman, J. S., Pourkashanian, M., and Williams, A., 1996. "Prediction of ash deposition on superheater tubes from pulverized coal combustion". *Journal of Fuel,* ***75***(3), pp. 271–279.

[20] Zhou, H., Jensen, P. A., and Frandsen, F. J., 2007. "Dynamic mechanistic model of superheater deposit growth and shedding in a biomass fired grate boiler". *Fuel,* ***86***, pp. 1519–1533.

[21] Hansen, L. A., Frandsen, F. J., Dam-Johansen, K., and Sorensen, H. S., 1999. "Quantification of fusion from solid fuel combustion". *Thermochimica Acta,* ***326***, pp. 105–117.

[22] Kær, S. K., 2001. "Numerical investigation of ash deposition in straw fired boilers". PhD thesis, Institute of Energy Technology, Denmark.

[23] Mueller, C., Selenius, M., Theis, M., Skrifvars, B. J., Backman, R., Hupa, M., and Tran, H., 2005. "Deposition behaviour of molten alkali-rich fly ashes-development of a submodel for cfd applications". *Proc. Combustion Institute,* ***30***, pp. 2991–2998.

[24] Strandström, K., Mueller, C., and Hupa, M., 2007. "Development of an ash particle deposition model considering build-up and removal mechanism". *Journal Fuel Processing Technology,* ***88***, pp. 1053–1060.

[25] El-Batsh, H., 2001. "Modeling particle deposition on turbine and compressor blade surfaces". PhD thesis, Vienna University of Technology.

[26] Senior, S. L., and Srinivasachar, S., 1995. "Viscosity of ash particles in combustion systems for prediction of particle sticking". *Energy and Fuels,* ***9***, pp. 277–283.

[27] Vargas, S., 2001. Straw and coal ash rheology.

[28] Yin, C., Luo, Z., Ni, M., and Cen, K., 1998. "Predicting coal ash fusion temperature with a back-propagation neural network model". *Fuel,* ***77***(17), pp. 1777–1782.

[29] Ledesma, M., and Isaacs, L. L., 1990. "Thermal properties of coal ash". *Materials Research Society.*

[30] Mbabazi, J. G., Sheer, T. J., and Shandu, R., 2004. "A model to predict erosion on mild steel surfaces impacted by boiler fly ash particles". *Wear,* ***257***, pp. 612–624.

[31] LI, H., Yoshihiko, N., Dong, Z., and Zhang, H., 2006. "Application of the factsage to predict the ash melting behavior in reducing conditions". *Chinese Journal of Chemical Eng.,* ***14***(6), pp. 784–789.

[32] Germano, M., Piomelli, U., Moin, P., and Cabot, W. H., 1991. "A dynamic subgrid-scale eddy viscosity model". *Physics of Fluids,* ***3***, pp. 1760–1765.

[33] Moin, P., Squires, K., and Cabot, W. H., 1991. "A dynamic subgrid model for compressible turbulence and scalar transport". *Physics of Fluids,* ***3***, pp. 2746–2757.

[34] Shah, A., 2005. "Development and application of a dispersed two-phase flow capability in a general multi-block navier stokes solver". Master's thesis, Virginia Tech.

[35] Shah, A., and Tafti, D. K., 2007. "Transport of particulates in an internal cooling ribbed duct". *Journal of Turbomachinery,* ***129***(4), pp. 816–825.

[36] Klienststreuer, C., 2003. *Two phase fow: Theory and applications.* Taylor and Francis.

[37] Graham, D. I., and James, P. W., 1995. "Turbulent dispersion of particles using eddy interaction models". *Int. Journal of Multiphase Flow,* ***22***(1), pp. 157–175.

[38] Gosman, A. D., and Ioannides, E., 1983. "Aspects of computer simulation of liquid-fueled combustors". *Journal of Energy,* ***7***(6), pp. 482–490.

[39] Tafti, D. K., 2001. "Genidlest - a scalable parallel computational tool for simulating complex turbulent flows". *Proceedings of the ASME Fluids Engineering Division,* ***256***, pp. 347–356.

[40] Rushdia, A., Guptaa, R., Sharmaa, A., and Holcombe, D., 2005. "Mechanistic prediction of ash deposition in a pilot-scale test facility". *Fuel,* ***84***, pp. 1246–1258.

5. EFFECT OF BLOWING RATIO ON DEPOSITION OF A VARIETY OF SYNGAS ASH SAMPLES ON A THREE-ROW FILM-COOLED LEADING EDGE VANE GEOMETRY USING LARGE EDDY SIMULATIONS

In Chapter 3, the effect of blowing ratio on Syngas ash deposition on a three-row film cooled leading edge vane geometry was presented. The deposition model was a step function based on the softening temperature, preventing any ash deposition below the softening temperature. Chapter 4 developed and validated a new deposition model which allowed for the deposition of ash below the softening temperature as observed by experiments. In this chapter, the three row film-cooled leading edge geometry (Chapter 3) is revisited with the new deposition model. The chapter discusses the effect of blowing ratio on the Syngas ash deposition on the leading edge vane geometry using the composition dependent ash deposition model. Results are presented for two particle diameters of 5 and 10 microns with the coolant to mainstream blowing ratios of 0.5, 1.0, 1.5 and 2.0 using time-accurate LES calculations. Deposition results are also estimated using the discrete random walk (DRW) model and are compared to that obtained from LES calculations. Eight different ash compositions given in Table 5.1 are used in the present study. The leading edge cooling geometry and the computational model description is described in section §3.3 and is not repeated here. The deposition model is described in section §4.3.

5.1 Discussion of results

The flow and temperature fields generated by the coolant jet-mainstream interaction are crucial to the aero-thermal behavior of particles and have a first-order effect on surface deposition. The aerodynamics of jet-mainstream interaction can either push the particles away from the vane surface or entrain the particle near the

Table 5.1: Chemical composition of some coal ash samples (%wt.)(§4.3)

	Lethabo	HN115	KL1	WY	ILL	Pitt	ND	ExBC
SiO_2	60.33	42.3	47.1	35.59	46.62	50.37	23.68	55.44
Al_2O_3	29.73	34.5	35.3	15.15	14.41	21.04	7.94	18.39
Fe_2O_3	2.68	6.17	4.72	7.53	26.80	21.23	9.82	5.00
TiO_2	1.37	2.24	1.9	1.40	0.73	1.14	0.47	1.46
P_2O_5	0.41	0.55	0.19	3.02	1.00	0.90	3.85	2.00
CaO	3.58	8.55	5.67	18.92	2.74	1.37	18.43	6.66
MgO	1.19	1.00	0.75	4.76	0.72	0.65	7.44	3.26
Na_2O	0.14	0.21	0.26	2.10	0.88	0.53	10.20	5.09
K_2O	0.45	0.76	1.33	1.01	3.15	2.00	1.35	1.71
S	0.10	0.04	0.03	10.53	2.94	0.78	16.82	0.98
MnO	0.02	0.00	0.00	0.00	0.00	0.00	0.00	0.00
$T_{soft}K$	1726	1633	1773	1423	1457	1551	1330	1551

surface. Similarly, the thermal field generated by the jet-mainstream interaction influences the temperature of the particle. The momentum Stokes number governs the particle trajectory, whereas the thermal Stokes number dictates the response time for the particles to the changes in temperature within the flow field. The flow conditions and the particle properties used to compute the Stokes number are tabulated in Table 5.2. The turbulent mixing in the coolant jet-mainstream interface alters the particle trajectory and temperature. First, the flow features on the film-cooled leading edge vane geometry are discussed followed by deposition results.

Table 5.2: Leading edge geometry and flow properties

Leading Edge Geometry	
Blade leading edge diameter (D^*) $[m]$	0.01
Coolant jet diameter (d^*) $[m]$	4.65×10^{-4}
Span-wise pitch (p^*/d^*)	4.5
Flow Properties	
Free stream velocity (U^*_∞), $[m/s]$	40
Free stream temperature (T^*_∞), $[K]$	1600
Free stream pressure (P^*_∞), $[atm]$	20
Free stream density (ρ^*_∞), $[kg/m^3]$	4.4
Particle density (ρ^*_p), $[kg/m^3]$	2500
Particle Specific heat (c^*_p), $[J/kgK]$	250
Coolant temperature (T^*_j), $[K]$	775
Coolant-to-mainstream density ratio	2.071
Coolant-to-mainstream blowing ratio (U^*_j/U^*_∞)	0.5, 1.0, 1.5, 2.0

Table 5.3: Particle Stokes number

d^*_p (μm)	St_p	St_{conv}	St_{rad}
5	0.25	0.0578	2.24
10	1.01	0.215	4.49

5.1.1 Flow and thermal field

To get an insight into the coolant jet-mainstream mixing, instantaneous coherent turbulent structures are plotted. Figure 5.1 shows the iso-surfaces of coherent

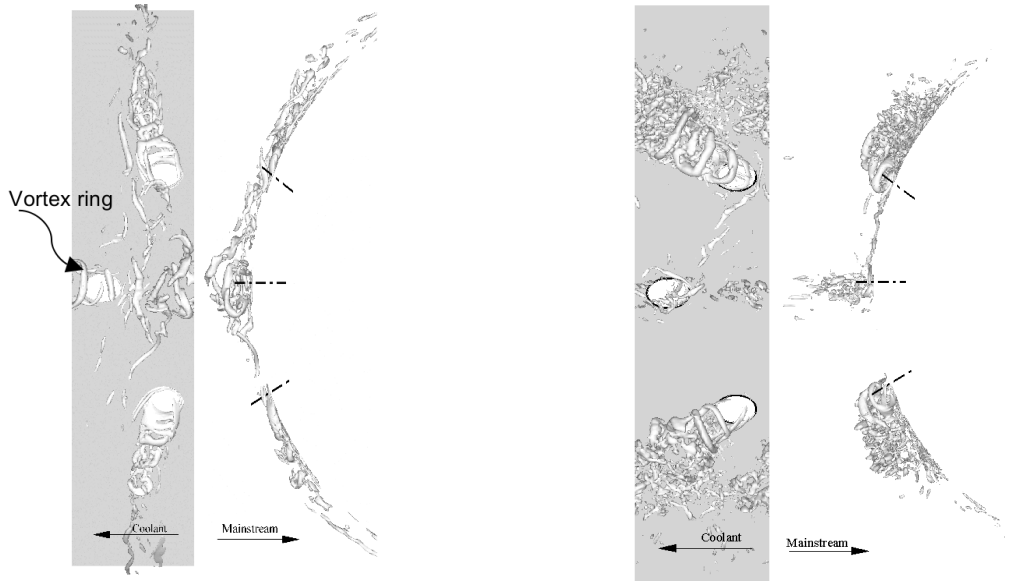

(a) Front View Side View (b) Front View Side View

Figure 5.1.: Structure of coherent vorticity (a) B.R. 0.5 (Iso-surface value = 30) (b) B.R. 2.0. (Iso-surface value = 75)

vorticity for the coolant to mainstream blowing ratio (B.R.) of 0.5 and 2.0. The magnitude (iso-vorticity value, figure 5.1) of the iso-vorticities represents the strength of the vortices. At low blowing ratio (B.R. = 0.5), the vortical coherent structures are well defined. A ring vortex generated at the stagnation jet convects along the stagnation line, which then destabilizes and moves downstream of the vane surface under the influence of the accelerating mainstream flow. The vortex-core generated near the off-stagnation holes quickly aligns to the vane surface and the thermal protection extends from its injection location to a fraction of the pitch. This occurrence is again caused by the influence of accelerating mainstream flow. As the blowing ratio is increased (B.R. = 2.0), the coolant jet penetrates further into the mainstream and is diluted by turbulent diffusion.

Figure 5.2 shows the contours of adiabatic effectiveness that is achieved by the film cooling on the vane surface to protect the vane surface from high temperatures

at different coolant to mainstream blowing ratios. Figure 5.3 shows the line plots of laterally averaged adiabatic effectiveness along the span of the vane surface as a function of downstream location (s/d). The spanwise average is found by averaging across the upper and lower halves of the geometry. The surface adiabatic effectiveness in the stagnation region is a function of the jet penetration and mixing and the amount of coolant injected. At B.R. = 0.5, jet penetration into the mainstream is the smallest amongst the different blowing ratios resulting in the least amount of mixing. Hence it has the largest effectiveness at the stagnation line. However, because of the larger injected mass at B.R. = 1.0 and the redirection of the coolant to the vane surface, the adiabatic effectiveness downstream of the stagnation line is higher than B.R.= 0.5. As the blowing ratio increases further to 1.5 and 2.0, the effectiveness decreases in the immediate vicinity of the stagnation line as the jet penetrates further into the mainstream but increases downstream of stagnation as the jet is redirected to the surface.

The behavior of the adiabatic effectiveness follows the same principles downstream of the second row of injection. There is a balance between the injected coolant mass and jet penetration and mixing. At the lowest blowing ratio of 0.5, the injected coolant remains close to the surface and provides the highest effectiveness immediately downstream of injection. However further downstream the effectiveness decays rapidly, as a result of the smaller mass of coolant and lower lateral spreading of the coolant. As the blowing ratio increases to 1.0, the larger initial penetration of the jet into the mainstream reduces the effectiveness immediately downstream of injection, but this increases as the coolant is pushed back to the surface. At B.R. = 1.5, the jet penetration into the mainstream is larger but because of the larger coolant mass, the redirection of coolant back to the surface dominates the downstream region, and increases the effectiveness. Similar to B.R. = 1.5, at B.R. = 2.0, in spite of the high T.K.E. generated and the intense mixing between the jet and the mainstream, the larger coolant mass injected and the larger lateral spread of the jet dominates the adiabatic effectiveness at the surface.

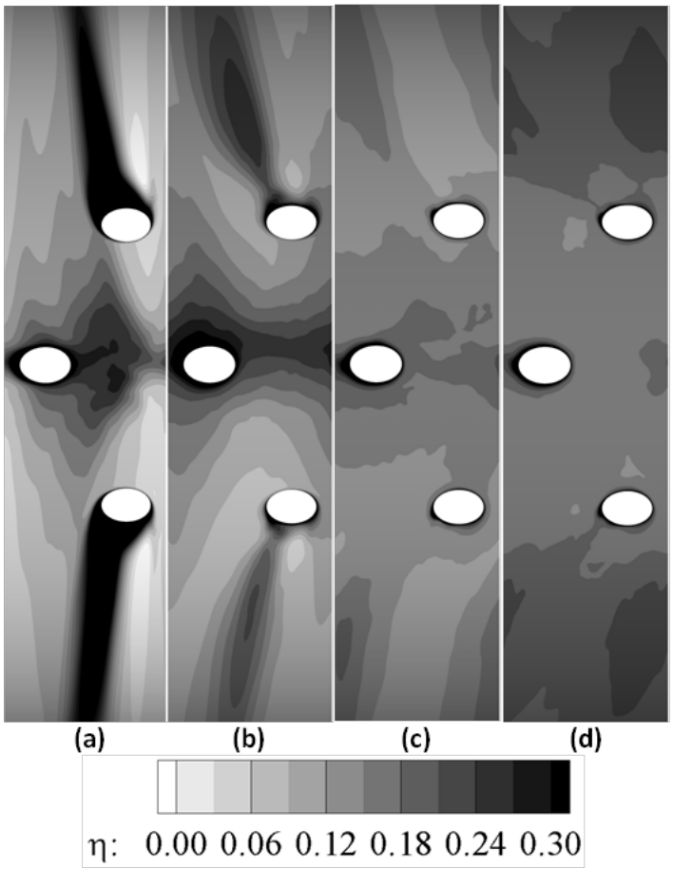

Figure 5.2.: Effectiveness on the vane surface (a) B.R. 0.5 (b) B.R. 1.0 (c) B.R. 1.5 (d) B.R. 2.0

5.1.2 Deposition

To first-order, the amount of ash deposited on the leading edge is a function of the aero-thermal field produced at the leading edge, which is a function of the outer flow scales and the jet-mainstream turbulent interactions in the inner layer. The outer flow scales are governed by the free-stream velocity and the diameter of the leading edge, while the inner turbulent scales are more difficult to characterize but have a large impact on particle aero-thermal state once the particle penetrates into the inner layer. Once the particle is transported to the surface, its deposition on the vane surface depends upon the ash particle composition and its physical properties governed by

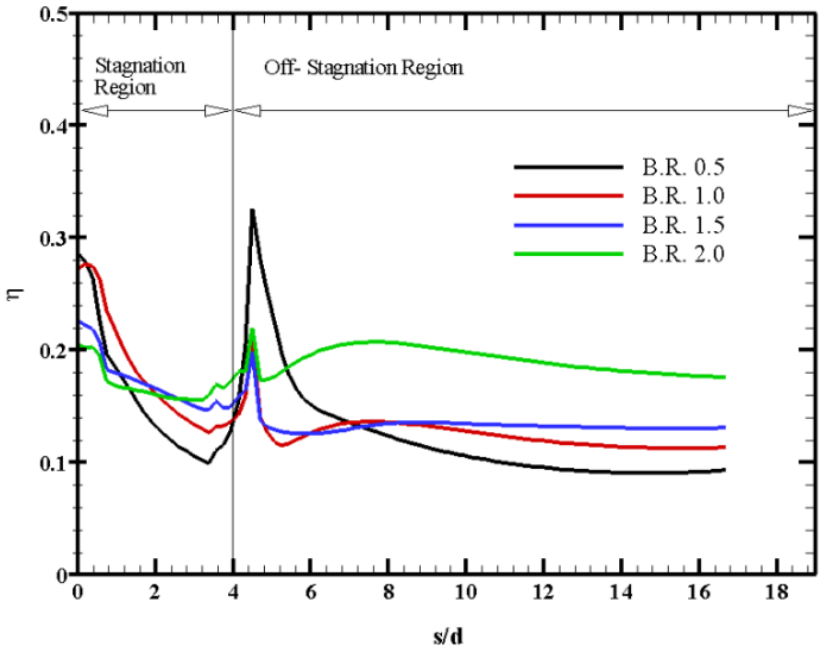

Figure 5.3.: Lateral span averaged effectiveness on the vane surface.

the sticking probability calculated by the critical viscosity model developed in Chapter 4.

5.1.2.1. Syngas ash simulations

Impact efficiency is defined as the percentage of particles that hit the vane surface to the total number of particles injected over the projected vane area at the inlet. Impact efficiency is independent of the ash composition and depends on the Stokes number of the ash particles and their interaction with the coolant jet or solely on the hydrodynamics. Figure 5.4 shows the variation of impact efficiency for 5 μm and 10 μm ash particles as a function of blowing ratio using LES calculations and the DRW model. Less number of 5 micron particles are transported to the surface. Because of the lower Stokes number (0.25), the 5 micron particles tend to follow the outer flow streamlines and few penetrate into the inner layer. Conversely, more of the 10 micron particles with a Stokes number of unity penetrate into the inner layer and impact the surface. A common trend observed for both ash particle sizes is that the percentage of particles impacting the vane surface decreases up to a blowing ratio of 1.5 and then increases for B.R. = 2.0. As the blowing ratio increases from 0.5,

the coolant is successful in pushing some of the particles away from the surface, but as the blowing ratio increases to 2.0, this is countered by the strong entrainment induced by the high blowing ratio, which draws particles toward the surface and increases impaction. Among the two methods used, for most of the cases the DRW model (which uses the mean and turbulent field from the LES calculations) underpredicts impact efficiency as compared to the LES calculations and the degree of underprediction increases as the blowing ratio increases. The probable reason for this is that in spite of using the mean turbulent fields from the LES calculations, the instantaneous random fluctuations produced by the DRW, can only approximate the spatial and temporal correlations of real turbulence, which gets more crucial as they play a larger and larger role in the transport of particles as the blowing ratio increases.

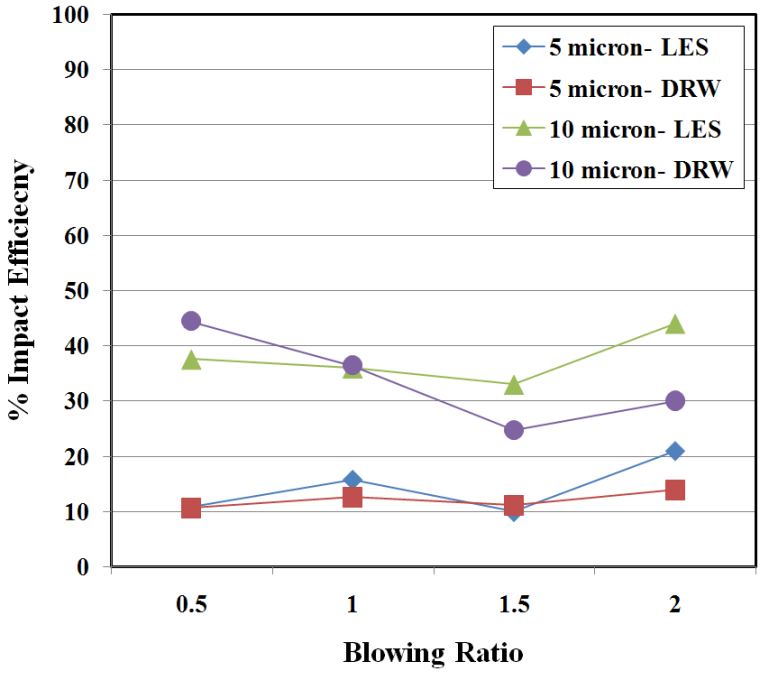

Figure 5.4.: Impact efficiency as a function of blowing ratio.

Similar to impact efficiency, capture efficiency is defined as the percentage of particles that deposit on the vane surface to the total number of particles injected over the projected vane area at the inlet. In addition to the hydrodynamics, the capture efficiency depends on the thermal state of the particle when it impacts the surface

and the composition of the ash, which determines the critical viscosity and hence the sticking probability as developed in Chapter 4. First, to study the deposition trend as a function of the blowing ratio, ND ash sample is chosen. The capture efficiency for other ash samples is discussed later in this section. ND ash sample has a low ash softening temperature that results in a very high sticking probability and the deposition trends would closely follow the impact efficiency trends. Figure 5.5 shows the capture efficiency for ND ash sample at all blowing ratios. For 5 μm ash particles, LES calculations predicts capture efficiency of 10% for B.R. = 0.5 and near 20% at B.R. = 2.0, and the capture efficiency for 10 μm particle averages at about 30% for all blowing ratios. The capture efficiency computed from the DRW model under-predicts deposition when compared to LES calculations at all the blowing ratios for both the particle sizes (exception 5 μm, B.R. = 1.5 and 10 μm, B.R. = 0.5). At B.R. = 2.0, the capture efficiency of ND ash sample is under-predicted by 50% for 5 μm particle sizes and 33% for 10 μm particle sizes by the DRW model. For 10 micron ash, the difference between LES and DRW is larger than in figure 5.4 for the impact efficiencies, signifying that the inaccuracies in simulating the instantaneous flow structures also impacts the prediction of ash temperature as it is transported to the surface. The lower ash particle temperature in DRW is attributed to underprediction of turbulence dispersion, which gives the particles more residence time in the coolant jet fluid to cool down more.

Figure 5.6 shows the capture efficiency on the vane surface for 5 μm particles at B.R. =0.5 and B.R =2.0 (ND ash sample) using LES and the DRW model. At B.R. =0.5, the stagnation jet moves laterally along the vane surface till half the lateral pitch, after which it loses momentum and convects downstream. The deposition in the stagnation region, more or less reflects the coolant trajectory, with little deposition in the coolant path. The regions of high deposition (black regions in figure 5.6) are a result of the ring vortices (Figure 5.1) which are generated by the jet-mainstream interaction and entrain particles to the surface. A similar trend is observed at the

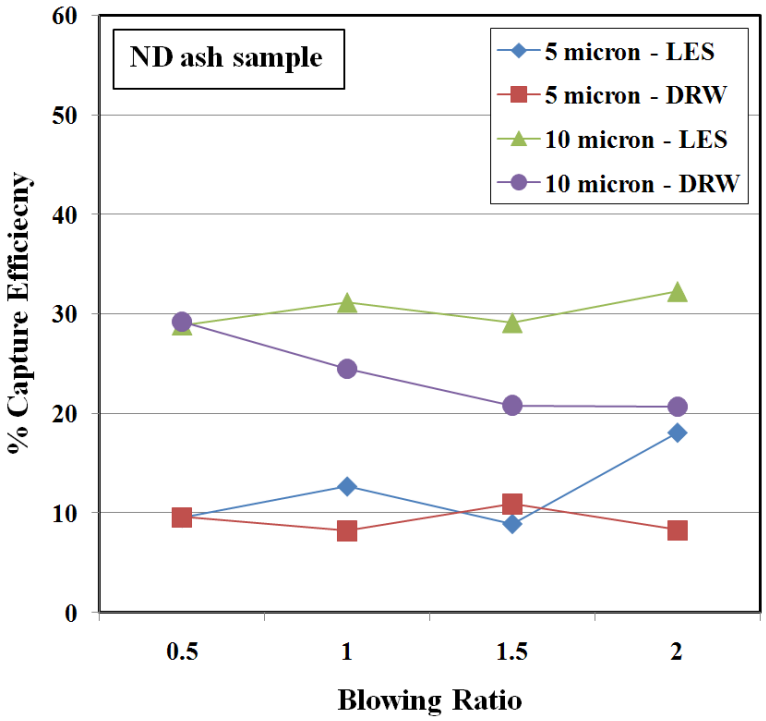

Figure 5.5.: Capture efficiency as a function of blowing ratio for ND ash sample (Table 5.1).

off stagnation coolant injection locations with little deposition in the coolant path. Both, LES and DRW show similar trends with some differences.

However, there are large differences between LES and DRW as the blowing ratio increases to 2.0. At B.R.=2.0, a strong fountain type flow is setup in the stagnation region as the stagnation jet pushes fluid and particles outward, only to the pushed back to the surface at the sides by the oncoming hot freestream flow resulting in deposition not in the region of the stagnation line but immediately downstream. These dynamics are completely missed by the DRW model in spite of having the LES mean turbulent statistics input to the model. Additionally, there is strong entrainment of free-stream fluid on the aft side of the off stagnation coolant holes. This is responsible for transporting particles to the surface and is portrayed by the dark regions in figure 5.6(b). Once again, as in the stagnation region, the entrainment dynamics is not captured by the DRW model. Both of these - the inability to capture the entrainment of particles by the fountain flow in the stagnation region and the

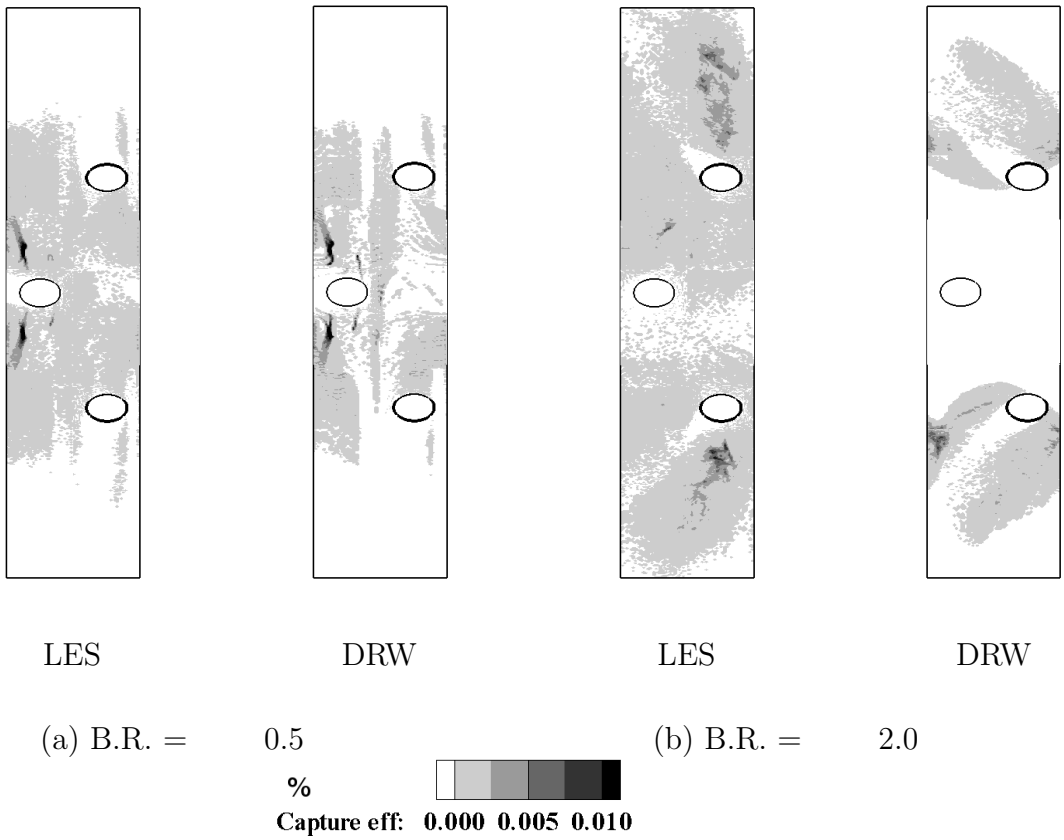

Figure 5.6.: Percentage capture efficiency of 5 μm ash particles on the leading edge vane surface for ND ash sample. (direction of coolant is from right to left)

entrainment of particles by the asymmetric vortex in the off-stagnation jets lead to the underprediction of deposition by the DRW at B.R. = 2.0.

Figure 5.7 shows capture efficiency on the vane surface for particles of 10 μm in size at B.R. = 0.5 and B.R = 2.0 (ND ash sample) for LES and the DRW model. An important difference between the 5 micron and 10 micron particles is the Stokes number. While the Stokes number of 0.25 for the 5 micron particles make them very amenable to manipulation by the flow, the Stokes number of unity of the 10 micron particles make them less amenable to be manipulated easily by the surrounding flow. Hence, while most of the 5 micron particles do not even penetrate into the inner layer but tend to flow around the leading edge in the outer flow, many of the 10 micron particles do, simply as a result of their larger momentum. Therefore, at the low

blowing ratio of 0.5, the particles enter the inner layer and have enough momentum of their own so as not be affected significantly by the coolant jets. The structured striations seen in figure 5.7a is indicative of the particles being insensitive to the perturbations in the flow field as a result of coolant injection and following a straight trajectory mirroring their injection locations upstream. For both methods, the intense deposition seen on the fore side of the stagnation is due to the particles caught up in the vortical ring vortex emanating from the stagnation jet mainstream interaction (Figure 5.1) similar to 5 μm particles (Figure 5.6).

At the high blowing ratio (B.R. = 2.0), both simulations show qualitatively similar deposition pattern for 10 μm particles. Unlike 5 μm particles (B.R. = 2.0), the DRW model for 10 μm ash particle shows deposition in the stagnation region because deposition is driven more by particle inertia and less by the turbulent flow field generated by the jet-mainstream interaction. However, in spite of the patterns of deposition being similar, DRW does underpredict the total capture efficiency by 30% as seen in figure 5.5.

Figure 5.8 shows the capture efficiency of 5 μm ash particles and figure 5.9 shows the capture efficiency of 10 μm ash particles at each blowing ratio for all the ash samples. The blue bar in the figure shows results obtained from time-accurate LES calculations, while the red bar shows results obtained from the DRW model and the dotted line shows deposition based on the softening temperature model ($T_{soft} = 1500K$). A common feature at all blowing ratios and both particle sizes is that even though significant amount of particles impact on the vane surface (Figure 5.4), Lethabo, HN115 and KL1 ash samples show little or no deposition. This is because the three ash samples have a softening temperature above the mainstream temperature and the variation of viscosity with temperature is relatively steep as compared to other ash samples (see Chapter 4: figure 4.2). Conversely the ND ash sample exhibits the largest capture efficiencies followed by WY and ILL ash. Additionally, for both particle sizes, the DRW model under-predicts the capture efficiency when compared to LES calculations and the difference increases with blowing ratio and decreases

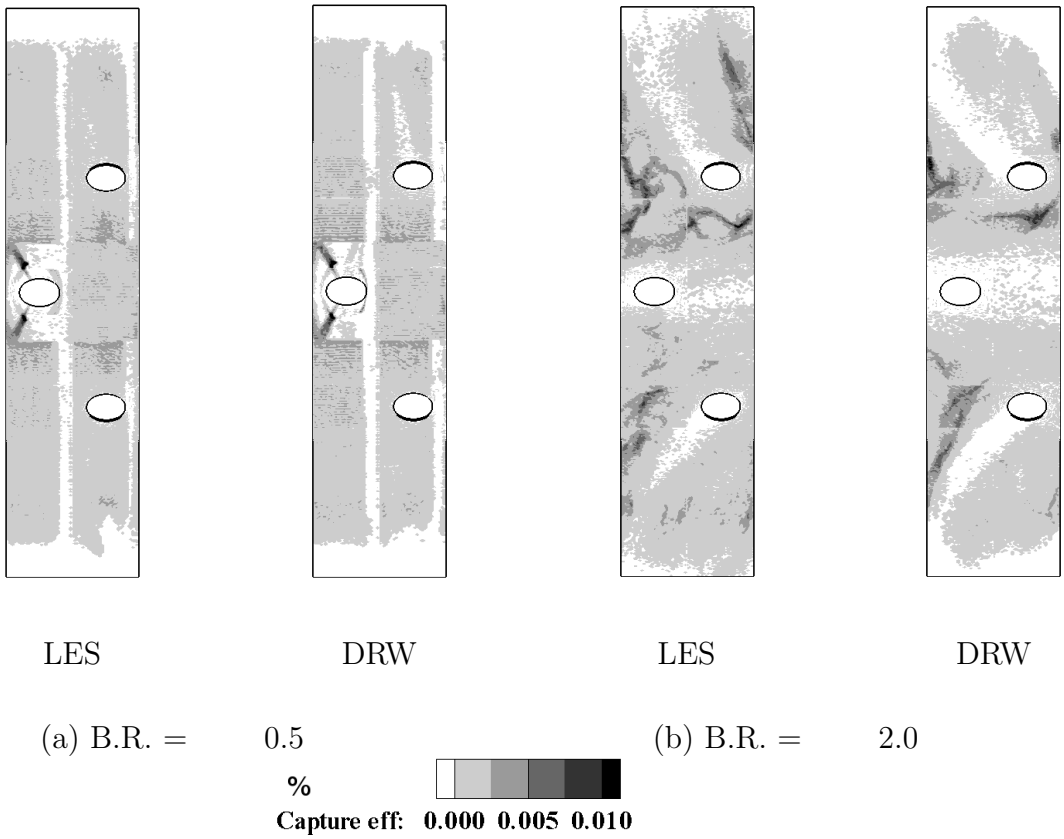

Figure 5.7.: Percentage capture efficiency of 10 μm ash particles on the leading edge vane surface for ND ash sample. (direction of coolant is from right to left)

with increasing size of the particles. This is consistent with the observations made in figures 5.6 and 5.7. At high blowing ratio, high intensity turbulence produced by the jet-mainstream interaction has a large impact on particle trajectory which cannot be reproduced accurately by the DRW model. Alternately, as the particle size increases, particle trajectory is driven more by its inertia and is less dependent on the turbulence generated by the jet mainstream interaction, particularly in the stagnation region.

5.1.2.2. PVC particle simulations

Further computational studies were carried out to compare experimental deposition results obtained from PVC particles. Details of the experiment conducted

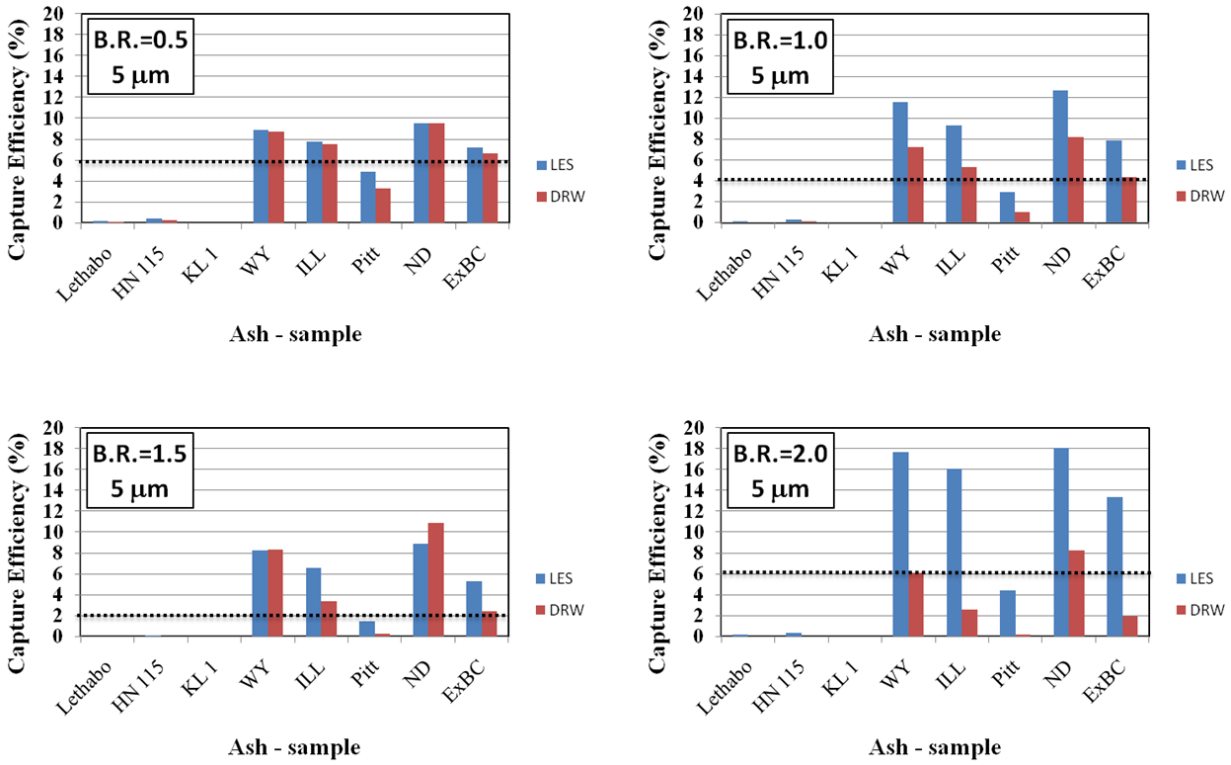

Figure 5.8.: Capture efficiency for all ash samples having a particle size of 10 μm at different blowing ratios (Dotted horizontal line indicates the deposition at $T_{soft} = 1500K$ independent of ash composition)

using PVC particles can be found in [Chapter 4, page 82]. The experiments consider a setup in which a film cooled leading edge vane modeled as a semi-cylinder with a flat after body is placed in the tunnel subjected to a heated freestream laden with PVC particles. Similarity between the computations and experiments is maintained by using flow conditions such that the particle momentum and thermal Stokes numbers in the computations matches the nominal experimental value of 3.13 and 2.4, respectively. The temperature in this study is non-dimensionalized based on the PVC melting temperature ($T = T^*/T^*_{melt}$).

The deposition model assumes an exponential trend, similar to that discussed in Chapter 4, of the form $P_s(T_p) = P_s(T_0) \cdot exp(kT_p)$ for $T_p < T_{melt}$ and $P_s = 1$ for $Tp \geq T_{melt}$. In this chapter, the same calibration constants discussed in Chapter 4 are

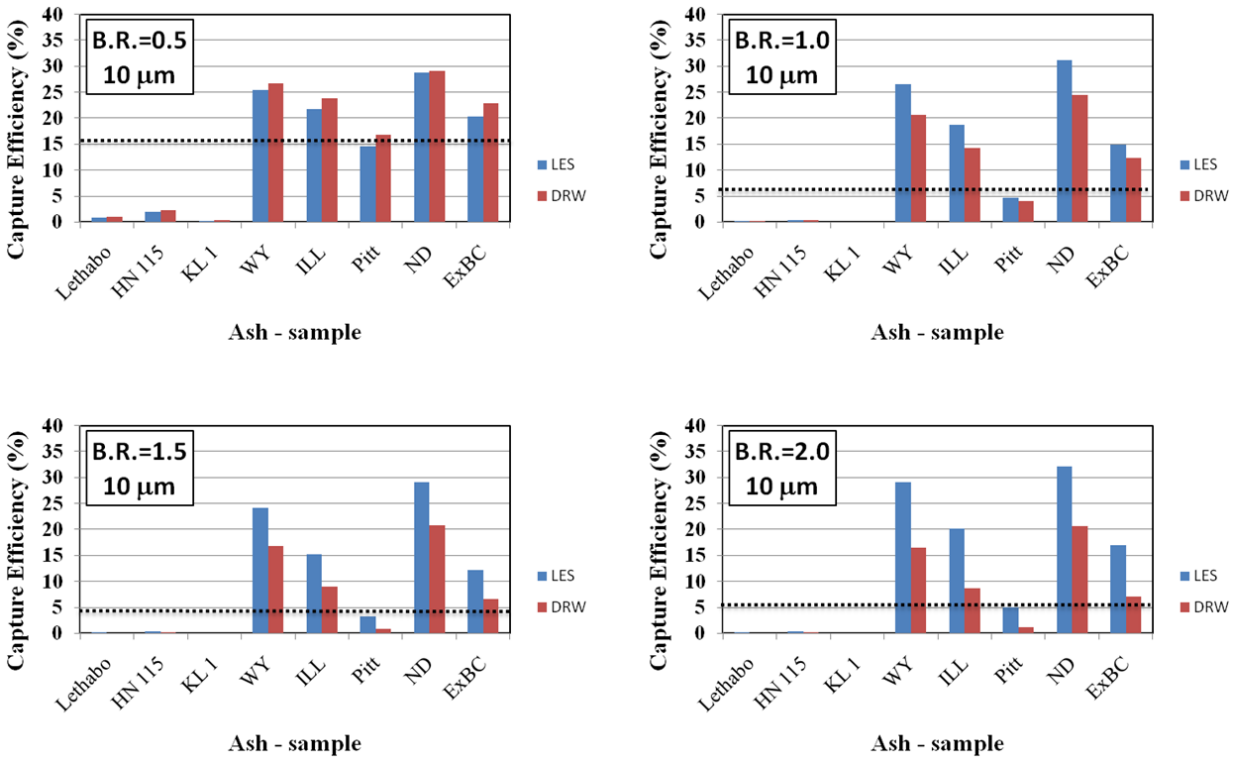

Figure 5.9.: Capture efficiency for all ash samples having a particle size of 5 μm at different blowing ratios (Dotted horizontal line indicates the deposition at $T_{soft} = 1500K$ independent of ash composition)

used: $P_s(T_o)$, sticking probability at 0K, is 1.06E-05 and the constant k is computed assuming that PVC melts at $T^*_{melt} = 533K$ ($P_s = 1$).

Figure 5.10 shows capture efficiency as a function of temperature that is non-dimensionalized by melting temperature of the PVC particles. The plot compares computational results obtained from the DRW model to experiments* at two blowing ratios (B.R. = 1.0 and B.R. = 2.0) for a range of free stream temperatures. The capture efficiency for experiments ranges from 13% - 23% and for the computations they vary from 2% - 17%. The experimental uncertainty is also given in the figure.

*Wood, E., 2010. *Simulated syngas ash deposition on the leading edge of a turbine vane with film cooling.* Masters Thesis, Virginia Tech.

The discrepancies between experimental observations and the computations using the DRW model can be explained as follows.

The deposition model constructed for PVC in Chapter 4 assumes an exponential trend in the sticking probability with particle temperature non-dimensionalized by the melting temperature of PVC ($T = T^*/T^*_{melt}$). The viscosity-temperature curves for some types of PVC particles can be found in the PVC handbook[†] [‡]. In these, while the viscosity decreases with an increase in temperature, the variation is not purely exponential but is more complex and depends on the type of PVC. There are various contents like PVC resin type, plasticizer etc. that formulate the PVC and subsequently govern the viscosity variation with temperature. In the present case, the PVC powder used in the experiments was not characterized well enough for the model to use a more specific variation. Additionally, the melting or softening temperature of PVC can vary anywhere from 373K to 533K. In the model we have used 533K as the melting temperature. If the PVC used in the experiments had a lower melting temperature, than the model would underpredict deposition. Further, the calibration of the deposition model (Chapter 4) is carried out in a flow in which the particles impacting the target surface are at the freestream temperature (T_∞). However, in the film cooled computations, the particle temperature impacting the leading edge will be cooled below T_∞ depending on the coolant distribution on the surface and particle trajectory through the coolant. Hence, the deposition model will predict a lower sticking probability. An additional factor which could have played a role in the underprediction is the possible increase in sticking probability with deposition, which the deposition model does not consider. In summary, the temperature dependent probabilistic deposition model used for the PVC particles could be inadequate and may possibly require better experimental classification on the type of PVC particle used so that a viscosity-temperature correlation from the PVC handbook can be used with the current data.

[†]Titow, W.V., 1984. *PVC Technology.* 4^{th} Ed., Elsevier Applied Sciences Publishing Ltd.

[‡]Buters, G., 1982. *Particulate nature of PVC - Formation, Structure and Processing.* Applied Sciences Publishers Ltd.

Figure 5.12 shows contours of the computational deposition pattern (% capture efficiency) of 24 μm PVC particles for B.R. = 0.5 and B.R. = 2.0 at T = 0.9. At B.R. = 0.5, the complete pitch is coated with PVC particles except the periphery of the stagnation jet and a tiny patch downstream of the off-stagnation jet. At B.R. = 2.0, the stagnation jet is successful in protecting the stagnation line from deposition and also the coolant jets effectively decrease the overall deposition compared to other blowing ratios. Experimental results at a B.R.=2 are also shown for comparison[§].

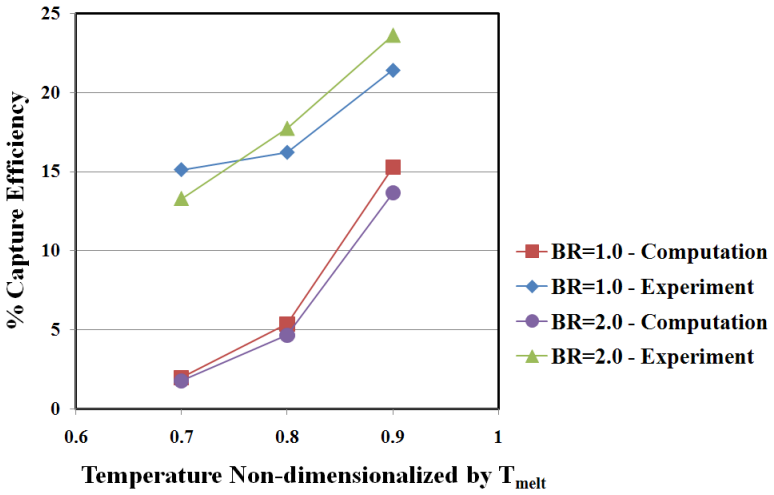

Figure 5.10.: Comparison of capture efficiency as a function of freestream temperature non-dimensionalized by melting temperature of 24 μm PVC particles with experiments. (Computations use the DRW model)

5.2 Summary and conclusions

Syngas ash deposition is investigated on a film-cooled semi-cylinder with a flat after body representative of leading edge turbine vane. The modified deposition model used in this study is based on the critical viscosity approach, discussed in Chapter 4. Large Eddy Simulation is used to model the flow field. Particle dynamics is calculated in two ways: using LES, i.e, exposing the particles to the unsteady instantaneous

[§]Wood, E., 2010. *Simulated syngas ash deposition on the leading edge of a turbine vane with film cooling.* Masters Thesis, Virginia Tech.

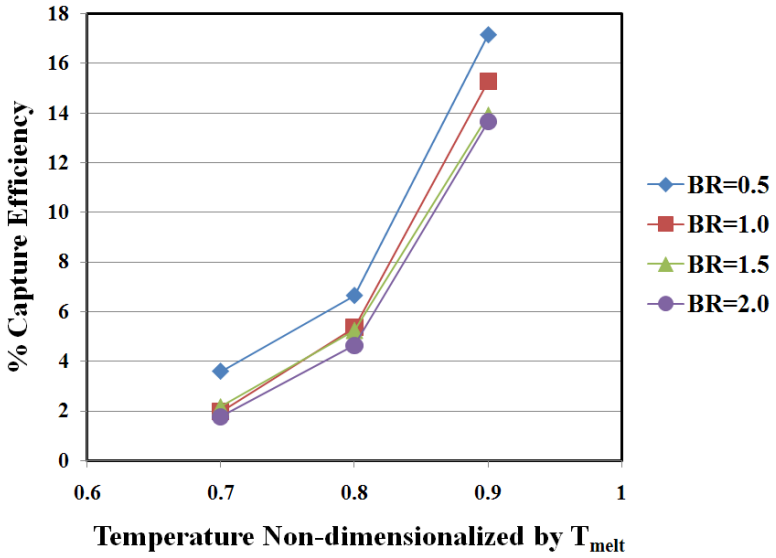

Figure 5.11.: Capture efficiency as a function of freestream temperature non-dimensionalized by melting temperature of 24 μm PVC particles using the DRW model

turbulent eddies, and in the other using the mean flow field and turbulent statistics from the LES to construct an instantaneous field through the DRW model.

Results quantify deposition for two ash particle sizes, 5 μm and 10 μm and coolant to mainstream blowing ratios of 0.5, 1.0, 1.5 and 2.0. Lethabo, HN115 and KL1 ash samples show little or no deposition for both particle sizes and all blowing ratios. Among all the ash samples, ND ash sample shows the highest capture efficiency due to its low softening temperature. A trend that is common to both the particle sizes is that the percentage capture efficiency is the least for blowing ratio of 1.5 as the coolant is successful in pushing the particles away from the surface. However, the percentage capture efficiency increases for blowing ratio of 2.0, as the particles are induced onto the surface by strong mainstream entrainment.

Comparing the use of DRW versus shows that at B.R. = 0.5, the capture efficiency obtained by the DRW is comparable to that obtained by LES calculations. This is because of lower levels of turbulence and most of the deposition appears on the periphery of the coolant path on the vane surface where there is no coolant coverage.

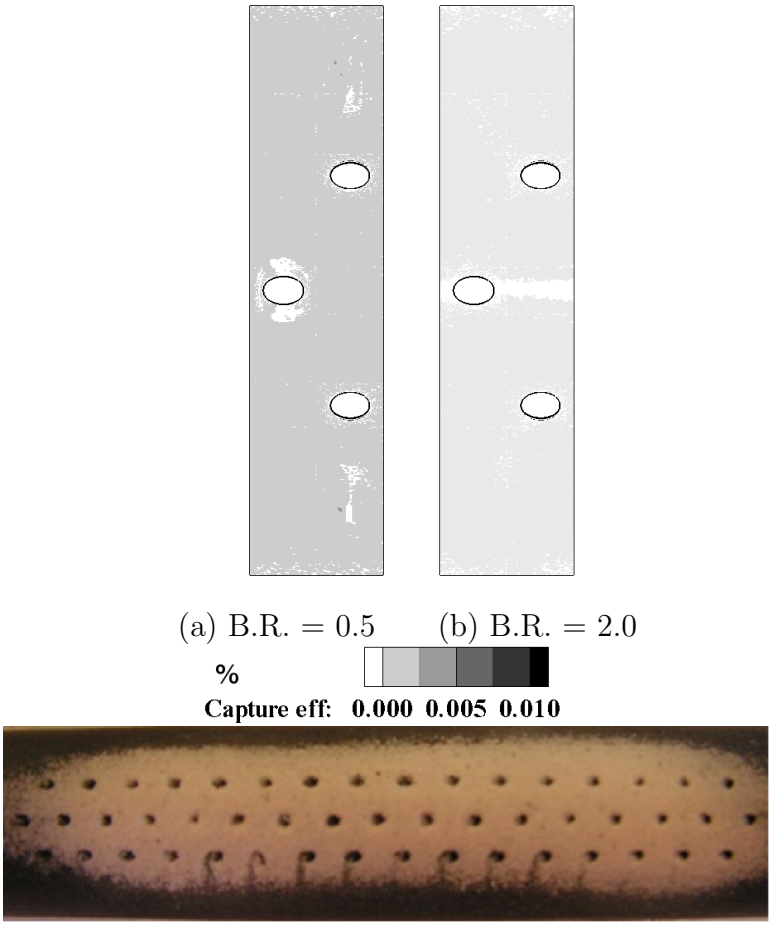

(a) B.R. = 0.5 (b) B.R. = 2.0

(c) Experiment (B.R. = 2.0

Figure 5.12.: Percentage capture efficiency of 24 μm PVC particles on the leading edge vane surface at T = 0.9. (direction of coolant is from right to left)

However, in general, the DRW model under-predicts capture efficiency as compared to LES calculations. The degree of under-prediction increases with blowing ratio. Although, the DRW model simulates turbulent dispersion, the instantaneous random fluctuations produced by the DRW model has little coherence. This becomes more crucial at higher blowing ratios.

Additionally, the DRW model was also extended to compare with deposition experiments using PVC particles. Similarity between the computations and experiments are maintained by matching particle momentum and thermal Stokes numbers

($St_p = 3.13$, $St_{conv} = 2.4$). The deposition model using the same calibration constants for PVC particles as described in Chapter 4. The capture efficiency for experiments ranges from 13% - 23% and the computations vary from 2% - 17%. The discrepancies may be a combined effect of the DRW model and the temperature dependent model used for the PVC particles. The deposition trends with temperature and blowing ratios agree qualitatively with experiments.

APPENDICES

APPENDIX A. FLOW SOLVER

The computational theory relates to two separate phases; the fluid or carrier phase and the particulate matter or dispersed solid phase. Two codes are utilized for performing the research tasks outlined in this dissertation. For LES calculations of the carrier phase, an in-house code GenIDLEST (Generalized Incompressible Direct and Large-Eddy Simulations of Turbulence) developed for application to turbulent flows in complex geometries is used. For steady RANS calculations, a commercial package (Ansys FLUENT) is utilized.

GenIDLEST uses a non-staggered finite-volume mesh with Cartesian velocities and temperature as the primary dependent variables. A fractional-step algorithm, with explicit as well as semi-implicit and implicit time advancement, is used. It uses both Message Passing Interface (MPI) and OpenMP for parallel execution. The equations are mapped from physical ($\vec{x}$) to logical/computational space ($\vec{\xi}$) by a boundary conforming transformation $\vec{x} = \vec{x}(\vec{\xi})$, where $\vec{x} = (x, y, z)$ and $\vec{\xi} = (\xi, \eta, \zeta)$. The equations are non-dimensionalized by a suitable length (L^*) and velocity scale (U^*). The transformed governing equations for incompressible constant property assumption is written in conservative nondimensional form as:

Mass

$$\frac{\partial}{\partial \xi_j}\left(\sqrt{g}\bar{U}^j\right) = 0 \tag{A.1}$$

Momentum

$$\begin{aligned}\frac{\partial}{\partial t}\left(\sqrt{g}\bar{u}_i\right) \;+\; & \frac{\partial}{\partial \xi_j}\left(\sqrt{g}\bar{U}^j\bar{u}_i\right) = -\frac{\partial}{\partial \xi_j}\left(\sqrt{g}(\vec{a}^j)_i\bar{p}\right) \\ & +\frac{\partial}{\partial \xi_j}\left(\left(\frac{1}{Re}+\frac{1}{Re_t}\right)\sqrt{g}g^{jk}\frac{\partial \bar{u}_i}{\partial \xi_k}\right) + \sqrt{g}S_{\bar{u}_i}\end{aligned} \tag{A.2}$$

Additional details of the in-house code, GenIDLEST, developed by Dr. Tafti can be found in *Tafti, D. K., 2001. Genidlest - a scalable parallel computational tool for simulating complex turbulent flows. Proceedings of the ASME Fluids Engineering Division, 256, pp. 347-356 [1].*

Energy

$$\frac{\partial}{\partial t}\left(\sqrt{g}\bar{\theta}\right) + \frac{\partial}{\partial \xi_j}\left(\sqrt{g}\bar{U}^j\bar{\theta}\right) = \frac{\partial}{\partial \xi_j}\left(\left(\frac{1}{PrRe}+\frac{1}{Pr_tRe_t}\right)\sqrt{g}g^{jk}\frac{\partial\bar{\theta}}{\partial\xi_k}\right)+\sqrt{g}S_{\bar{\theta}} \qquad (A.3)$$

where $\vec{a}^i$ are the contravariant basis vectors [*] , $\sqrt{g}$ is the Jacobian of the transformation, $g^{(ij)}$ is the contravariant metric tensor, $\sqrt{g}U^j = \sqrt{g}(\vec{a}^j)_i u_i$ is the contravariant flux vector, u_i is the Cartesian velocity vector, and θ is the non-dimensional temperature. $S_{\bar{u}_i}$ and $S_{\bar{\theta}}$ are additional source terms in the momentum and energy equation, respectively. The overbar in the continuity, momentum and energy equations denote grid filtered quantities. Re_t is obtained from the subgrid stress model.

Eqns. (A.1-A.3) are solved using an overlapping multi-block structured mesh topology. In each block the equations are mapped from physical ($\vec{x}$) to computational space ($\vec{\xi}$) by a boundary conforming transformation $\vec{\xi} = \vec{x}(\vec{\xi})$, where $\vec{x} = (x, y, z)$ and $\vec{\xi} = (\xi, \eta, \zeta)$. Inter-block connectivity can be structured ($\xi+$ face adjoining a $\xi-$ face) or unstructured. In an unstructured inter-block topology a $\xi-$ face boundary can adjoin a η or ζ face with arbitrary axes orientations.

GenIDLEST can handle non-matching or non-conformal boundary interfaces, i.e. there does not have to be a one-to-one correspondence between meshes of adjoining block faces. This allows additional flexibility in meshing complex domains and can also be used for local refinement. In such cases dependent variables have to be interpolated between faces. For this purpose, bilinear interpolation functions are used together with integral conservation of mass, momentum, and energy fluxes. The fluxes are conserved globally (over face) versus locally, which would constrain the generality of the non-matching interfaces.

The multiblock framework provides a natural framework for parallelization. Depending on the total number of blocks and processors, each processor is assigned multiple blocks. Further, within each block virtual cache blocks are used. The virtual blocks are not explicitly reflected in the data structure but are used only in the

[*]The notation $(\vec{a}^j)_i$ is used to denote the i-th component of vector $\vec{a}^j$, $(\vec{a}^j)_i = \partial\xi_j/\partial x_i$

solution of linear systems. The motivation to construct much smaller cache blocks is to extract performance on cache-based hierarchical memory systems. These small cache blocks form the basic computing units for preconditioning linear systems. Hence, underneath the coarse grained parallelism of MPI processes, there exists additional parallelism across multiple blocks, or across the mesh nodes in each block, and across the multiple cache blocks. Hence, GenIDLEST is instrumented for coarse-grained parallelism with MPI and for embedded or fine-grained parallelism with OpenMP.

The governing equations are discretized with a conservative finite-volume formulation. In non-orthogonal coordinate systems, there are a number of choices in the selection of the grid topology and the dependent variable in the momentum equations. In GenIDLEST, we adopt a non-staggered grid topology with Cartesian velocities as dependent variables. The Cartesian velocities, pressure, and temperature are calculated and stored at the cell center, whereas contravariant volume fluxes are stored and calculated at the cell faces. The convection term can be approximated in a number of different ways. Presently, there are two basic approximations, second-order central difference and the third-order upwind biased approximation, to calculate the cell face values. These two approximations can either be used in their basic form or combined with TVD criteria to preserve monotonicity of the convected variable. In addition to the TVD limiter, a multi-dimensional flux limiter [2] is also implemented. The flux limiter is based on the less restrictive universal limiter proposed by Leonard [3]. In this scheme, the intermediate velocities are first calculated with the base approximations and then checked for monotonicity in a multidimensional framework. Two subgrid-scale stress models are available at this time, the Smagorinsky [4] and the dynamic Smagorinsky model [5]. Additionally, several high and low Re-number RANS models, based on the $k-\omega$ model [6–8] and Menters [9–11] models are also available.

A variety of boundary conditions are available in GenIDLEST, and they are specified individually for each computational block. With the exception of periodic

or inter-block boundaries, each boundary face can have multiple boundary conditions assigned to it.

1. Periodic or inter-block boundaries: Both of these boundaries precipitate the same action, which involves exchanging boundary information between adjacent faces. For unstructured block connectivity and/or non-conformal interfaces, the boundary information is filtered by coordinate rotations and interpolations as required. Coordinate rotations and interpolation factors are calculated at the beginning of each run.

2. Wall boundary: When the velocity normal to the boundary is zero or there is no influx (outflux) of mass, the boundary is specified as a wall. Wall boundaries can have slip velocities imposed on them and temperature or heat flux (gradients) specified.

3. Inlet boundary: When there is a known net influx (outflux) of mass from the boundary, it is specified as an inlet. Only temperature can be specified at this boundary.

4. Outflow boundary: Outflow boundaries use a convective boundary condition in which the dependent variable is allowed to convect out of the domain. Both temperature and heat flux can be specified.

5. Symmetry boundary: At this boundary, the normal velocity and gradients of tangential velocities and temperature are set to zero.

6. Pressure boundary: Pressure, and not velocity, is specified at this boundary. The velocities are derived from the flow generated by the pressure. For increased flexibility in meshing, internal blanked zones or solid obstacles can also be specified in each computational block. Boundary conditions on these regions use Dirichlet conditions on velocities, including suction or blowing. Temperature or heat flux can be specified.

The discretized continuity and momentum equations are integrated in time using a projection method. The temporal advancement is performed in two steps, a predictor step, which calculates an intermediate velocity field, and a corrector step, which calculates the updated divergence free velocity at the new time step. The predictor step can be fully explicit in time, semi-implicit, in which the viscous terms are treated implicitly, or fully-implicit, in which the convection terms are also treated implicitly. All methods are incorporated in GenIDLEST. The semi-implicit method is useful for low Reynolds number flows and in flows with large effective viscosities by allowing larger time steps than what would be allowed by the viscous stability condition. The fully-implicit method allows the use of larger time-steps in high Reynolds number flows. The corrector step uses the continuity equation to formulate the pressure equation. The computed pressure is then used to update the intermediate velocity field.

The linear system generated in the solution of the pressure equation and the implicit treatment of viscous terms is non-symmetric on non-orthogonal meshes. Further, the presence of non-conformal or non-matching boundaries creates additional strong non-symmetries. In GenIDLEST, Krylov methods based on the method of Conjugate Gradients (CG) for symmetric systems and BiCGSTAB or GMRES(m) for non-symmetric systems. These are coupled with preconditioners based on a two-level Additive Schwarz domain decomposition (DD) method [12–14].

GenIDLEST is very portable between different computer architectures and compilers. It has a front-end Java interface for the creation of input files. A number of post-processing utilities are present, including the ability to obtain mean and turbulent statistics in a distributed computing environment, time-dependent data dumps for analysis and visualization, and vortex identification techniques based on the $\nabla\vec{u}$ [15] and λ_2 method [16].

A.1 LES subgrid scale modeling

For LES, Re_t is the inverse of the non-dimensional subgrid eddy-viscosity and is modeled by the Smagorinsky model [4] as

$$\frac{1}{Re_t} = C_s^2(\sqrt{g})^{(2/3)}|\bar{S}|$$

where $|\bar{S}|$ is the magnitude of the strain rate tensor given by $|\bar{S}| = \sqrt{(2\bar{S}_{ik}\bar{S}_{ik})}$. The Smagorinsky constant C_s^2 is obtained via the dynamic procedure [5] and is constrained to be positive. To this end, a second test filter, denoted by $\hat{G}$, is applied to the filtered governing equations with the characteristic length scale of $\hat{G}$ being larger than that of the grid filter, $\bar{G}$ (usually $\hat{\triangle} = 2\bar{\triangle}$) . The test filtered quantity is obtained from the grid filtered quantity by a second-order trapezoidal filter which is given by $\hat{\phi} = \frac{1}{4}(\bar{\phi}_{i-1} + 2\bar{\phi}_i + \bar{\phi}_{i+1})$ in one dimension. The resolved turbulent stresses, representing the energy scales between test and grid filters, $L_{ij} = \widehat{\bar{u}_i\bar{u}_j} - \hat{\bar{u}}_i\hat{\bar{u}}_j$, are then related to the subtest, $T_{ij} = \widehat{u_iu_j} - \hat{\bar{u}}_i\hat{\bar{u}}_j$, and subgrid-scales stresses $\tau_{ij} = \overline{u_iu_j} - \bar{u}_i\bar{u}_j$ though the identity, $L_{ij}^a = T_{ij}^a - \hat{\tau}_{ij}^a$.The anisotropic subgrid and subtest-scale stresses are then formulated in terms of the Smagorinsky eddy viscosity model as:

$$\hat{\tau}_{ij}^a = -2C_s^2(\sqrt{g})^{(2/3)}\widehat{|\bar{S}|\bar{S}}_{ij}$$

$$T_{ij}^a = -2C_s^2\alpha(\sqrt{g})^{(2/3)}|\hat{\bar{S}}|\hat{\bar{S}}_{ij} \tag{A.4}$$

Using the identity

$$\hat{L}_{ij}^a = \hat{L}_{ij} - \frac{1}{3}\delta_{ij}L_{kk} = -2C_s^2(\sqrt{g})^{(2/3)}\left[\alpha|\hat{\bar{S}}|\hat{\bar{S}}_{ij} - \widehat{|\bar{S}|\bar{S}}_{ij}\right] = -2C_s^2(\sqrt{g})^{(2/3)}M_{ij} \tag{A.5}$$

Here α is the square of the ratio of the characteristic length scale associated with the test filter to that of grid filter and is taken to be $\left[\hat{\bar{\triangle}}_i/\bar{\triangle}_i = \sqrt{6}\right]$ for a repre-

sentative one-dimensional test filtering operation. Using a least-squares minimization procedure of Lilly, a final expression for C_s^2 is obtained as:

$$C_s^2 = -\frac{1}{2}\frac{1}{(\sqrt{g})^{(2/3)}}\frac{L_{ij}^a \cdot M_{ij}}{M_{ij} \cdot M_{ij}} \tag{A.6}$$

where $M_{ij} = (\hat{\triangle}/\bar{\triangle})^2|\hat{\bar{S}}|\hat{\bar{S}}_{ij} - \widehat{|\bar{S}|\bar{S}}_{ij}$. The value of C_s^2 is constrained to be positive by setting it to zero when $C_s^2 < 0$.

A.2 Modeling particle dynamics

The equation of motion for a representative particle in the Lagrangian framework can be written as:

$$\begin{aligned} \frac{d\vec{x}_p^*}{dt^*} &= \vec{v}_p^* \\ m_p^*\frac{d\vec{v}_p^*}{dt^*} &= \vec{F}_{drag}^* + \vec{F}_{bouyancy}^* - \vec{F}_{addedmass}^* + \vec{F}_{pressure}^* + \\ &\quad \vec{F}_{basset}^* + \vec{F}_{lift}^* + \vec{F}_{brownian}^* + \vec{F}_{thermophoretic}^* \end{aligned} \tag{A.7}$$

where

$$\vec{F}_{drag}^* = \frac{m_p^*}{\tau_v^*}\left(\vec{v}^* - \vec{v}_p^*\right) + m_p^*\left(\frac{3}{4}\frac{\mu^*}{\rho_p^*}\nabla^* 2\vec{v}^*\right)$$

The first term is due to Stokes drag in a uniform flow, whereas the second term is a correction to the assumption of uniform flow and is important for large particle diameters within regions of strong shear (Faxen force). The induced drag force due to particle rotation (Magnus effect), which is only consequential for large rotating particle is neglected. τ_v is the particle relaxation time or inertial time constant and is given by $\tau_v = 4\rho_p^* d_p^*/(3\rho_f^* C_D^*|\vec{v}^* - \vec{v}_p^*|)$. For particle Reynolds number (Re_p), from Stokes drag law ($C_D = 24/Re_p$), the particle relaxation time reduces to a convenient form as $\tau_v = \frac{\rho_p^* d_p^* 2}{18\mu^*}$

For $1 \leq Re_p \leq 400$, a more accurate form of the drag law is $C_D = 24/Re_p^{0.646}$. Other fits to the drag law are also available. The relaxation time is a measure of the time taken by a particle to adjust to the flow velocity of the continuous phase. Larger the particle relaxation time, larger is the effect of its inertia and it responds slowly to

changes in the fluid velocity field. The second term in the drag force is the additional drag on a particle in regions of high shear and can be neglected for small particles and low shear rates. A true measure of particle response to its surrounding fluid is when the inertial time constant of the particle is compared to the characteristic time scale of the flow field. If U_c^* is the characteristic velocity and L_c^*, the characteristic length scale of the flow then the Stokes (St_p) number

$$St_p = \frac{\tau_v^*}{\tau_f^*} = \frac{\rho_p^* d_p^* 2}{18\mu^*} \frac{U_c^*}{L_c^*}$$

is a measure of the relative inertial response of the particle compared to how quickly changes take place in the flow field. If $St_p << 1$, the particle responds almost immediately to changes in the carrier flow fluid. On the other hand for $St_p >> 1$, the particle is always responding to changing flow conditions and is limited by its own inertia in its response to the changing fluid conditions.

The buoyancy force is driven by density differences between the dispersed and continuous phase and is given by:

$$\vec{F}_{buoyancy}^* = (m_p^* - m_f^*)\vec{g}^*$$

The added mass force is a result of relative particle acceleration and the resultant force which it experiences in accelerating/decelerating the fluid surrounding it and is given by:

$$\vec{F}_{addedmass}^* = \frac{1}{2} m_f^* \frac{d}{dt^*}(\vec{v}_f^* - \vec{v}_p^*)$$

The effective force on the particle brought about by pressure gradients in the continuous phase is given by:

$$\vec{F}_{pressure}^* = -m_f^* \frac{d\vec{v}^*}{dt^*}$$

Both, the added mass term and pressure term can be neglected when $\rho_p^*/\rho_f^* >> 1$ and $St_p < 1$.

The Basset history force is a result of unsteady relative flow in the vicinity of the particle and is proportional to the amount of relative acceleration which is given by:

$$\vec{F}^*_{basset} = \frac{3}{2} d^*_p 2\sqrt{\pi \rho^*_f \mu^*_f} \int_{t^*_0}^{t^*} \frac{1}{\sqrt{t^* - t^{*\prime}}} \frac{d(\vec{v}^* - \vec{v}^*_p)}{dt^{*\prime}} dt^{*\prime}$$

The Saffman lift force generated in the particle due to strong velocity gradients in the flow field in a direction perpendicular to particle motion is given by:

$$\vec{F}^*_{lift} = 5.2\ m^*_p \sqrt{v^*_f} \frac{\rho^*_f}{\rho^*_p d^*_p} \frac{(v^*_j - v^{*p}_j)\epsilon^*_{ij}}{(\epsilon^*_{lk}\epsilon^*_{lk})^{1/4}}$$

, where $\epsilon^*_{ij} = \frac{1}{2}\left(\frac{\partial v^*_i}{\partial x^*_j} + \frac{\partial v^*_j}{\partial x^*_i}\right)$. This force can be neglected except it regions of high velocity gradients as in the near wall region of boundary layers.

For submicron particles, random Brownian motion caused by the bombardment of fluid molecules on the particle result in a net force given by:

$$\vec{F}^*_{brownian} = \forall \cdot G_i \sqrt{\pi S^*_0 / \triangle t^*}$$

where the spectral intensity $S_0 = 216\mu^*_f K^* T^*_f / (\pi^2 d^{*5}_p (\rho^*_p / \rho^*_f)^2 C_c)$, K^* is Boltzmann constant $= 1.38 \times 10^{-23} J/K$, C_c is a correction for particle sizes approaching the mean free path of the carrier fluid, and G_i is a zero-mean, unit variance-independent Gaussian random number. Brownian motion could potentially be important for very small particles in regions of low velocity in the vicinity of walls.

For very small particles or low relaxation times, thermophoretic effects brought about by large temperature gradients may contribute to the forces acting on particles.

$$\vec{F}^*_{thermophoretic} = -m^*_p k_T \frac{\nu^*_f}{\tau^*_v} \frac{1}{T^*_f} \nabla T^*_f$$

where $k_T = 3.34K/(1+K)$, $K = 15\mu^*_f R/k^*_p$ in the limit as Knudsen number tends to zero (mean free path of molecules $<< d^*_p$), k^*_p is the thermal conductivity of the particle and R the gas constant.

Similarly, the characteristic equation describing heat transfer between the dispersed and continuous phase is given by:

$$\begin{aligned} m_p^* C_p^* \frac{dT_p^*}{dt^*} &= \pi d_p^* k_f^* Nu \left(T_f^* - T_p^*\right) \\ &\quad -\epsilon\sigma^* \pi d_p^* 2 \left(T_p^* 4 - T_f^* 4\right) \end{aligned} \tag{A.8}$$

where Nu is the Nusselt number given by $Nu = 2 + 0.6Pr^{1/3}Re_p^{1/2}$. For $Re_p << 1$, when conduction heat transfer dominates, $Nu = 2$. Under these conditions and when radiative heat transfer is negligible, a thermal time constant can be defined as: $\tau_t^* = \frac{d_p^* 2 \rho_p^* C_p^*}{12 k_f^*} = \frac{3}{2} Pr \frac{C_p^*}{C_f^*} \tau_v^*$, where C_f^* is the specific heat of the fluid.

A.3 Bibliography

[1] Tafti, D. K., 2001. "Genidlest - a scalable parallel computational tool for simulating complex turbulent flows". *Proceedings of the ASME Fluids Engineering Division, FED,* ***256***, pp. 347–356.

[2] Thuburn, J., 1996. "Multidimensional flux-limited advection schemes". *Journal of Computational Physics,* ***123***, pp. 74–83.

[3] Leonard, B. P., 1991. "The ultimate conservative difference scheme applied to unsteady one-dimensional advection". *Computational Methods in App. Mech. and Engineering,* ***88***, pp. 17–74.

[4] Smagorinsky, J., 1963. "General circulation experiments with the primitive equations. i. the basic experiment". *Monthly Weather Review,* ***91***, pp. 99–164.

[5] Piomelli, M. G. U., Moin, P., and Cabot, W., 1991. "A dynamic subgrid-scale eddy viscosity model". *Physics of Fluids A,* ***3***, pp. 1760–1765.

[6] Wilcox, D., 1994. "Simulation of transition with a two-equation turbulence model". *AIAA Journal,* ***32***(2), pp. 247–255.

[7] Wilcox, D., 1998. "Turbulence modeling for cfd". *DCW Industries, Second Ed.*

[8] Wilcox, D., 1998. "Reassessment of the scale-determining equation for advanced turbulence models". *AIAA Journal,* ***26***(11), pp. 1299–1310.

[9] Menter, F., 1993. "Zonal two equation turbulence models for aerodynamic flows". 24^{th} *Fluid Dynamics Conference, AIAA Paper 93-2906.*

[10] Menter, F., 1992. "Improved two-equation $k-\omega$ turbulence models for aerodynamic flows". *NASA Technical Memorandum 103975.*

[11] Menter, F., 1993. "Zonal two equation $k-\omega$ turbulence models for aerodynamic flows". *AIAA Paper 93-2906*.

[12] Wang, G., and Tafti, D., 1998. "Parallel performance of additive schwarz preconditioners on origin 2000". *Advances in Engineering Software,* ***29***(3-6), p. 433.

[13] Wang, G., and Tafti, D., 1999. "Performance enhancement on microprocessors with hierarchical memory systems for solving large sparse linear systems". *International Journal of Supercomputing Applications and High Performance Computing,* ***13***(1), p. 63.

[14] Wang, G., and Tafti, D., 1998. "Uniprocessor performance enhancement by additive schwarz preconditioners on origin 2000". *Advances in Engineering Software,* ***29***(3-6), p. 425.

[15] Chong, M., Perry, A., and Cantwell, B., 1990. "A general classification of three-dimensional flow fields". *Physics of Fluids A,* ***2***, pp. 765–777.

[16] Jeong, J., and Hussain, F., 1995. "On the identification of a vortex". *Journal of Fluid Mechanics,* ***285***, pp. 69–94.

APPENDIX B. COMPARISON OF RANS SIMULATIONS TO LES

Abstract

The modified deposition model based on the critical viscosity approach is used to predict flyash deposition on the film-cooled leading edge vane geometry. Chapter 4 discusses the validation of the results obtained from the deposition model with the experiments of Crosby et. al. [1] on a flat, 45° wedge shape geometry. Deposition on 3-row film-cooled leading edge vane geometry is revisited here to see the effect of deposition below the softening temperature. Furthermore, this appendix also investigates the results obtained from a commercial flow solver (FLUENT) for steady state RANS modeling. The RANS simulations use the $SST\ k-\omega$ turbulence model to predict the mean flow and temperature field. The results obtained from the $SST\ k-\omega$ turbulence model are compared against results obtained from Large Eddy Simulation (LES). Results discuss coolant to mainstream blowing ratios of 1.0, 1.5 and 2.0 and ash particles of 5 microns in diameter. First, adiabatic effectiveness obtained from steady state RANS is compared to LES and subsequently, particle deposition results are quantified and compared. Results show that the $SST\ k-\omega$ turbulence model over-predicts the stagnation coolant jet penetration into the mainstream and under-predicts turbulent mixing. Even though the spanwise averaged effectiveness follow similar trends, the $SST\ k-\omega$ turbulence model over-predicts adiabatic effectiveness by 2 times for B.R. = 2.0 (s/d = 6) when compared to LES. For particle transport in LES, most of the scales are resolved by the simulations. However, for steady state RANS calculations, the turbulence dispersion of particle transport is modeled using a stochastic approach (Discrete Random Walk model) to account for instantaneous velocity fluctuations. For RANS simulations, over-prediction of jet penetration

Modified deposition methodology is used to predict deposition, refer Chapter 4 for further details

causes the coolant core to successfully push the particles away from the vane surface. Furthermore, at B.R. = 2.0, RANS predicts much higher adiabatic effectiveness, so whichever particles reach the vane surface are cooled below their softening temperature and possess a very low sticking probability resulting in little or no deposition whereas, LES predicts a capture efficiency of $\sim 14\%$. In summary, RANS is unable to correctly predict ash deposition in the film-cooled leading edge region when compared against time accurate high resolution LES calculations.

B.1 Domain description

B.1.1 Geometry description

The computational domain of interest models the leading edge of a vane as a semi-cylindrical form with a flat after body (Figure B.1). Three rows of film cooling holes are employed. One row is located at stagnation and two rows are located at $\pm$4d, on either side of the stagnation line. The lateral pitch spacing (P) between two holes for any given row is 4.5d, and the relative position of the holes on the upper half and lower half are staggered with respect to the stagnation hole. The origin is fixed at the center of the domain at stagnation with the stagnation hole located at z = -1.125d and staggered off-stagnation holes located at z = 1.125d. The coolant hole diameter ratio (D/d) is 21.5 and the length ratio of the coolant pipe (L/d) is 10.75. The coolant is injected laterally at 45° to the surface with a compound angle of 90° to the mainstream. Figure B.1 shows the computational domain of interest. It extends 10D in the x-direction, 5D in y-direction and 4.5d in the spanwise z-direction.

B.1.2 Grid description

A key feature for any numerical simulation is having a mesh with minimally skewed cells and superior near wall resolution. Here a multi-block framework is adopted for meshing the computational domain of interest. Gridgen, a commercial numerical grid generation software is used to create this multi-block grid. The grid is

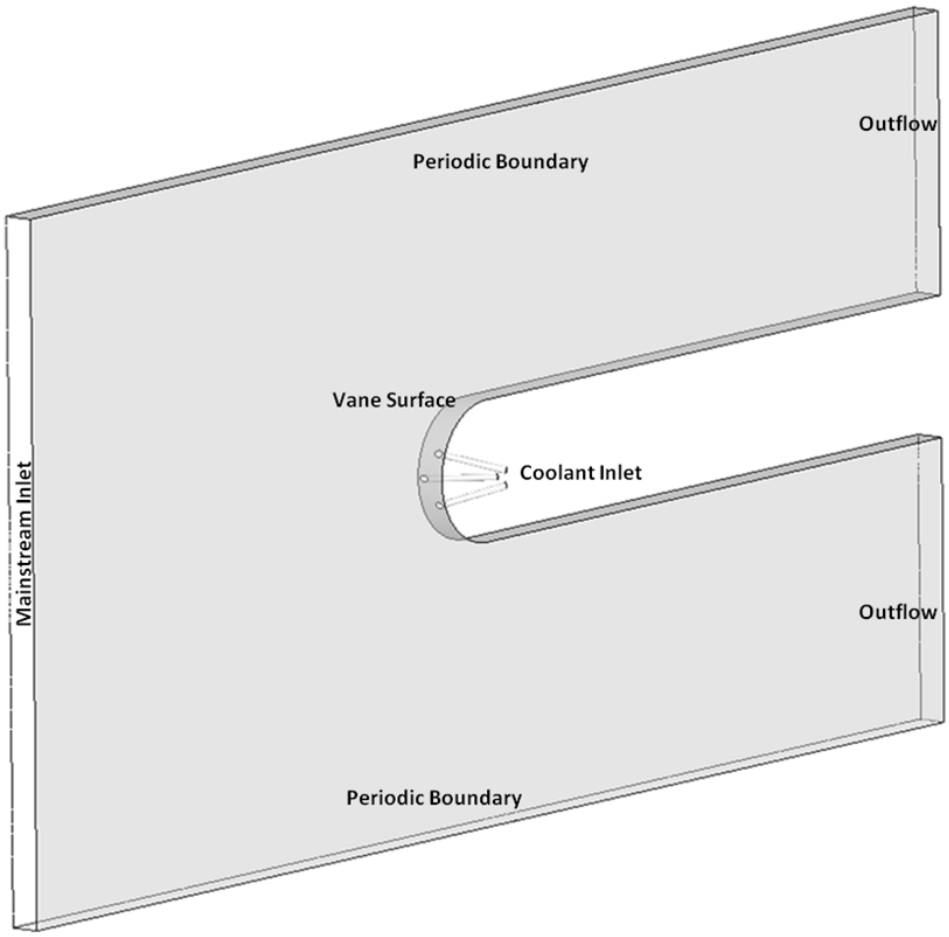

Figure B.1.: Computational domain of a leading edge vane modeled as a semi-cylinder with a flat after body

made of a structured mesh with unstructured block topology. To build the baseline grid, the Reynolds number based on coolant hole diameter and coolant inlet velocity is a decisive factor for the near wall resolution in the coolant pipe. The near wall resolution estimated in the coolant pipe is carried forward to the cylinder surface and flat after body. Based on these requirements, the baseline grid has a size of 11.38 million cells. Since the baseline grid selected for this geometry has the same high near wall resolution (7 points lie within $y^+ = 10$) as that used for LES studies no further grid independent study has been carried out for RANS calculations.

B.1.3 Boundary conditions

The adiabatic wall approach is used to predict the adiabatic wall temperature and effectiveness. Therefore, the surface is maintained at zero wall flux, the coolant temperature is set to 775K and the mainstream temperature is set to 1600K. Periodic boundary conditions are applied in the span (z-direction) to simulate an infinite row of holes. To simulate a linear cascade arrangement, periodic boundary conditions are also applied in the y-direction. No penetration and no slip conditions are applied on the vane surface and on the coolant pipe wall. The mainstream inlet condition has a constant velocity profile of 40m/s, turbulence intensity of 0.04% and viscosity ratio of 10. A convective outflow boundary condition is applied at the exit. The inlet boundary condition for the coolant pipe is also a constant velocity profile applied normal to the cross-section of the pipe. Turbulent intensity at the coolant inlet is set to 0.04% and the viscosity ratio is set to 5.

The particles (5 μm in size) are injected at the mainstream inlet of the leading edge extending the full lateral dimension of the computational domain and 0.35D on either side of the symmetry plane (or stagnation line). Hence the total coverage is 70% of the projected area of the leading edge. The coverage was not extended to the full projected area in order to make a one-to-one comparison with the deposition results that are obtained through LES calculations. A total number of 362,500 particles are injected at this location. Initially upon particle injection, the particle velocities and temperatures are set to the same as fluid velocity and temperature. Subsequently, the governing equations (refer §3.2) of motion of these particles are integrated using a trapezoidal scheme in the Lagrangian frame of reference to obtain the velocity and location.

In the present appendix, the free stream Reynolds number based on leading edge diameter and the free stream velocity is 32,000. The coolant to mainstream blowing ratio of 0.5, 1.0, 1.5 and 2.0, and a density ratio of 1 is studied.

B.1.4 Solver controls

The steady state RANS simulations, uses a commercial flow solver Ansys FLUENT. The carrier phase is computed using the shear stress transport (SST) $k-\omega$ turbulence model and the discrete phase is solved sequentially using the Lagrangian particle tracking algorithm. The turbulent dispersion of particles is modeled using stochastic tracking (Discrete Random Walk). All the results shown for RANS simulations are computed using an in-house TurboCFD cluster using 19 processors. For solver controls used for LES simulations, refer Chapter 3 §3.3.3.

B.2 Discussion of results

The purpose of this study is to investigate the particle deposition obtained using steady state RANS modeling of particle trajectory and report their comparison with deposition obtained from LES simulations. The particles that deposit on the leading edge vane surface are governed by the flow and temperature field generated by the coolant jet mainstream interaction. The momentum Stokes number governs the particle trajectory, whereas the response time for the particles to the changes in temperature within the flow field is regulated by the thermal Stokes number. The coolant jet mainstream mixing produces turbulent eddies which not only alter the particle trajectory but also change the particle temperature. This section first discusses the aero-thermal fields, followed by comparing RANS adiabatic effectiveness to LES simulations. Finally, particle deposition results are quantified and compared on the leading edge vane surface.

B.2.1 Mean temperature

Figure B.2 in streamwise (s/d slices) and figure B.3 in spanwise (z/d slices) show the mean temperature contours. Results obtained from the SST $k-\omega$ turbulence model (steady state RANS) are compared with the results obtained from LES simulations for B.R = 0.5 (figure B.2a) and B.R. = 2.0 (figure B.2b). The temperature

contour level shown here are non-dimensional (See page no. xvii). For B.R = 0.5, at streamwise slices s/d = 1 and s/d = 2, it can be seen that the coolant injected at the stagnation hole moves in the transverse direction approximately by half pitch (off-stagnation hole centerline). This is also evident in the spanwise mean temperature contours (figure B.3). As the blowing ratio is increased to 2, it can be seen that the stagnation jet moves laterally throughout the pitch. The coolant core spotted at s/d = 2, for the $SST\ k-\omega$ turbulence model, implies that the coolant jet dilution is under-predicted in this model when compared to LES simulations. The stagnation coolant jet forms a protective umbrella to protect the stagnation region similar to LES simulations nonetheless; the $SST\ k-\omega$ turbulence model over-predicts coolant penetration into the mainstream (figure B.3).

Next, just downstream of the off-stagnation coolant hole injection (s/d =5), for B.R. = 0.5, we can observe the crescent shaped coolant jet attached to the vane surface similar to that seen in LES simulations. The crescent shape is a visual representation of the asymmetric counter rotating vortex pair which entrains mainstream from the aft side of the coolant trajectory. This feature is a characteristic of the coolant jet geometry and angle of injection. As the blowing ratio increases to B.R. = 2.0, downstream of the off-stagnation coolant injection (s/d = 5), the coolant has moved half pitch from its injection location (s/d = 4) similar to that of LES simulations. Further downstream (s/d = 7.0) of the vane surface, even though the aft side vortex is entraining mainstream beneath the jet, the the $SST\ k-\omega$ turbulence model under-predicts turbulent mixing. In fact, the presence of coolant injected from the stagnation jet is still evident at s/d = 7.0 for the the $SST\ k-\omega$ turbulence model.

B.2.2 Turbulent kinetic energy

Figure B.4 show the mean T.K.E. contours (normalized by U_∞^2) in planes normal to the vane surface along the stream wise direction for B.R. = 0.5 and B.R. =2.0. T.K.E. level is a good indicator of the turbulent mixing between coolant and mainstream. T.K.E is produced by the shear interaction between the coolant jet and the

mainstream as the jet penetrates into the flow and also by the strong shear induced underneath the coolant jet in the near wall region due to entrainment [2, 3].

As the blowing ratio increases, the T.K.E. also increases. Concurrent with the temperature contours the $SST\ k-\omega$ turbulence model under-predicts turbulent mixing. Figure B.5 shows the T.K.E. profile for B.R. = 0.5 along the off-stagnation hole centerline. T.K.E. values of magnitude 0.03 are observed in the bulk of the stagnation jet as it interacts with the mainstream by the $SST\ k-\omega$ turbulence model compared to a magnitude of 0.06 from LES simulation. As the bulk of the stagnation jet convects downstream there is a drop in the maximum T.K.E. to approximately 0.02, before it is replenished by coolant injection at s/d=4. The crescent shaped region (figure B.4) of high T.K.E. is a consequence of the shear interaction between the coolant boundaries and the mainstream. In the T.K.E. profile at s/d = 5, the $SST\ k-\omega$ turbulence model does not predict any turbulence in the near wall region. The T.K.E. magnitude obtained from the $SST\ k-\omega$ turbulence model, downstream of the off-stagnation injection is less (0.01) and does not diffuse as quick as that seen in LES simulations, in the bulk of the coolant flow as the jet convects further downstream.

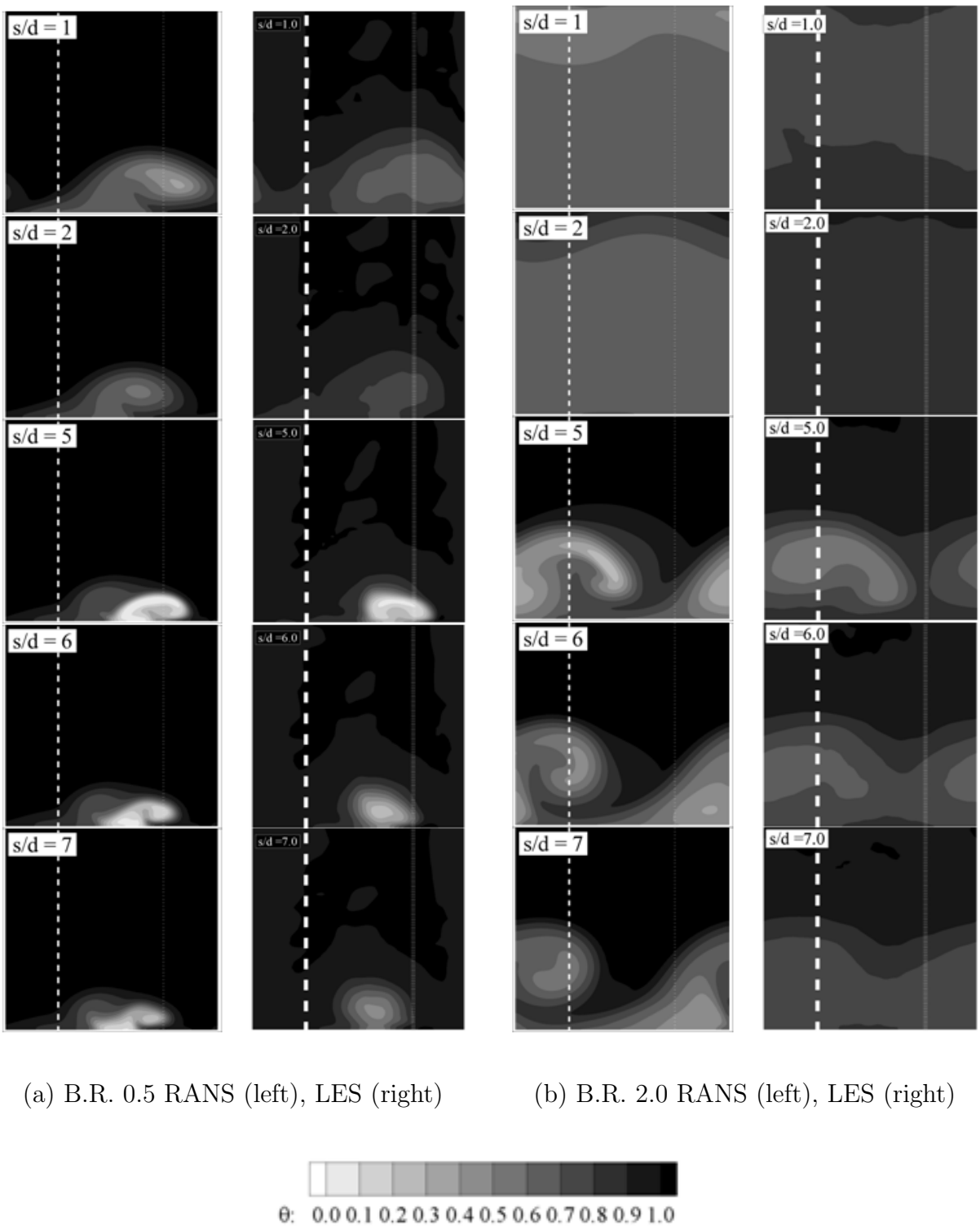

(a) B.R. 0.5 RANS (left), LES (right)

(b) B.R. 2.0 RANS (left), LES (right)

Figure B.2.: Time-averaged temperature contours in streamwise direction. Coolant injection is from right to left. Height of domain is 4.28d. Dash line is centerline of stagnation hole (z/d=-1.125); faint dotted line is centerline of off-stagnation hole (z/d=1.125).

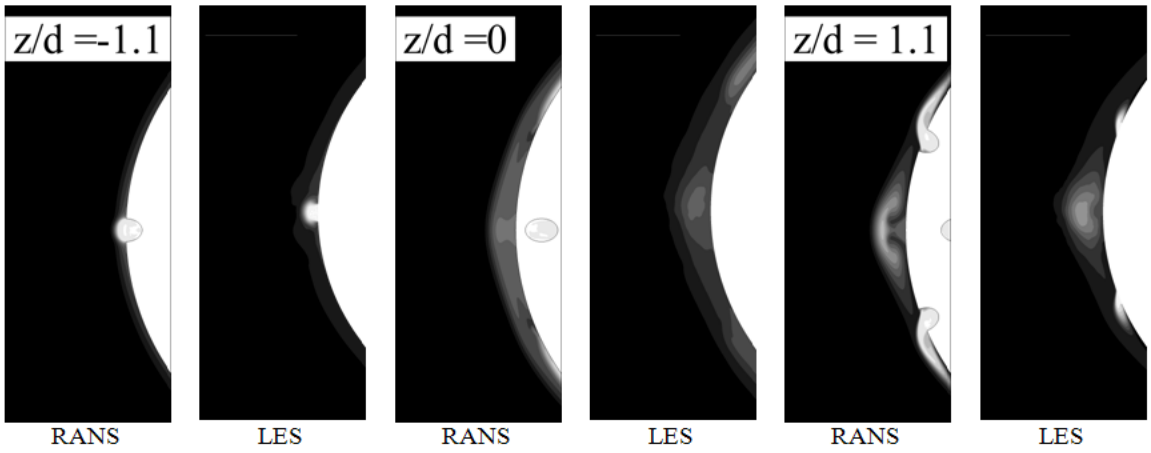

(a) B.R. 0.5

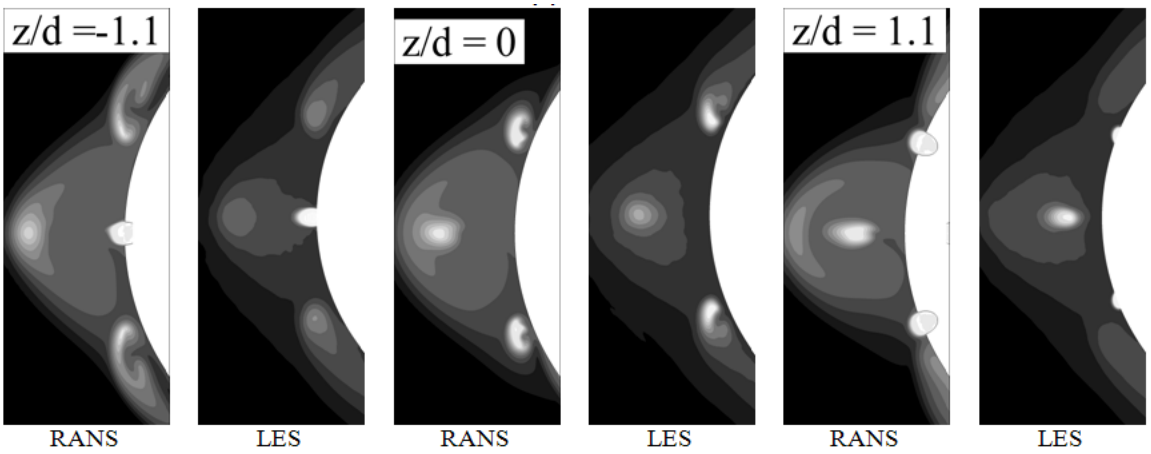

(b) B.R. 2.0

Figure B.3.: Time-averaged temperature contours at different lateral planes. Stagnation hole centerline is at z/d=-1.125 and off-stagnation hole centerline is at z/d=1.125.

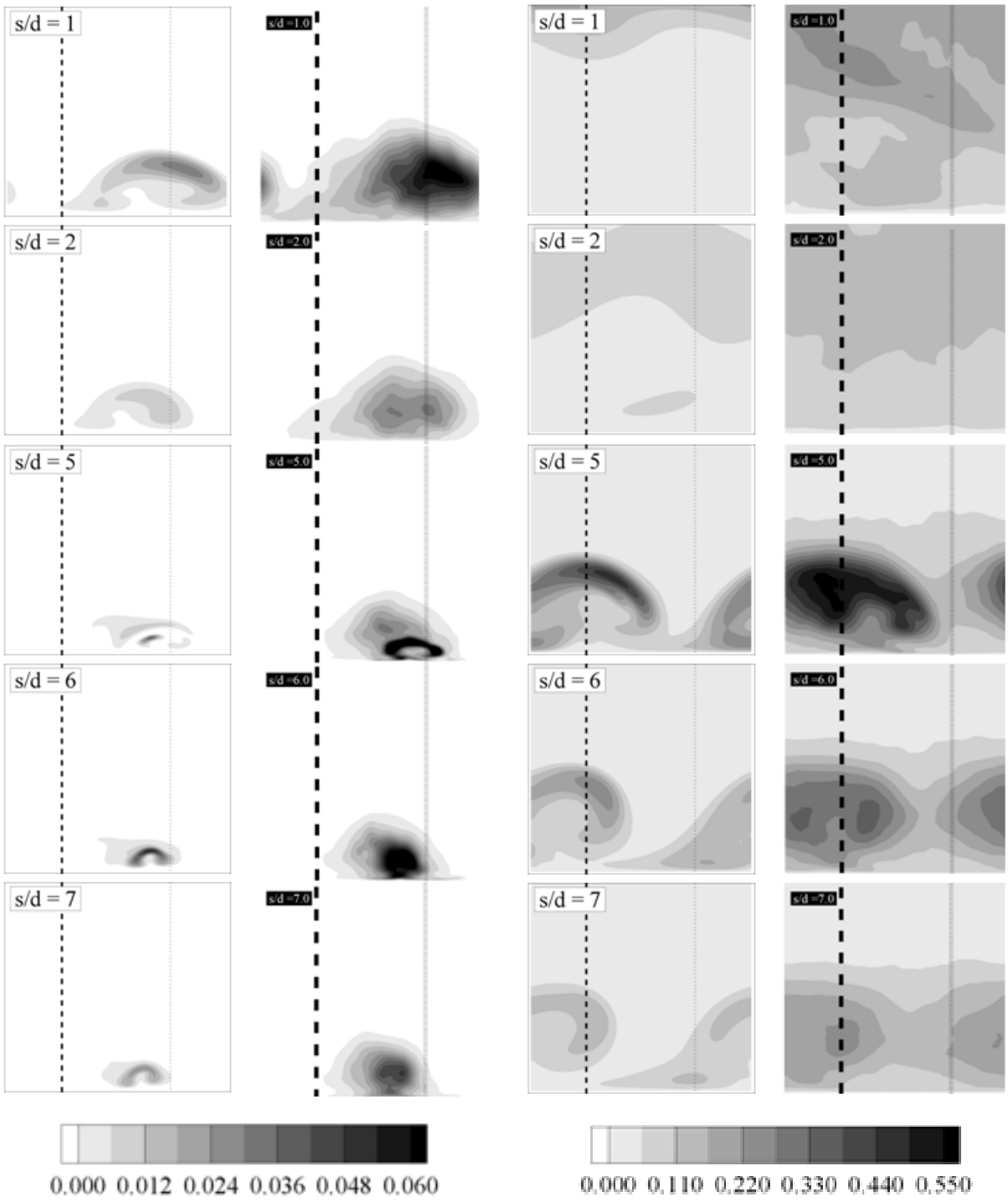

(a) B.R. 0.5 RANS (left), LES (right)

(b) B.R. 2.0 RANS (left), LES (right)

Figure B.4.: T.K.E. contours along the stream wise direction. Coolant injection is from right to left. Height of domain is 4.28d. Dash line is centerline of stagnation hole (z/d=-1.125); dotted line is centerline of off-stagnation hole (z/d=1.125).

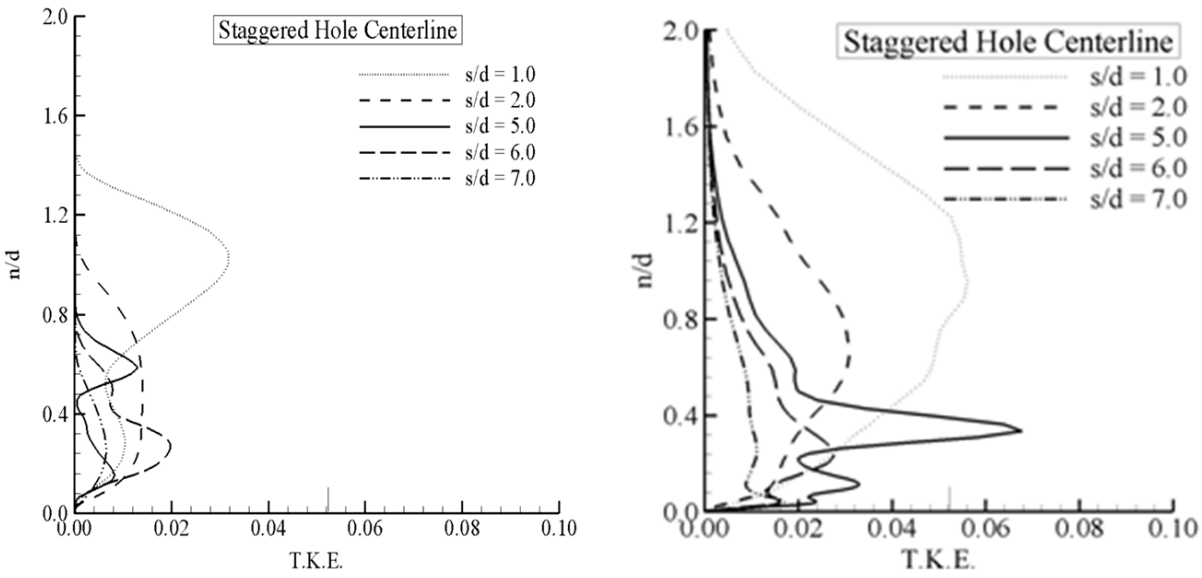

(a) RANS (b) LES

Figure B.5.: T.K.E. profiles along the streamwise direction for B.R. = 0.5

B.2.3 Adiabatic effectiveness

Figure B.6 compares the contours of adiabatic effectiveness that is achieved by the film cooling on the vane surface to protect the vane surface from the hot mainstream at blowing ratios of 0.5 and 2.0. Figure B.7 shows the line plots of spanwise laterally averaged adiabatic effectiveness along the downstream location (s/d) for RANS and LES simulations. The spanwise average is found by averaging across the upper and lower halves of the geometry. The surface adiabatic effectiveness in the stagnation region is a function of the jet penetration and mixing and the amount of coolant injected. The behavior of the adiabatic effectiveness reported by the $SST\ k-\omega$ turbulence model follows a similar trend to that obtained by LES calculations at all blowing ratios. Nonetheless, adiabatic effectiveness is over-predicted by the $SST\ k-\omega$ turbulence model. This is attributed to the under-prediction of jet dilution or turbulent mixing by the RANS based model (low T.K.E values).

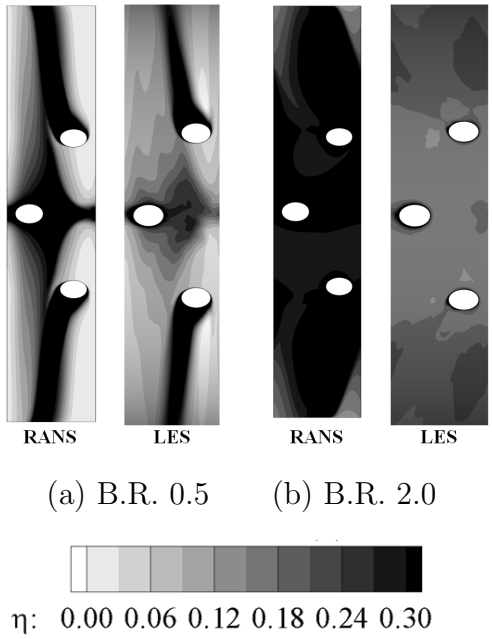

(a) B.R. 0.5 (b) B.R. 2.0

Figure B.6.: Contours of Adiabatic effectiveness

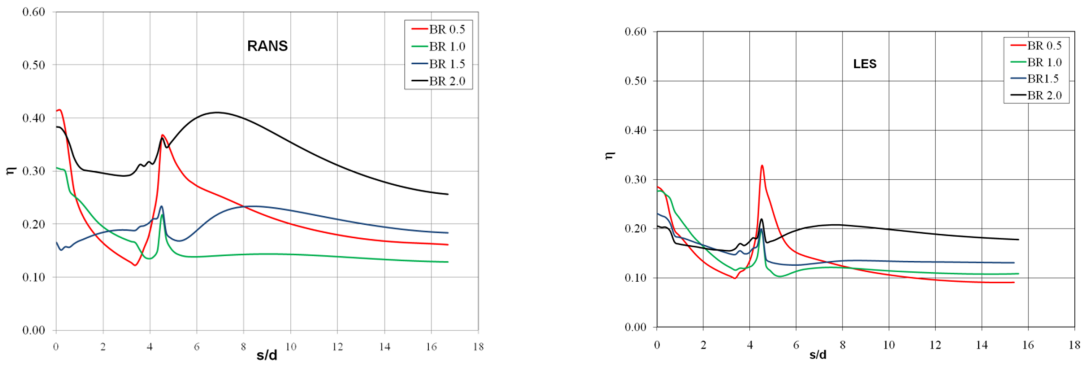

(a) RANS (b) LES

Figure B.7.: Spanwise laterally averaged adiabatic effectiveness along the streamwise direction

B.2.4 Deposition

Deposition on the vane surface is influenced by whether the coolant jets are successful in blowing the particles away from the surface or whether the particles approaching the surface are cooled to a solid phase. In the present appendix, the deposition model uses the sticking probability model based on critical viscosity of the flyash particles as the criterion for deposition (refer Chapter 4). Particle size considered for this study is 5 μm in diameter.

To give a realistic estimate of deposition, the dispersion of flyash particles caused due to the presence of turbulence is modeled using a stochastic approach (Discrete Random Walk Model) in the RANS based solver. The purpose of using this model is to account for local variations in the flow field that will alter particle trajectories in an effort to simulate unsteady particle trajectories using the mean flow field. This instantaneous velocity field is obtained as a product of a normalized random number and u_{rms} from the calculated turbulent kinetic energy. The fluctuating velocity estimated from T.K.E. assumes isotropic turbulence.

Figure B.8 shows the capture efficiency predicted by the RANS simulations compared to the capture efficiency predicted from LES calculations for 3 blowing ratios. In this figure, only 2 representative ash samples are compared: namely ND ash sample and the ExBC ash sample used by Crosby et al. [1] (Table 4.1). The modified deposition model is explained in section §4.3 and the old model is explained in section §3.3. As expected the modified deposition model accounts for deposition below the softening temperature in addition to the deposition occurring above the softening temperature (old model: T_{soft} = 1500K). For all the 3 blowing ratios, the ND ash sample exhibits the highest capture efficiency. This feature is due to differences in viscosity variations for the 2 samples. For LES simulations (figure B.8a), deposition increases at B.R. = 2.0, this is due to increased levels of mainstream entrainment. Figure B.8b shows ash deposition predicted by RANS simulations. As noted in the previous section, the coolant jets are coherent and indicate little jet dilution (figure

B.2), thus resulting in higher effectiveness of vane surface. Lower surface temperature (figure B.6) and increased jet penetration predicted by RANS simulations results in increased particle residence time in cooler surroundings. Additionally, the discrete random walk model implemented in this complex geometry adds little effect in simulating the particle trajectory close to the vane surface. This can partly be due to isotropic turbulence assumption in the discrete random walk model. Hence, whatever number of particles impact the surface are cooled much below their softening temperature and possess a low sticking probability. In summary, LES performs well when predicting ash deposition on the leading edge vane surface compared to RANS simulations.

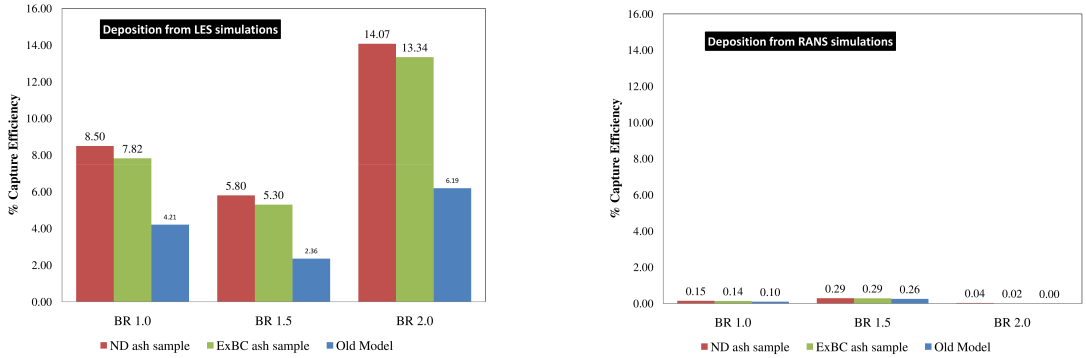

(a) (b)

Figure B.8.: Percentage capture efficiency of ash particles on the vane surface from (a) LES simulations (b) Discrete Random Walk model in RANS simulations

B.3 Summary and conclusions

Computational studies have been carried out on a 3-row film cooled leading edge region representative of a turbine vane to investigate ash deposition for particle sizes of 5 μm. The simulations for steady state RANS use the SST $k-\omega$ turbulence model and are compared against results obtained from LES. Particle trajectories are tracked in a

Lagrangian frame of reference. Qualitatively, the $SST\ k{-}\omega$ turbulence model predicts somewhat similar flow field features in comparison to LES. However, the $SST\ k-\omega$ turbulence model estimates low values of turbulent kinetic energy which indicates less amount of jet dilution. The inaccuracies in estimating turbulent mixing of jets by the $SST\ k-\omega$ turbulence model, results in the over-prediction of jet penetration and under-prediction of jet mixing. This results in higher adiabatic effectiveness on the vane surface compared to LES calculations. Deposition results shown in this appendix employs the deposition model that uses sticking probability based on the critical viscosity approach as a criterion for deposition. Results have quantified the effect of accounting deposition for particles that are below their softening temperature for 2 ash samples. The modified deposition model for ND ash sample predicts the capture efficiency of the particles twice as much as its precursor. In the RANS based solver, the turbulence dispersion of particles is modeled using a Discrete Random Walk (DRW) model. Results from the DRW model show trivial effects on particle trajectory close to the vane surface. Only a small fraction of the particles injected, actually impact the surface ($\sim$0.4%) and since RANS over-predicts the adiabatic effectiveness whichever particles reach the surface have a very low sticking probability resulting in very little or no deposition.

B.4 Bibliography

[1] Crosby, J. M., Lewis, S., Bons, J. P., Weiguo, A., and Fletcher, T., 2007. "Effects of partilce size, gas temperature, and metal temperature on high pressure turbine deposition in land based gas turbines from various synfuels". *ASME Paper No. GT2007-27531.*

[2] Rozati, A., and Tafti, D., 2008. "Large-eddy simulation of leading edge film cooling: Analysis of flow structures, effectiveness, and heat transfer coefficient". *International Journal of Heat and Fluid Flow,* ***29***(1), pp. 1–17.

[3] Rozati, A., and Tafti, D., 2008. "Effect of coolant mainstream blowing ratio on leading edge film cooling flow and heat transfer - les". *International Journal of Heat and Fluid Flow,* ***29***(1), pp. 857–873.

APPENDIX C. DEPOSITION MODEL ALGORITHM

Our previous deposition model involved calculation of capture efficiency at run-time. The modified deposition model, now works like a post-processing tool where the capture efficiency is calculated after the simulation is completed. The particle wall collision data recorded at run-time from the solver is saved to a file, which is input to the deposition model. The particle wall collision data includes particle information like impact temperature, velocity and angle. The benefit in applying the deposition model as a post processing tool is that the capture efficiency for various ash compositions [Table 4.1] can be computed easily with the available particle wall collision data. In general, to run a simulation for one ash composition, it takes about 2 3 weeks on System X cluster at Virginia Tech using the previous model. Whereas, using this modified deposition model one can predict capture efficiency for many coal ash composition in just 2 3 weeks, adding more flexibility to the model. The algorithm for the modified deposition model is shown in Figure C.1. Equation (4.1) in the computational model framework is defined as the actual sticking probability of the particle. In order to implement this formulation, a uniform random number generator is used to generate random sticking probabilities for each particle collision. If the random sticking probability of the particle is less than the actual sticking probability then the particle is assumed to deposit. In order to use this approach, the particle sample size must be large enough for the capture efficiency to asymptote to the actual sticking probability.

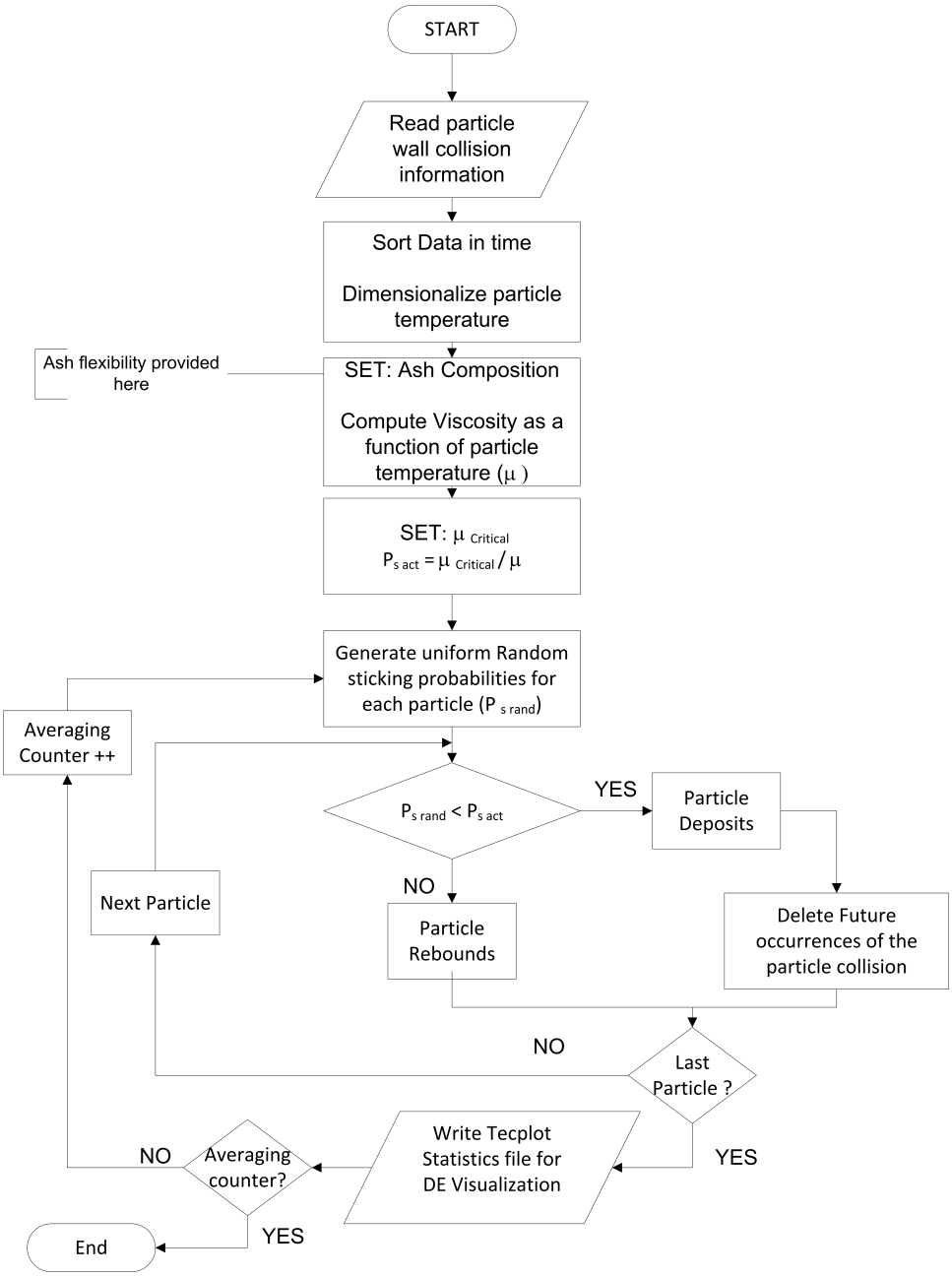

Figure C.1.: Flow chart for deposition model implementation in GenIDLEST

APPENDIX D. EROSION STUDIES

Abstract

A numerical study is performed to investigate erosion of Syngas ash in the leading edge region of a turbine vane. The leading edge of the vane is modeled as a symmetric semi-cylinder with a flat after body. Three rows of coolant holes located at stagnation and at $\pm 21.3^{\circ}$ from stagnation are simulated at blowing ratios of 0.5,1.0,1.5 and 2.0. Large Eddy Simulation (LES) is used to model the flow field of the coolant jet-mainstream interaction and Syngas ash particles are modeled using a Lagrangian framework. Ash particle sizes of 5 and 7 micron are considered. Under the conditions of the current simulations, both ash particles have Stokes numbers less than unity of O(1) and hence are strongly affected by the flow and thermal field generated by the coolant interaction with the mainstream. Because of this, the stagnation coolant jets are quite successful in pushing the particles away from the surface and minimizing erosion in the stagnation region. Overall, erosive ash particles of 5 μm size increase from 4% of the total to 7% as the blowing ratio increases from 0.5 to 2.0, whereas 7 μm erosive particles remain nearly constant at 10%.

D.1 Introduction

Syngas produced from coal gasification, despite gas cleanup procedures, contains traces of flyash particles ($1\mu m$-$10\mu m$, [1–3]). The residual ash particles achieve a molten state in the gas turbine combustor and are carried through to the hot gas flow path. The first stage vanes are the most susceptible to damage in the form of deposition and erosion. Solid ash particles can degrade the thermal barrier coating [4] by erosion and contribute to spallation of the coating. Knowledge of the mechanisms

A part of this work is published in IGTI ASME paper # GT09-59326

responsible for erosion and methods of mitigation can help improve the operational life of the turbine components and reduce the risk of catastrophic failures.

Impaction of particulate matter (mostly ash) has received attention in past studies which have focused on the effect of particle size on impaction of the first stage stator and rotor. The trajectory of particles is governed by the action of different forces due to aerodynamic drag, lift, gravity, unsteady motion, pressure gradients, turbulent eddies, Brownian impaction of molecules, and at large temperature gradients, that of thermophoresis. Random Brownian motion is caused by bombardment of fluid molecules on the particle and thermophoretic effects are brought about by large temperature gradients. Although in most situations the drag force is dominant, other forces can dominate under certain conditions.

Erosion of turbine blades has been extensively studied in the literature [5]. Erosion, or erosive wear, is the loss of material from a solid surface due to the impact of the solid particles in the gas-solid mixture on the turbine blade. Erosion is affected by various parameters - the composition, size, and shape of the eroding particles, their velocity and angle of impact, and the composition and microstructure of the surface being eroded. Though the erosion of a given material is a function of time, most of the models focus on the steady state erosion. The impact of the particles on blades leads to elastic or plastic deformation or fracture (erosion), depending on the impact characteristics and the material properties. However the magnitude and direction of the rebound velocities give a good estimate of the kinetic energy transferred to the blade upon impact. The larger the ratio of the rebound velocity to the impact velocity (restitution coefficient), the lesser is the erosion. Finnie [6] investigated the wear mechanisms on ductile and brittle surfaces. His investigation concluded that the flow field and the vane surface properties influence the amount of erosion of the surface. One point of emphasis in this study is that the surface that is coarsened by erosion may possibly enhance turbulence and further intensify the rate of erosion. Tabakoff [2] described an experimental technique to evaluate parameters that characterize particle erosion in gas turbine components. He investigated flyash

particles sized 15 μm and sand particles sized 160 μm. A semi-empirical relation to measure the erosion rate was developed. Erosion rate depends on yield strength of the surface, which is a function of temperature, particle impact velocity, impact angles and restitution ratios. Metwally et. al. [7] used a blade material erosion model that depends on particle trajectory, which is a function of flow field. A recent study by Tabakoff [8] reported that platinum aluminide coating on stainless steel material provided superior resistance from erosion due to flyash particles at high temperatures. Siravuri et al. [9] evaluated particle rebound characteristics at the leading edge of a blade by using silica sand particles sizes between 1000 to 1500 μm and stainless steel as the target material. They found that impact was highest (largest erosion damage) at the leading edge, which subsequently decreased further downstream.

Recent work on deposition and erosion in turbomachines is summarized in a review paper by Hamed et al. [10]. The review includes an extensive pool of studies on erosion conducted experimentally and numerically. The experiments found the amount of erosion to be a function of particle size, mainstream temperature and the amount of turbulence produced by the film cooling jet. Likewise, deposition was a function of particle inertia and temperature. There have been few numerical studies of erosion. Hamed et. al. [11] included experimental and numerical investigation on erosion in gas turbine vanes. Their computations used Fluent with a RNG $k-\epsilon$ turbulence model to compute the flow field with Lagrangian particle dynamics. They reported high erosion rates in the leading edge of the vane. Shah and Tafti [12] also used Lagrangian particle dynamics to compute the erosion in a ribbed internal cooling duct. The turbulence in the flow field is resolved using the LES technique that provided a firm theoretical basis for modeling particle trajectories. Results presented particle impingement locations, impact velocity, impact angles for sand particles sizes of 10 μm, 50 μm and 100 μm.

The leading edge of the first stage nozzle guide vane is one of the most vulnerable sections to deposition and erosion. While most past studies have focused on particle impaction in the first stage stator and rotor, the objective of this paper is to investigate

the dynamics of ash deposition and erosion in a leading edge vane geometry with film cooling. LES is used for resolving the turbulent interaction between film cooling jets and the mainstream flow with Lagrangian particle dynamics to simulate the ash particles. This follows an earlier study [13] which investigated film-cooled geometry with two rows of holes on either side of stagnation. It was established that the particles with Stokes numbers much less than unity did not pose a serious threat to erosion, whereas particles at higher Stokes numbers (>1) impacted the surface by virtue of their inertia and jet blowing ratios (up to 1.2) did have not have a substantial impact on their trajectories. Particles with Stokes number of O(1) were found to be the most amenable to manipulation by the coolant jets. The current study is an extension of [13] but for a more realistic three-row cooling geometry at the leading edge and for coolant blowing ratios ranging from 0.5 to 2.0. Two ash particle sizes of 5 μm and 7 μm are investigated.

D.2 Computational model

D.2.1 Geometry description

The computational domain models the leading edge of a vane as a semi-cylindrical form with a flat after body. Three rows of film cooling holes are employed. One row is located at stagnation and two rows are located at ±4d, on either side of the stagnation line. The lateral pitch spacing (P) between two holes for any given row is 4.5d, and the relative position of the holes on the upper half and lower half are staggered with respect to the stagnation hole. The origin is fixed at the center of the domain at stagnation with the stagnation hole located at z = -1.125d and staggered off-stagnation holes located at z = 1.125d. The coolant hole diameter ratio (D/d) is 21.5 and the length ratio of the coolant pipe (L/d) is 10.75 . The coolant is injected laterally at 45° to the surface with a compound angle of 90° to the mainstream. Figure D.1 shows the head-on view of the leading edge model. The dotted line shows the computational domain. Figure D.2 shows the computational domain of interest

as the shaded region. It extends 10D in the x-direction, 5D in y-direction and 4.5d in the spanwise z-direction.

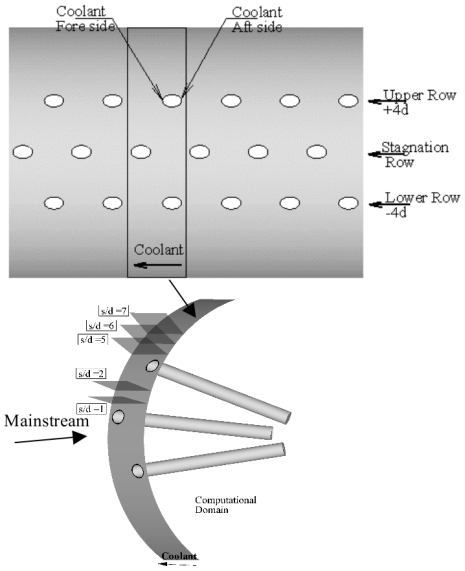

Figure D.1.: Leading edge vane model and near field streamwise planes used in presenting results.

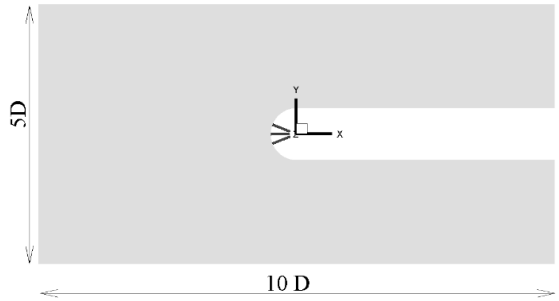

Figure D.2.: Computational domain in side view (X-Y plane)

The flow conditions and the particle properties used to compute the Stokes number are tabulated in [Table D.1] . The Stokes number signifies the time that a particle takes to respond to a local change in the fluid velocity (momentum Stokes number) or fluid temperature (thermal Stokes number). A Stokes number much less than 1 indicates that the particle responds to the changes in the fluid surrounding

Computations assumes a coolant to mainstream density ratio of 1 (Table D.1)

Table D.1: Leading edge geometry and flow properties

Leading Edge Geometry	
Blade leading edge diameter (D^*) $[m]$	0.01
Coolant jet diameter (d^*) $[m]$	4.65×10^{-4}
Span-wise pitch (p^*/d^*)	4.5
Flow Properties	
Free stream velocity (U^*_∞), $[m/s]$	40
Free stream temperature (T^*_∞), $[K]$	1600
Free stream pressure (P^*_∞), $[atm]$	20
Free stream density (ρ^*_∞), $[kg/m^3]$	4.4
Particle density (ρ^*_p), $[kg/m^3]$	2500
Particle Specific heat (c^*_p), $[J/kgK]$	250
Coolant temperature (T^*_j), $[K]$	775
Ash softening Temperature, $[K]$	1500
Coolant-to-mainstream density ratio	2.071
Coolant-to-mainstream blowing ratio (U^*_j/U^*_∞)	0.5, 1.0, 1.5, 2.0

Table D.2: Particle Stokes number

d^*_p (μm)	St_p	St_{conv}	St_{rad}
5	0.25	0.0578	2.24
7	0.49	0.113	3.14

it almost instantaneously. And a Stokes number greater than 1 indicates that the particle takes a long time to adjust to changes in surrounding fluid. The momentum

and the thermal Stokes number for the particle sizes considered in this study are tabulated in Table D.2.

D.2.2 Boundary conditions

The adiabatic wall approach is used to predict the adiabatic wall temperature and effectiveness. Therefore, the surface is maintained at zero wall flux, the non-dimensional coolant temperature is set to 0 and the non-dimensional mainstream temperature is set to 1. Periodic boundary conditions are applied in the span (z-direction) to simulate an infinite row of holes. To simulate a linear cascade arrangement, periodic boundary conditions are also applied in the y-direction (figure D.2). No penetration and no slip conditions are applied on the vane surface and on the coolant pipe wall. The mainstream inlet condition is a constant velocity profile with no turbulence intensity and a convective outflow boundary condition is applied at the exit. The inlet boundary condition for the coolant pipe is also a constant velocity profile applied normal to the cross-section of the pipe.

The particles are injected 0.36D upstream of the leading edge extending the full lateral dimension of the computational domain and 0.35D on either side of the symmetry plane (or stagnation line). Hence the total coverage is 70% of the projected area of the leading edge. The coverage was not extended to the full projected area because trial runs showed that particles injected outside of the 0.7D envelope did not interact with the vane surface but simply flowed around the leading edge as the flow diverged on approach to the leading edge. A total number of 362,500 particles are injected at this location. Initially upon particle injection, the particle velocities and temperatures are set to the same as fluid velocity and temperature. Subsequently, the governing equations of motion of these particles are integrated using a third order Adams-Bashforth method in the Lagrangian frame of reference to obtain the velocity, location, and temperature. Molten particles in the free-stream at T=1600K deposit on the vane surface if their temperature is above the ash softening temperature of

1500K. If the particles are cooled below the softening temperature they are assumed to be solid and behave as erosive particles.

In the present study, the free stream Reynolds number based on leading edge diameter and the free stream velocity is 32,000. The effect of coolant to mainstream blowing ratio of 0.5, 1.0, 1.5 and 2.0, on ash particle sizes of 5 μm and 7 μm is investigated.

D.3 Discussion of results

The flow and temperature field generated by the coolant jet and mainstream interaction are crucial to the aero-thermal behavior of particles and whether they deposit or erode the surface. The aerodynamics of jet-mainstream interaction can either push the particle away from the vane surface or entrain the particle near the surface. In the same manner, the thermal field generated by the jet-mainstream interaction influences the temperature of the particle. The momentum Stokes number governs the particle trajectory, whereas the response time for the particles to the changes in temperature within the flow field is regulated by the thermal Stokes number. The coolant jet mainstream mixing produces turbulent eddies which not only alter the particle trajectory but also change the particle temperature. If the thermal Stokes number is small, any interaction of the particle with the coolant jet will lower its temperature below the softening temperature.

D.3.1 Flow and thermal field

To get an insight of the coolant jet mainstream mixing, instantaneous coherent structures of turbulence are shown. Figure D.3 shows the iso-vorticity coherent turbulent structures for coolant to mainstream blowing ratio of 0.5 and 2.0. These structures are extracted by using the vortex eduction procedure by Chong et al. [14]. The magnitude (iso-vorticity value, Figure D.3) of the iso-vorticities represent the strength of the vortices. At low blowing ratio (B.R. = 0.5), the vortical coherent

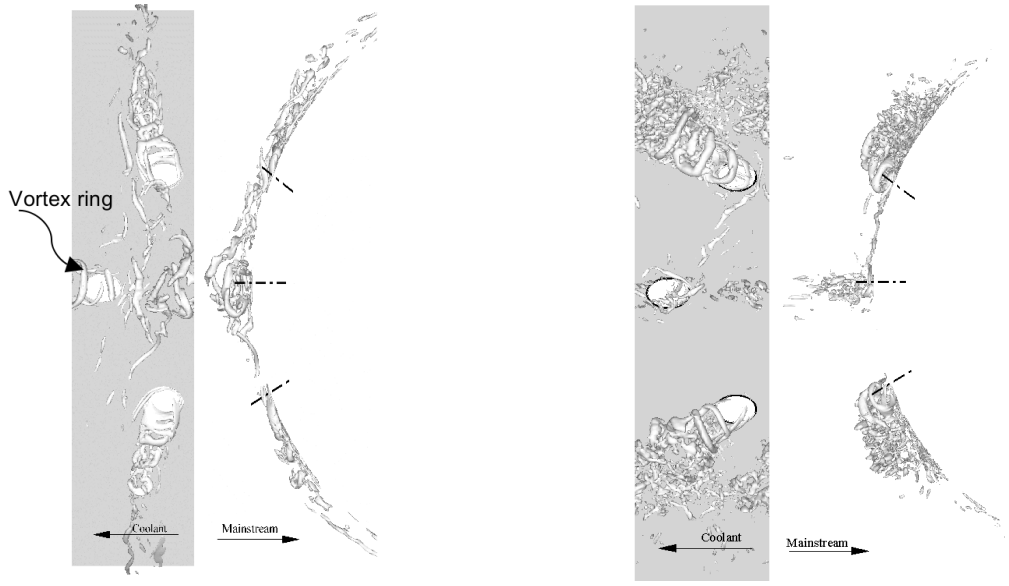

(a) Front View Side View (b) Front View Side View

Figure D.3.: Structure of coherent vorticity (a) B.R. 0.5 (Iso-surface value = 30) (b) B.R. 2.0. (Iso-surface value = 75)

structures are well defined. A ring vortex generated at the stagnation jet convects along the stagnation line which then destabilizes and moves downstream of the vane surface under the influence of the accelerating mainstream flow. The vortex generated by the off-stagnation holes quickly aligns to the vane surface and protection extends to a fraction of the pitch. This occurrence is again caused by the influence of accelerating mainstream flow. As the blowing ratio is increased (B.R. = 2.0), the coolant jet penetrates further into the mainstream and is diluted by turbulent diffusion. At this high blowing ratio, the little coherence that is seen in figure D.3a, disintegrates to form small scale vortical structures.

Figure D.4 shows the contours of adiabatic effectiveness that is achieved by the film cooling on the vane surface to protect the vane surface from high temperatures at different coolant to mainstream blowing ratio. Figure D.5 shows the line plots of laterally averaged adiabatic effectiveness along the span of the vane surface as a

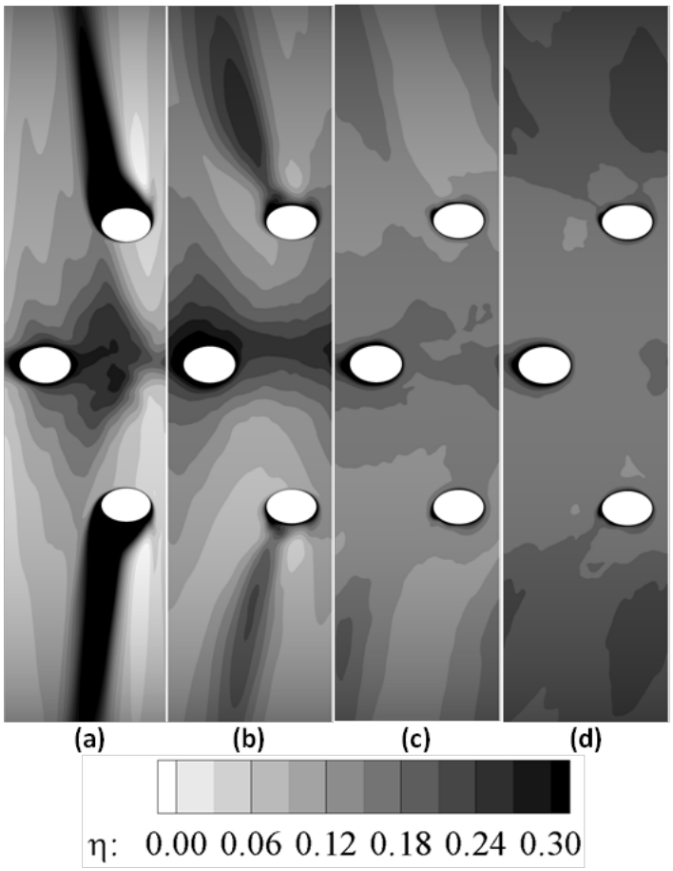

Figure D.4.: Effectiveness on the vane surface (a) B.R. 0.5 (b) B.R. 1.0 (c) B.R. 1.5 (d) B.R. 2.0

function of downstream location (s/d). The spanwise average is found by averaging across the upper and lower halves of the geometry. The surface adiabatic effectiveness in the stagnation region is a function of the jet penetration and mixing and the amount of coolant injected. At B.R.=0.5, jet penetration into the mainstream is the smallest amongst the different blowing ratios resulting in the least amount of mixing. Hence it has the largest effectiveness at the stagnation line. However, because of the larger injected mass at B.R.=1.0 and the redirection of the coolant to the vane surface, the adiabatic effectiveness downstream of the stagnation line is higher than B.R.=0.5. As the blowing ratio increases further to 1.5 and 2.0, the effectiveness decreases in the immediate vicinity of the stagnation line as the jet penetrates further into the mainstream but increases downstream of stagnation.

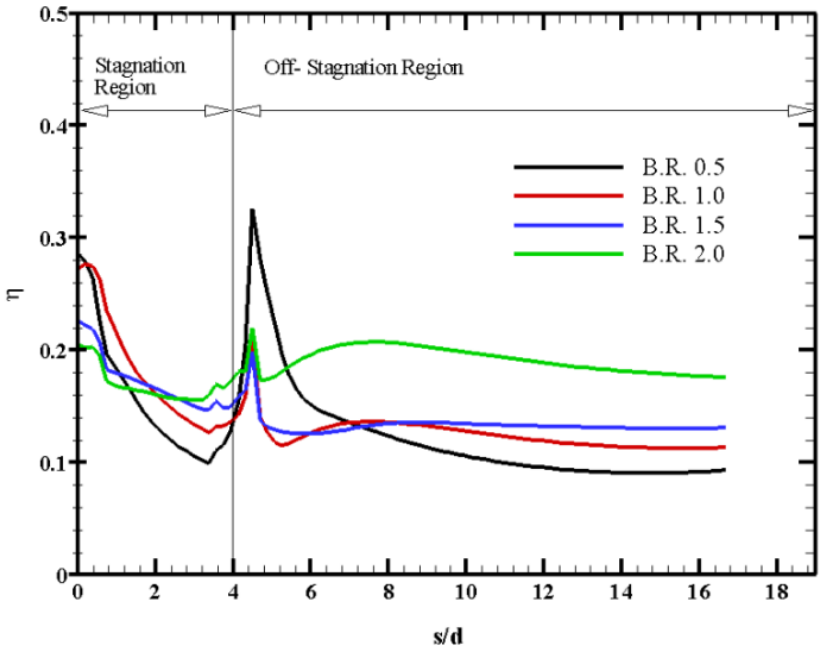

Figure D.5.: Lateral span averaged effectiveness on the vane surface.

The behavior of the adiabatic effectiveness follows the same principles downstream of the second row of injection. There is a fine balance between injected coolant mass and jet penetration and mixing. At the lowest blowing ratio of 0.5, the injected coolant remains close to the surface and provides the highest effectiveness immediately downstream of injection. However the effectiveness decays rapidly, as a result of the smaller mass of coolant and lower lateral spreading of the coolant. As the blowing ratio increases to 1.0, the larger initial penetration of the jet into the mainstream reduces the effectiveness immediately downstream of injection, but which increases as the coolant is pushed back to the surface. At B.R.=1.5, the penetration into the mainstream is larger but because of the larger coolant mass, the redirection of coolant back to the surface dominates downstream and increases the effectiveness. Similar to B.R.=1.5, at B.R.=2.0, in spite of the high T.K.E. generated and the intense mixing between the jet and the mainstream, the larger coolant mass injected and the larger lateral spread of the jet dominates the adiabatic effectiveness at the surface.

D.3.2 Erosion

Erosion is the amount of material removed due to impaction of abrasive flyash particles. The particles that impact the surface of the vane and have their temperature less than the softening temperature are said to be in solid state and have the potential to erode the surface. This section of the study does not characterize the extent of actual erosion but instead quantifies the fraction of particles that could be erosive, impact velocity, impact angles and the fraction of incoming particle kinetic energy that could potentially be imparted to the vane surface. These data along with material properties can be used to compute the actual net erosion rate [1, 15].

Particles that participate in erosive wear are assumed to be in the solid state or above the softening temperature in the current model. This implies that the particles on their way to the surface have had sufficient residence time in the coolant to be cooled below the softening temperature. Hence erosive particles are mostly found in the coolant path. When an erosive particle strikes the surface it is modeled as an ideal elastic collision with restitution coefficient of unity. Figure D.6 shows the distribution of the percentage of total particles which are erosive. At B.R.=0.5, the coolant core stays attached to the vane surface at the stagnation row as well as the off-stagnation rows. The lateral penetration of the stagnation row jet and the formation of ring vortices, their subsequent breakdown and the convection of vortex streams downstream of stagnation influence the distribution of erosive 5 and 7 μm particles. There is a clear correlation between the coherent structures in figure D.3(a) at B.R.=0.5 and the erosive pattern in figure D.6. A smaller fraction of the 5 μm particles are entrained by the coolant jet because of their tendency to follow the outer flow around the stagnation line (small St_p), whereas more 7 μm particles are entrained into the coolant jet, cool down and hit the surface. Further evidence to the entrainment of the particles in the coolant jet at stagnation versus direct inertial impaction can be obtained from figure D.7 which shows the distribution of impact velocity on the surface just before the particle collides with the surface, and figure

D.8 which shows the angle of impact. The low angles of impact in the stagnation region testify that the particles do not undergo a head on collision with the surface but rather at a very shallow angle which is more in line with the entrainment of particles into the vortex structures produced by the jet-mainstream interaction. The low velocities of impact in the stagnation region signify that potential erosive damage is not very high.

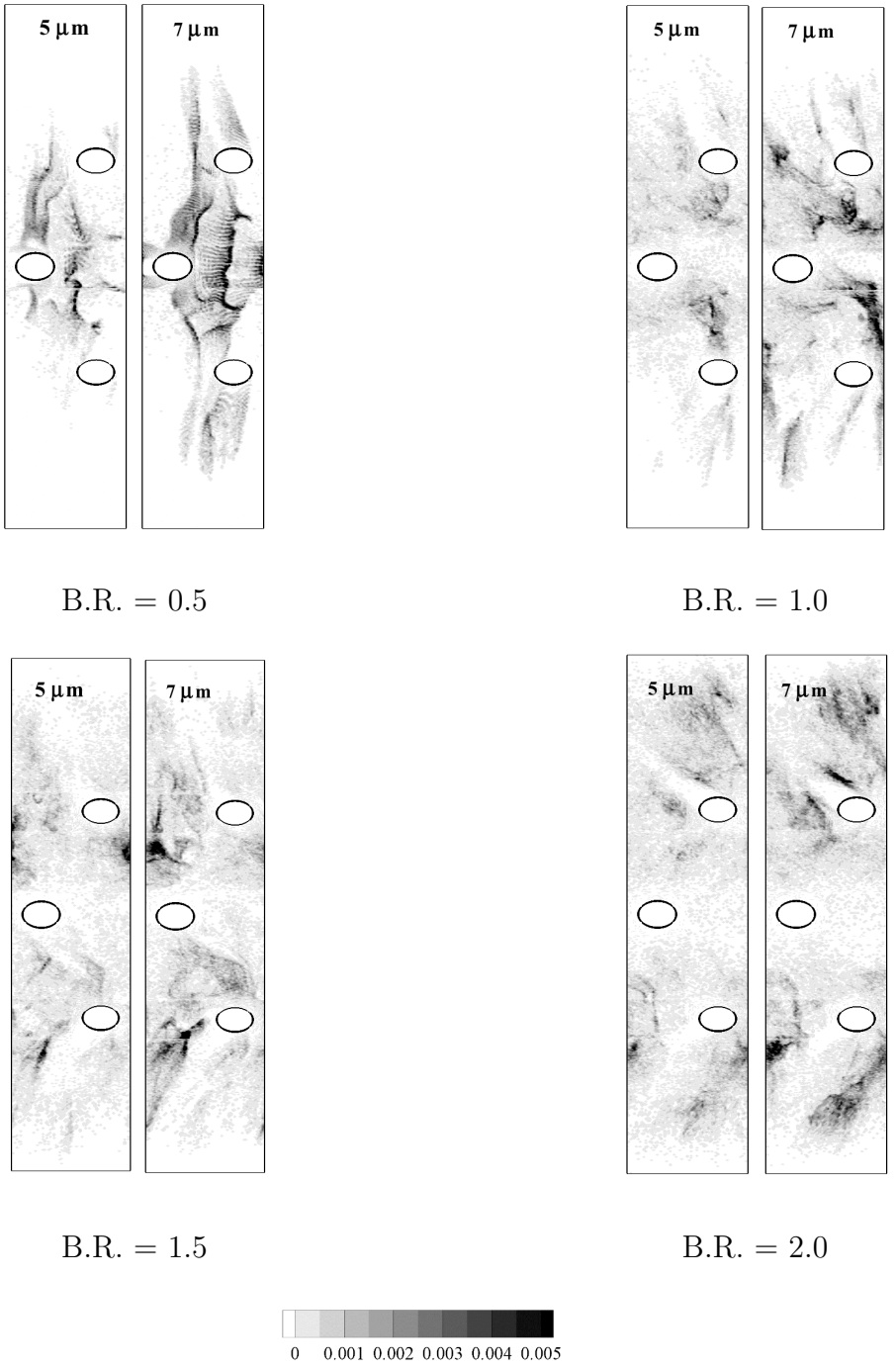

Figure D.6.: Percentage of particles leading to potential erosion on leading edge vane surface (direction of coolant is from right to left)

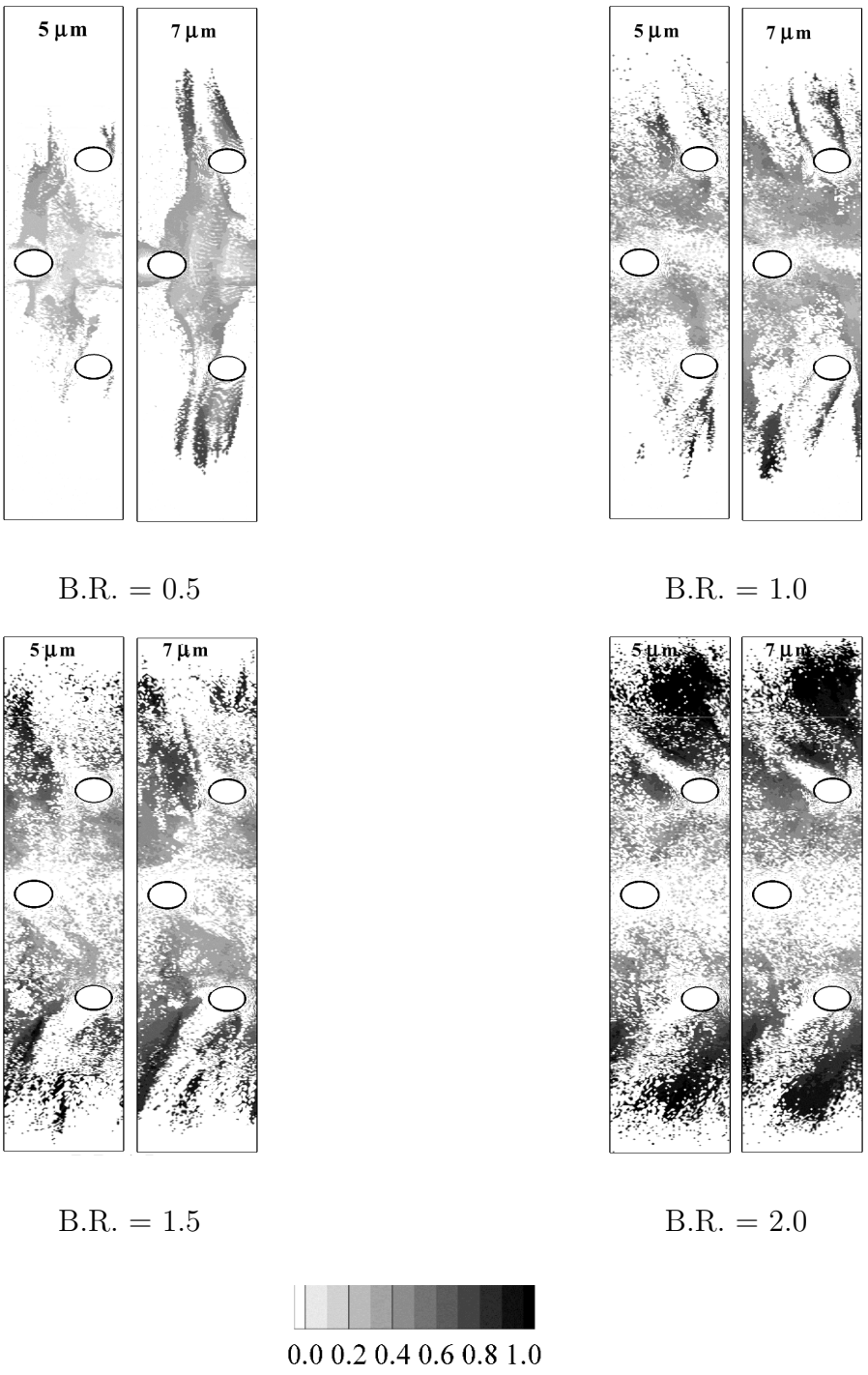

Figure D.7.: Impact velocities of particles leading to potential erosion on leading edge vane surface (direction of coolant is from right to left)

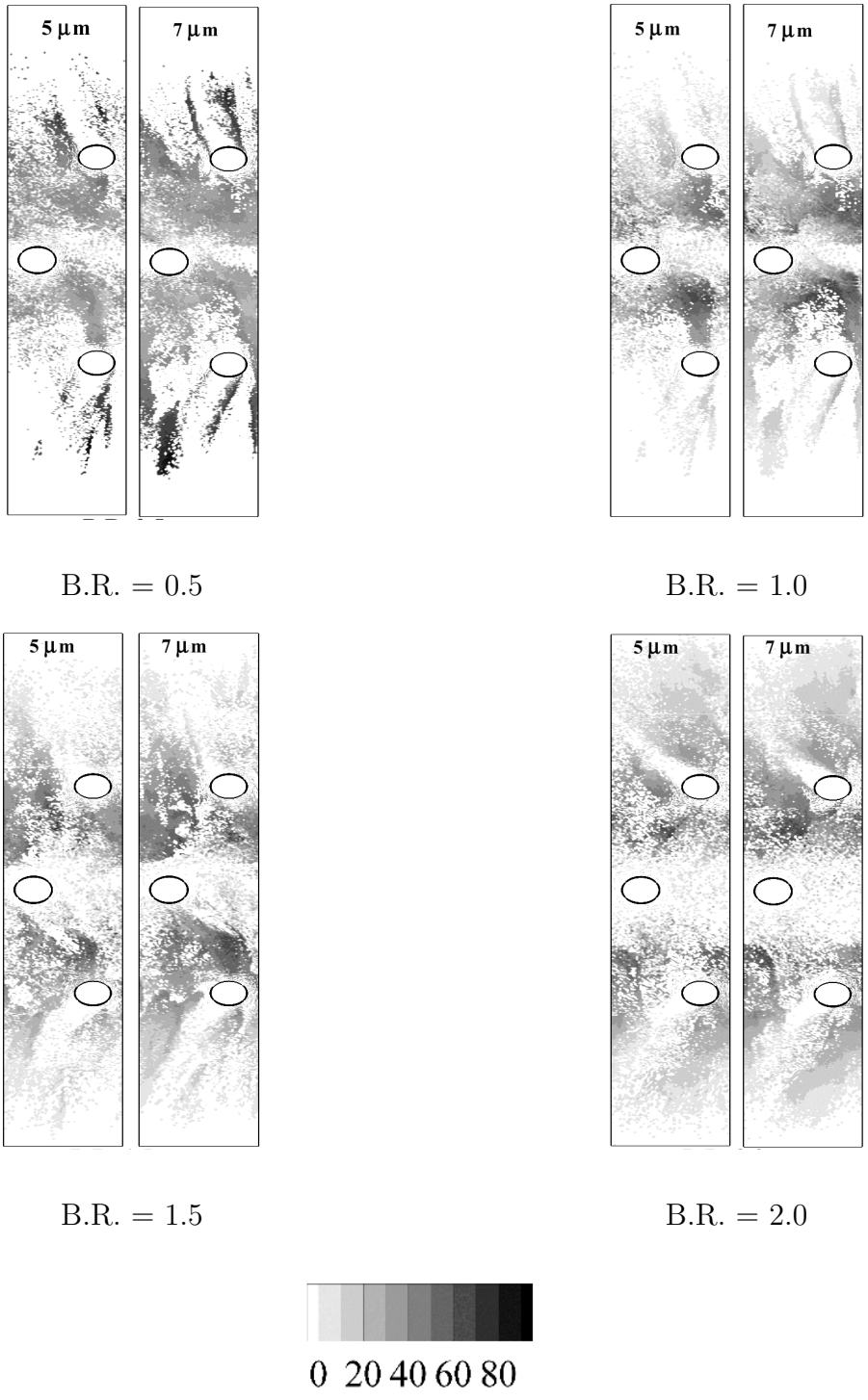

Figure D.8.: Impact angles of particles leading to potential erosion on leading edge vane surface (direction of coolant is from right to left)

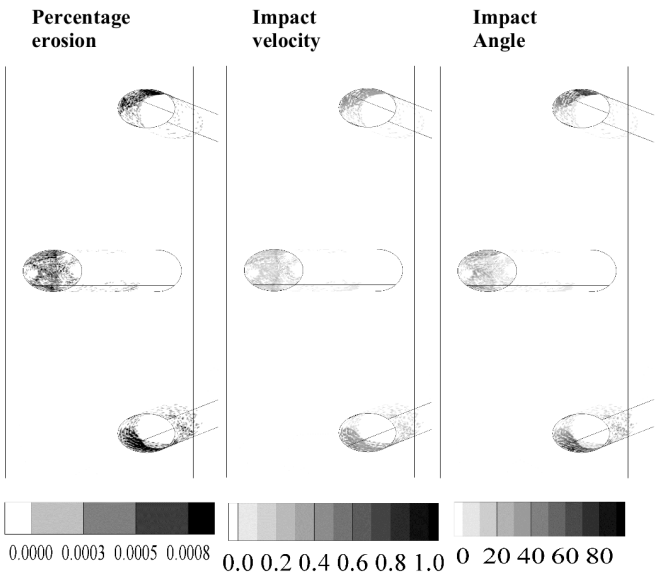

Figure D.9.: Scope of potential erosion in coolant pipe for 7 μm particles for a coolant to mainstream blowing ratio of 0.5 (direction of coolant is from right to left)

Table D.3: Percentage energy fraction of erosive particles (EFEP)

B.R.	Particle Size, μm	5	7
0.5	Coolant Hole	0.02	0.12
	Vane Surface	0.14	0.65
	Total EFEP	0.16	0.77
1.0	Coolant Hole	0.04	0.11
	Vane Surface	0.31	0.67
	Total EFEP	0.35	0.78
1.5	Coolant Hole	0.01	0.01
	Vane Surface	0.68	1. 06
	Total EFEP	0.69	1.07
2.0	Coolant Hole	0.01	0.02
	Vane Surface	0.97	1.52
	Total EFEP	0.98	1.54

As the blowing ratio increases further to B.R.=1, 1.5, and 2.0, the increase in coolant jet momentum at stagnation succeeds in pushing particles away from the stagnation region and the number of erosive particles reaching the surface decrease. Downstream of stagnation, the pattern looks quite similar in its gross features to the deposition pattern (Chapter 3; figure 3.6). Between the stagnation and off-stagnation row, the concentration of erosive particles coincides with areas of large deposition with relatively large velocities and large impact angles. Since these regions are not well protected by the coolant flow (Figure D.4), it is reasoned that the erosive particles get to these locations on the surface through the same mechanism as do the particles which are deposited - i.e., through entrainment in the fountain flow setup by the stagnation coolant jet.

Erosive particles at the off-stagnation coolant jets are concentrated around the periphery of the coolant path on the aft and fore side. More 7 μm particles reach the surface as erosive particles in this region. The concentration of erosive particles increases on the aft side of the coolant path at B.R.=2 with high impact velocities but low angles of impaction. These particles are entrained by the coolant jet, which cools them below the softening temperature and as the coolant is pushed back to the surface, it transports the particles which impinge on the surface. There is a clear correlation between the region of high adiabatic effectiveness in figure D.4 at B.R.=2, downstream of the off-stagnation coolant jets and the high concentration of erosive ash particles which impinge at a high velocity and relative large angles.

Unlike deposition, a very tiny fraction of particles contribute to erosive wear in the coolant channels as shown in figure 13 for 7 μm particles at B.R.=0.5. Figure D.9 also shows the average impact velocity and the respective impact angle. Increasing the blowing ratio substantially decreases the amount of particles (upto 80%, Table D.3) that enter the coolant pipe.

The percentage of erosive particles that impact the surface is summarized in figure D.10 which shows the erosive efficiency (includes the vane surface and coolant pipe) as a function of blowing ratio. Erosive efficiency is defined as the percentage of

particles that impact and elastically rebound to the total number of particles injected which spans the projected vane area at the inlet. In the present case, the plane of particle injection covers 70% of the projected vane area and the remaining 30% is assumed to disperse and flow with the streamlines without impacting the vane surface. Erosive ash particles of 5 μm size increase with increase in blowing ratio. Whereas the percentage of particles potentially eroding the vane surface for 7 μm particle sizes are almost constant at 10% except a dip at blowing ratio of 1.5. The larger trend in the behavior of erosive particles with blowing ratio is similar to that observed for deposition. The difference between the two particle sizes is largest at the low blowing ratio which decreases as the blowing ratio increases.

The general increase in both deposition and erosive particles with blowing ratio figure D.11 for the 5 μm particles agrees with the observation that at the low momentum Stokes number of 0.25, more particles are entrained in the vicinity of the surface by the coolant jets as the blowing ratio increases. Whereas, more of the 7 μm particles penetrate into the inner layer by virtue of their larger inertia at low blowing ratios, as the blowing ratio increases the coolant jets are more successful in pushing the particles away from the surface resulting in less number of particles reaching the surface. However, this trend is reversed again as the blowing ratio increases to 2.

Finally, an estimate is made of the fraction of incoming particle energy that can potentially be transferred to the surface as erosive energy. This is defined by the variable EFEP (Energy Fraction of Erosive Particles). EFEP is calculated as the ratio of kinetic energy of erosive particles to the initial kinetic energy possessed by the particles injected upstream.

$$(EFEP)_p = \frac{\sum\limits_{surface}\sum\limits_{time} 1/2\ m_{erosive} V^2_{normal}}{\sum 1/2\ m_p U^2_\infty} \tag{D.1}$$

The EFEP quantifies the percentage transfer of initial kinetic energy which leads to potential erosion and is tabulated in Table D.3. As one would expect the

values for 7 μm at a blowing ratio of 2.0 signifies highest fraction of energy (1.54%) being imparted to the vane surface. The potential for vane surface erosion increases with blowing ratio for both particle sizes.

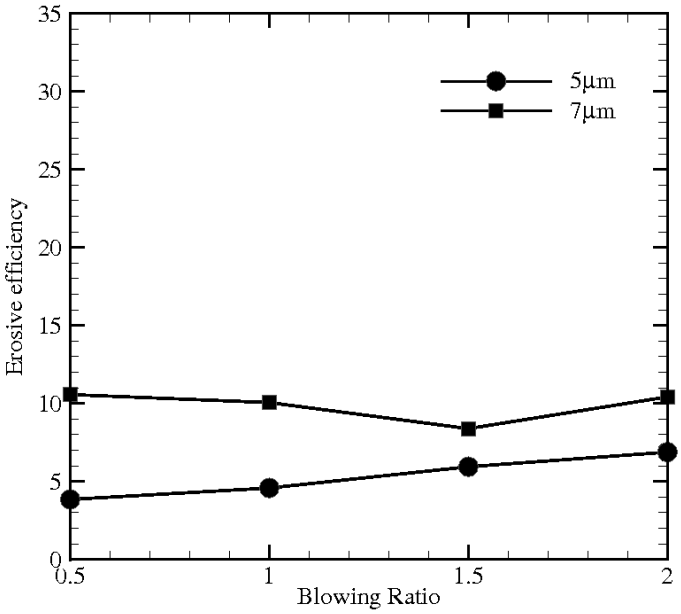

Figure D.10.: Erosive efficiency of particles as a function of blowing ratio

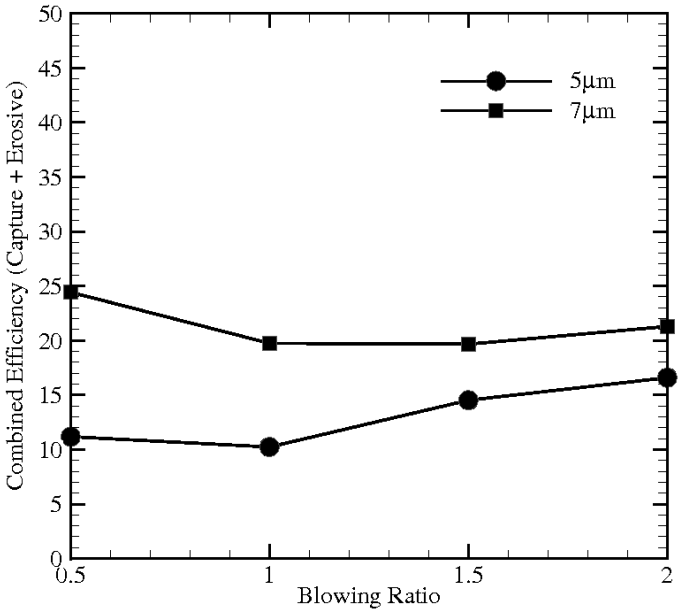

Figure D.11.: Total percentage of particles hitting the wall as a function of B.R.

D.4 Conclusions

Computational studies have been carried out on a three-row leading edge vane geometry to investigate ash deposition and erosion for particle sizes of 5 and 7 μm and jet to mainstream blowing ratios of 0.5, 1.0, 1.5 and 2.0. The simulations use LES for an accurate representation of the highly turbulent flow field with Lagrangian dynamics for the ash particles.

The momentum Stokes number is the single most important parameter which regulates the particle trajectory in the flow field by its response to the flow field surrounding it followed by the jet-mainstream blowing ratio. While the momentum Stokes number is a good indicator of whether an ash particle gets near the vane surface, the thermal Stokes number together with the ash softening temperature in relation to the mainstream, coolant, and surface temperature govern whether an ash particle deposits on the surface.

Under the conditions of the current simulations, both ash particles have Stokes numbers less than unity of O(1) and hence are amenable to be strongly affected by the flow and thermal field generated by the coolant interaction with the mainstream. Because of this, the stagnation coolant jets are quite successful in pushing the particles away from the surface and minimizing deposition and erosion in this region.

The potential for erosive wear increases in regions where the particles have sufficient contact with the coolant to cool down below the softening temperature. At B.R.=0.5, most of the erosive wear occurs in the stagnation region which is a result of particles entrained in the coolant jet. As the blowing ratios increase, the stagnation region is relatively free of erosive wear as the particles are pushed away from the surface. However, similar to the deposition mechanism (§3.4.2), these particles are pushed back to the surface downstream of stagnation, some of which contribute to erosion of the surface. Another region of high potential erosion, as the blowing ratio increases to 2.0, lies downstream of the off-stagnation jets in the region where the coolant jet is pushed back to the surface bringing with it entrained ash particles.

Overall, erosive ash particles of 5 μm size increase from 4% of the total to 7% as the blowing ratio increases from 0.5 to 2.0, whereas the 7 μm erosive particles remain nearly constant at 10% The larger trend in the behavior of erosive particles with blowing ratio is similar to that observed for deposition. The difference between the two particle sizes is largest at the low blowing ratio and decreases as the blowing ratio increases.

Overall, for particles of size 5 μm, there is a combined increase in deposition and erosive particles (see Chapter 3) from 11% to 17% as the blowing ratio increases from 0.5 to 2.0. The 7 μm particles, on the other hand decrease from 24% to about 21% as the blowing ratio increases from 0.5 to 2.0.

D.5 Bibliography

[1] Bunker, R. D., 1985. "Deposition, erosion and corrosion protection for coal-fired gas turbine". *ASME Paper Number 85-IGTI-61.*

[2] Tabakoff, W., 1991. "Measurements of particles rebound characteristics on materials used in gas turbines". *Journal of Propulsion,* ***7***(5), pp. 805–813.

[3] Bons, J. P., Crosby, J., Wammack, J. E., Bentley, B. I., and Fletcher, T., 2005. "High pressure turbine deposition in land based gas turbines from various synfuels". *ASME Paper Number GT-2005-68479.*

[4] Bons, J. P., Taylor, R., McClain, S. T., and Rivir, R. B., 2001. "The many faces of turbine surface roughness". *Journal of Turbumachinery,* ***123***, pp. 739–748.

[5] , 1988. *Particulate Flows and Blade Erosion - lecture series 1988-08.* Von Karman Insititute for Fluid Dynamics, Rhode Saint Genese, Belgium.

[6] Finnie, I., 1960. "Erosion of surfaces by wear". *Wear,* ***3***, pp. 87–103.

[7] Metwally, M., Tabakoff, W., and Hamed, A., 1995. "Blade erosion in automotive gas turbine engine". *Journal of Engineering for Gas Turbine and Power,* ***117***, pp. 213–219.

[8] Tabakoff, W., 2006. "Engine deterioration when exposed to particulate flows". *ASME Paper Number GT2006-91236.*

[9] Siravuri, S., Tabakoff, W., and Gunaraj, J. A., 1999. "Experimental investigation of particle rebound characteristics on turbomachinery leading edge geometry". *ASME Paper Number 99-GT-193.*

[10] Hamed, A., Tabakoff, W., and Wenglarz, R., 2006. "Erosion and deposition in turbomachinery". *Journal of Propulsion and Power,* ***22***(2), pp. 350–360.

[11] Hamed, A., Tabakoff, W., Rivir, R., Das, K., and Arora, P., 2005. "Turbine blade surface deterioration by erosion". *Journal of Turbomachinery,* ***127***, pp. 445–452.

[12] Shah, A., and Tafti, D., 2007. "Transport of particulates in an internal cooling ribbed duct". *Journal of Turbomachinery,* ***129***(4), pp. 816–825.

[13] Rozati, A., Tafti, D., and Sreedharan, S., 2008. "Effect of snygas ash particle size on deposition and erosion of a film cooled leading edge". *ASME Paper Number HT2008-56155.*

[14] Chong, M. S., Perry, A. E., and Cantwell, B. J., 1990. "A general classification of three dimensional flow fields". *Physics of Fluids A,* ***2***(5), pp. 765–777.

[15] Mbabazi, J. G., Sheer, T. J., and Shandu, R., 2004. "A model to predict erosion on mild steel surfaces impacted by boiler fly ash particles". *Wear,* ***257***, pp. 612–624.